BORON NITRIDE/ZINC DOPED HYDROXYAPATITE/POLYCAPROLACTONE COMPOSITE SCAFFOLDS FOR BONE TISSUE ENGINEERING

A THESIS SUBMITTED TO
THE GRADUATE SCHOOL OF NATURAL AND APPLIED SCIENCES
OF
MIDDLE EAST TECHNICAL UNIVERSITY

BY

EMİNE AYŞE TURHAN

IN PARTIAL FULFILLMENT OF THE REQUIREMENTS
FOR
THE DEGREE OF MASTER OF SCIENCE
IN
MICRO AND NANOTECHNOLOGY

MARCH 2021

Approval of the thesis:

BORON NITRIDE/ZINC DOPED HYDROXYAPATITE/POLYCAPROLACTONE COMPOSITE SCAFFOLDS FOR BONE TISSUE ENGINEERING

submitted by **EMİNE AYŞE TURHAN** in partial fulfillment of the requirements for the degree of **Master of Science** in **Micro and Nanotechnology, Middle East Technical University** by,

Prof. Dr. Halil Kalıpçılar
Dean, Graduate School of **Natural and Applied Sciences** _____

Prof. Dr. Almıla Güvenç Yazıcıoğlu
Head of Department, **Micro and Nanotechnology** _____

Prof. Dr. Zafer Evis
Supervisor, **Engineering Sciences Dept., METU** _____

Prof. Dr. Ayşen Tezcaner
Co-Supervisor, **Engineering Sciences Dept., METU** _____

Examining Committee Members:

Prof. Dr. Dilek Keskin
Engineering Sciences Dept., METU _____

Prof. Dr. Zafer Evis
Engineering Sciences Dept., METU _____

Prof. Dr. Ayşen Tezcaner
Engineering Sciences Dept., METU _____

Asst. Prof. Dr. Bengi Yılmaz
Biomaterials Dept., University of Health Sciences _____

Asst. Prof. Dr. Ammar Z. Alshemary
Biomedical Eng. Dept., Karabük University _____

Date: 16.03.2021

I hereby declare that all information in this document has been obtained and presented in accordance with academic rules and ethical conduct. I also declare that, as required by these rules and conduct, I have fully cited and referenced all material and results that are not original to this work.

Name Last name : Emine Ayşe Turhan

Signature :

ABSTRACT

BORON NITRIDE/ZINC DOPED HYDROXYAPATITE/POLYCAPROLACTONE COMPOSITE SCAFFOLDS FOR BONE TISSUE ENGINEERING

Turhan, Emine Ayşe

Master of Science, Micro and Nanotechnology

Supervisor: Prof. Dr. Zafer Evis

Co-Supervisor: Prof. Dr. Ayşen Tezcaner

March 2021, 112 pages

Bone diseases and disorders have been expected to increase mostly in time because of the aging, obesity and pysical activity problems. For this reason, bone tissue engineering has been focus point to design new biocompatible scaffolds and enhance bone tissue regeneration. Composite scaffolds composed of PCL, Zn doped hydoxyapatite (HA), and boron nitride nanofibers (BNNFs) were prepared by the rotary jet spinning for bone tissue engineering applications. Synthesis of BNNFs and Zn-HA was achieved by the freeze drying and the wet chemical methods, respectively and then verified by XRD, FTIR, SEM and ICP analyses. The composite scaffolds were characterized for morphological properties, bioactivity, biocompatibility and mechanical properties. The bioactivity of PCL, PCL-Zn HA, PCL-Zn HA-BNNF and PCL-BNNF scaffolds was tested in simulated body fluids (SBF) and PCL-Zn HA-BNNF group showed good bioactivity by forming higher amount of apatite layer. Furthermore, proliferation and osteogenic activity of cells in all groups were investigated by Saos-2 cells. The results showed that the highest proliferation and osteogenic activity of cells

were obtained in PCL-Zn HA-BNNF group. Furthermore, compression test results revealed that compressive properties of PCL scaffolds were improved by the addition of both BNNF and Zn HA but tensile tests showed that addition of Zn HA or BNNF reduced the strength of PCL due to the agglomeration of particles. Our results showed that PCL-Zn HA-BNNF scaffolds holds promise for bone tissue engineering applications

Keywords: Hydroxyapatite, Boron Nitride Nanofiber, PCL, Bone Tissue Engineering, Rotary Jet Spinning

ÖZ

KEMİK DOKU MÜHENDİSLİĞİ İÇİN BOR NİTRÜR/ÇİNKO KATKILI HİDROKSİAPATİT/POLİKAPROLAKTON KOMPOZİT İSKELELER

Turhan, Emine Ayşe
Yüksek Lisans, Mikro ve Nanoteknoloji
Tez Yöneticisi: Prof. Dr. Zafer Evis
Ortak Tez Yöneticisi: Prof. Dr. Ayşen Tezcaner

Mart 2021, 112 sayfa

Yaşlanma, obezite ve fiziksel aktivite sorunları nedeniyle kemik hastalıkları ve bozukluklarının zamanla artması beklenmektedir. Bu nedenle, kemik dokusu mühendisliği, yeni biyouyumlu iskeleler tasarlamak ve kemik dokusu rejenerasyonunu geliştirmek için odak noktası olmuştur. PCL, çinko katkılı hidroksiapatit (HA) ve bor nitrür nanofiberlerden (BNNF'ler) oluşan kompozit iskeleler, kemik dokusu mühendisliği uygulamaları için rotary jet eğirme ile hazırlandı. BNNF'ler ve ağırlıkça% 1 Zn-HA içeren biyoseramiklerin sentezi, sırasıyla dondurarak kurutma ve yaş kimyasal yöntemle sağlandı ve ardından XRD, FTIR, XPS, SEM ve ICP analizleri ile doğrulandı. Kompozit yapı iskeleleri, morfolojik özellikler, biyoaktivite, biyouyumluluk ve mekanik özellikler açısından karakterize edildi. PCL, PCL-Zn HA, PCL-Zn HA-BNNF ve PCL-BNNF iskelelerinin biyoaktivitesi uyarılmış vücut sıvılarında (SBF) test edilmiş ve PCL-Zn HA-BNNF grubu daha yüksek miktarda apatit tabakası oluşturarak iyi biyoaktivite göstermiştir. Ayrıca tüm gruplardaki hücrelerin proliferasyonu ve osteojenik aktivitesi Saos-2 hücreleri tarafından araştırıldı. Sonuçlar, hücrelerin en yüksek proliferasyon ve osteojenik aktivitesinin PCL-Zn HA-BNNF grubunda elde

edildiğini gösterdi. Ayrıca, sıkıştırma testi sonuçları, PCL iskeletlerinin sıkıştırma özelliklerinin hem BNNF hem de Zn HA ilavesiyle iyileştirildiğini ancak gerilme testleri Zn HA veya BNNF ilavesinin partiküllerin aglomerasyonu nedeniyle PCL'nin gücünü azalttığını gösterdi. Sonuçlarımız, PCL-Zn HA-BNNF iskelelerinin kemik dokusu mühendisliği uygulamaları için umut vaat ettiğini gösterdi.

Anahtar Kelimeler: Hidroksiapatit, Bor Nitrür Nanofiber, PCL, Kemik Doku Mühendisliği, Merkezkaç kuvvetiyle eğirme

To my dear family

ACKNOWLEDGMENTS

I am grateful and deepest appreciation to my thesis advisor Prof. Zafer Evis for his support, encouragement, knowledge, endless patience and guidance throughout in this thesis with his knowledge and experience. His valuable insights and directions gave me guidance to complete this research.

I owe my appreciation and gratitude to my co-advisor Prof. Dr. Ayşen Tezcaner, for her perspective, experience in cell culture studies, guidance, precious ideas, advices and comments enlightened me on this research and bone tissue engineering.

I am also grateful to Prof. Dr. Dilek Keskin for her valuable advices and guidance throughout my cell culture studies.

I am also grateful to my research mentor Sema Akbaba for her great contributions, guidance and precious friendship through all experiments and discussion of results.

I would also like to thank to my friends and labmates Buşra Yedekçi, Ali Motameni, Hossein Jodati and Ahmet Engin Pazarçeviren for their valuable contribution and support in my thesis. I am also grateful to Sevim Bulgurcu, Gizem Demir, İdil Uysal, Merve Canyurt, Sinem Yetim, Zehra Canyurt, Merve Derya Oflaz, Saliha Gün, Serra Tütüncü and Esma Turhan for their never ending love and motivation.

I would like to give my foremost thanks to my father Süleyman Turhan and my mother Zühre Turhan for their effort and endless love.

I am also grateful to National Boron Research Institute for allowing me to work in their laboratories and use their lab equipments.

TABLE OF CONTENTS

LIST OF TABLES

TABLES

LIST OF FIGURES

FIGURES

LIST OF ABBREVIATIONS

ABBREVIATIONS

Zn HA	Zinc Hydroxyapatite
HA	Hydroxyapatite
ALP	Alkaline Phosphatase
BSA	Bovine Serum Albumin
BCA	Bicinchoninic Acid
BNNF	Boron Nitride Nanofiber
BNNT	Boron Nitride Nanotube
BTE	Bone Tissue Engineering
CaP	Calcium Phosphate
c-BN	Cubic Boron Nitride
DMEM	Dulbecco's Modified Eagle Medium
ECM	Extracellular Matrix
EDX	Energy Dispersive X-Ray Spectroscopy
FTIR	Fourier Transform Infrared
FBS	Fetal Bovine Serum
h-BN	Hexagonal Boron Nitride
JCPDS	Joint Committee on Powder Diffraction
PBS	Phosphatase Buffered Solution

PCL	Poly ε-caprolactone
PLGA	Poly(lactic-co-glycolic acid)
PLLA	Poly-L-Lactic acid
pNPP	P-Nitrophenol
PS	Polystyrene
SBF	Simulated Body Fluid
SEM	Scanning Electron Microscope
TCPS	Tissue Culture Polystyrene
TCP	Tricalcium Phosphate
TE	Tissue Engineering
$^{W}/_{V}$	Weight per volume
$^{W}/_{W}$	Weight per weight
XRD	X-Ray Diffraction
XPS	X-ray photoelectron spectroscopy

CHAPTER 1

INTRODUCTION

1.1 Tissue Engineering

Tissue engineering (TE) which is an interdisciplinary research field uses scientific principles of life sciences and engineering and it aims to stimulate new tissue formation as an alternative to organ transplantation. There is only small percentage of available organ donors for transplantation. Morever, list of people who seek the medical treatment is very crowded and as a result of this, they can die without getting any transplantation or treatment. This affects the patient quality of life badly. Thus, TE has a huge impact on the human health through studies focused on elucidating the mechanism of diseases and developing new artificial devices for injured organs or tissues. In the past, organ transplantation was limited because of the immunological rejection from the body and organ deficiency. Besides, there is only transplantation of specific organs instead of all of them such as kidney and liver. Additionally, money has an influence for the organ transplantation. As a result of this, new strategies have been developed to supply enough organs equally for all people who are waiting for organ transplantation due to technological improvement. To address these problems and seek new solutions to improve the life of patients, TE has a potential to regenerate and replace the injured organs by designing new biomaterials. Biomaterials field is an interdisiplinary research area by bringing different fields together to design and fabricate materials. It has a huge impact on human health by substituting damaged tissues or organs with biomaterials or stimulating generation of new tissues without causing any toxic effect.

1.1.1 Bone Tissue Engineering

The aim of bone tissue engineering research is to fabricate materials which outperform bone reformation. This material is found in the form of scaffold which

provides support for cell attachment, differentiation mineral deposition and then regeneration and remodeling by patient's cells when it is placed into bone defect. The formation of new bone is highly dependent on the defect site, structure and function of scaffolds. Thus, scaffold fabrication has to be fabricated for target bone tissue. As an example; orthopaedic defects are generated in the long bones of the limbs or spinal vertebrae which undergo torsional and compressive loads during the walking. Besides, craniofacial bone defects are resulted from injuries, infections, diseases and congenital problems rather than problems of load bearing (Koons et al., 2020). Thus, structure of bone is very important for production of scaffolds.

1.1.1.1 Bone

Bone provides highly vascularized connective tissues, protective for organs and support for cell attachment. Bone includes organic and inorganic structures. In the mineralized matrix of bone, organic phase exists with mainly collagen to provide rigidity, toughness and viscoelasticity. The mineral phase of carbonated apatite as an inorganic phase enables structural stiffness, reinforcement and mineral homeostasis. The other non-collagenous proteins create a microenvironment for stimulation of cellular functions. Besides, bone has layered structure with a macrostructure (cortical bones and cancellous bone), microstructure (Haversian system, osteon, single trabeculae) and and subnanostructure (minerals, collagen and non-collagenous organic proteins (Henkel et al., 2013). The compact bone has a complex sytem than cancellous bone. In the macrostructure of bones, compact bone includes closely packed haversian and osteon systems. The osteons have central canals named as osteonic (haversian) canals surrounding with concentric rings (lamellae) of matrix. The bone cells of osteocytes are placed between the rings of matrix which is named lacunae. Small channels exist between lacunae and osteonic (haversian) canals for passage through the hard matrix. In the compact bone, haversian canals are tightly packed and form a solid mass. Additionally, osteonic canals include blood vessels which are interconnected and parallel to the axis of the bone. The structural organization of bone is represented in Figure 1.1.

The density of cancellous (spongy) bone is less and lighter than compact bone. It includes trabeculae and bars of bone which are close to cavities including the red bone marrow. The canaliculi are occupied to adjacent cavities to take blood supply.

The process of bone formation is named as ossification or osteogenesis. This process starts with osteoblast cells by secreting unmineralized collagen (osteoid) and alkaline phosphatase which increase the accumulation of calcium and phosphate bone mineral and fibres of collagen. Then, osteoblasts are surrounded with mineralized bone matrix so they become mature to osteocytes. Additionally, active osteoblasts are determined by bone lining cells that provide cell proliferation and differentiation. Osteocytes have vital role for regulation of bone formation and resorption according to mechanical stress in the local environment. Additionally, they are responsible for fracture bone healing. Bone resorption is achieved by osteoclasts which have multinucleated cells and they can differentiate into macrophages. They perform bone dissolution and absorbtion by secreting acid phosphatase which dissolves both inorganic materials consisting of calcium and phosphorus and organic collogen in the bone. (Koons et al., 2020).

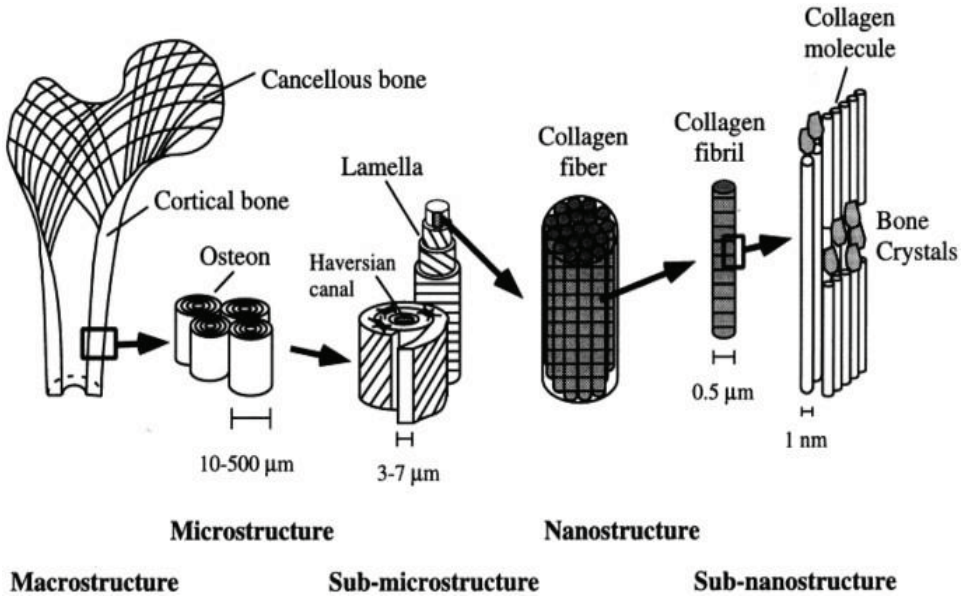

Figure 1.1 Systematic representation of structural organization of bone (Henkel et al., 2013).

1.1.2 Biomaterials

The definition of biomaterial was named as a nonviable material and used in a medical device by interacting biological systems. In time, this definition has been redefined many times and reached a concensus as biomaterial evolves for medical applications. This definition is: “A biomaterial is a substance that has been engineered to take a form which, alone or as part of a complex system, is used to direct the course of any therapeutic or diagnostic procedure by controlling the interactions with components of living systems, in human or veterinary medicine”. In this respect, biomaterial has to be nontoxic, biocompatible and load bearing.

In the very early times, dental implants were found as stone and ivory in China and Egypt. In 16^{th} and 17^{th} centuries, gold and ivory dental implants were reported (More et al., 2013). Besides, other metal implants consisting of gold, lead, iridium, tantalum, stainless steel and cobalt alloys were also reported in the early 20^{th} century (Singh et al., 2019). To improve their biocompatibility and mechanical properties, different polymers such as polyurethane, polyamide, polymethylmethacrylate resin, polytetrafluoroethylene and polyurethane were started to find use in many different parts of the body. These polymers do not only improve biocompatibility but also enhance mechanical properties (Singh et. al, 2019). Biocompatibility, an important term in the biomaterial field, is defined as the ability of material to have an appropriate host response in a specific application. The appropriate host response was explained as not causing any side effect or complications during the healing process such as thrombogenesis, mutagenesis and carcinogenesis (More et al., 2013). As an example, hemodialysis membranes are used to eliminate uremic toxins, excess ions and water by the process of dialysate. During this process, membrane includes diffusion of solutes in blood over a semipermeable membrane and flow of the dialysate is opposite to the flow direction of blood in the extracorporeal circuit. In the counter-current flow, concentration of gradient across membrane retains at maxiumum level so efficiency of dialysis increases. In conventional hemodialysis, process is done for three times in one week and each treatment requires three to four hours to draw blood of each patient with a rate of 200-400 ml/min. In this way, biocompatibility

is a very important factor for purification of the blood without causing any complications. In another example, in the case of hip-joint prosthesis, it is implanted into human body and stay for lifetime of patients. In that case, appropriate host response is very important for patients to maintain the function of tissue and generation of tissue without causing any complications or toxic effects. In this respect, there are many synthetic biomaterials used in the body such as ceramics, polymers, glasses, carbons and composite materials. These materials can be found in the form of fibers, films, foams, molded or machined parts and fabrics. These materials are classified according to their interaction with tissue or body fluids because when these biomaterials are implanted in the organism, their interaction and degradation behavior differ in terms of ways and time. In this respect, they are categorized as bioinertness, bioactivity and bioresorbability.

Bioinert materials like tantalum, titanium, stainless steel, aluminum and zirconium oxides when implanted in human body result in minimum interaction with surrounding tissue or organs. They don't initiate a response or interaction with tissues or organs. This makes them highly stable. However, these bioinert materials can damage surrounding tissues or organs when they start to degrade because of some toxic ions (Dubok, 2000).

Bioactive materials (hydroxyapatite (HA), tricalcium phosphate (TCP) and bioglasses etc.) have a contact with bone tissue or organs and resulted in chemical reaction or ion exchange reaction with surrounding tissue and body fluids when they are implanted in living organism. They enable the formation of the apatite active layer which has similar structure with natural bone on the bioceramic implants. Bioresorbable materials (i.e., TCP, porous HA, calcium phosphate (CaP) salts, certain bioglasses, polyurethane and polylactic–polyglycolic acid copolymers) dissolve gradually without causing any toxic effect and regenerate new tissues after implanting in the living organism. Morever, there are common types of biomaterials which are engineered for use in a specific area. As an example, for hip-joint implants, metals and alloys are chosen because of their better osteoconductive and load bearing properties.

Polymeric scaffolds are preferred for soft tissues because they have porous structure which enables good osteconductivity, biodegradation, permeability,

mechanical strength and transparency. Among these properties, biodegradation is the most important one because these polymers can be removed from human body by breaking down or resorbing instead of surgery. Polymers are classified as natural and synthetic. Natural polymers are classified as proteins and polysaccharides. Proteins are collagen, gelatin, elastin, silk, albumin, fibrin and keratin while polysaccharides are chitosan, alginic acid, hyaluronic acid, cellulose and chondroitin sulfate (Tang et al., 2014). These polymers are commonly used in TE applications.

1.1.2.1 Natural Biomaterials

Natural biomaterials are highly applicable due to their biocompatibility and good bioactivity properties which enhance cell attachment and proliferation. They are classified in two types including bioactive proteins (collagen, gelatin, elastin, silk, albumin, fibrin and keratin) and polysaccharides (chitosan, alginic acid and hyaluronic acid) (Dwivedi et al., 2020).

1.1.2.1.1 Collagen

Collagen is a good candidate for engineering hard tissues because it is found in extracellular matrix (ECM) of musculoskeletal tissues along with other tissue types. In human body, there are 22 different types of collagen present. Collagen types of I-IV are found most abundantly. Collagen is obtained from mammals to use it in the scaffold. Morever, collagen is very easy to process. In that way, different collagen based scaffolds can be obtained in desired shapes such as tubes (Huang et al., 2011), sheet (Yamauchi et al., 2004), sponges (Shen et al., 2010) and powders (Tomoaia et al., 2013) to use them in the applications of muscle (Drury & Mooney, 2003), skin (Liu et al., 2012), cardiovascular (Sell et al., 2009), tendon (Kew et al., 2011), cartilage (Olivier et al., 2004) and ligament (Laurencin & Freeman, 2005). This makes collagen ideal for TE. Nanofibrous collagen scaffolds were used to fabricate a biomimetic nanofibrous extracellular matrix for tissue engineering. This scaffold is very efficient for wound healing. Type I collagen nanofibrous extracellular matrices which were electrospun using

1,1,1,3,3,3-hexafluoro-2-propanol (HFIP) were prepared as biodegradable and biomimetric scaffolds to investigate their potential in promoting adhesion and spreading of human keratinocytes. Cellular response was also studied after adsorbing type I collagen, fibronectin and laminin onto the ECM matrices. surface modified matrices were used for wound healing in twelve Sprague–Dawley rats. In both groups including Type I collagen and laminin coated ECM matrices, epithelization of the wound was completed at the end of 4 weeks and connective tissue was generated densely without any inflammation based on the histological examination. It was asserted that type I collagen and laminin coated matrices were significantly higher than control groups (uncoated collagen nanofibers) in terms of adhesion of NHEK and NHOK and their high surface area (Rho et al., 2006). In another study, rat Blood Outgrowth Endothelial cells (rBOEC) and genetically modified rBOEC (rBOEC/eNOS-GFP) were seeded on the nanofibrous scaffolds of PLA-chitosan (PC) and PLA-chitosan-collagen (PCC) to investigate attachment and viability of cells on these scaffolds. Viability and attachment of both rBOEC and rBOEC/eNOS-GFP on PCC scaffolds were significantly higher than those of PC nanofibrous scaffolds because of the presence of collagen that makes it as a potential candidate for vascular tissue and wound healing applications (Swarnalatha et al., 2013). Ngiam et al. (2009) investigated the deposition of nano-hydroxyapatite (nHA) by CaP dipping method on PLGA and PLGA/collagen (PLGA/Col) nanofibers which was fabricated through electrospinning. The quantity of deposited nHA was significantly higher on the PLGA/collagen nanofiber composites and presence of nHA enhanced the attachment and proliferation of the osteoblast cells.

1.1.2.1.2 Gelatin

Gelatin is one of the widely used biopolymers in many different applications such as food packaging, pharmaceutical, medical, cosmetic, and TE. It can be found in skin, bone and cartilage resulted in less immunological response. Thus, cell attachment, differentiation and proliferation will be enhanced (Tang et al., 2014). Gelatin can be obtained through denaturation and hydrolysis of collagen partially (Tang et al., 2014). Gelatin has greater absorbtion of liquid (such as 45 times of its

weight) because of its high porous structure. Additionally, it was absorbed by the body in 4-6 weeks (Chong et al., 2007). In a study, porogen was formed in the gelatin by using water. In this research, gelatin was crosslinked with glutaraldehyde after several washing. Then, this freezed hydrogel was resulted in ice in the hydrogel network. Ice was then sublimated by freeze drying. At the end of this process, interconnected porous structures were obtained uniformly (Kang et al., 1999). There are also other studies about using gelatin with chitosan and HA. This composite formed a 3D porous scaffold and tested on rat calvaria osteoblasts. The results are highly promising to be used in bone TE (Zhao et al., 2002). Gelatin can be combined with other synthetic or natural polymers with a greater interconnected porous structure.

1.1.2.1.3 Chitosan

Chitosan which is a linear polysaccharide containing β-(1-4)-linked d-glucosamine and N-acetyl-d-glucosamine obtained mostly from the hard exoskeletons of shellfish-like shrimp and crab (Tang et al., 2014). The properties of good mechanical, reactive functional groups, biocompatibility and easy synthetic pathway make chitosan very suitable for TE (Kumbar et al., 2002; Madihally & Matthew, 1999; Suh & Matthew, 2000; Tang et al., 2014). They can be fabricated with a different morphology for different tissues. As an example, crosslinked chitosan microspheres were made for drug encapsulation (Kumbar et al., 2002). Besides, biocompatibility and antimicrobial activity of chitosan are great advantages for wound dressing that provides acceleration of the blood clothing, platelet adhesion, thrombin formation and absorbtion of blood (Ong et al., 2008). Chitosans are found in different morphologies such as sponges for cartilage tissue application (Oliveira et al., 2009), hydrogels for nerve generation (Pfister et al., 2006), fibers for wound dressing and drug delivery (Jayakumar et al., 2010) and membranes for skin TE (Chen et al., 2009).

1.1.2.1.4 Alginate

Alginate is a polysaccharide commonly found in the cell wall of brown algae. It possesses hydrophilic properties. Hydration of alginic acid leads to formation of

viscous gum. This provides easy fabrication and shapable process due to hydrophilic properties. Due to existence of carboxylate groups in the structure, gel formation is very easy by making divalent cations and this increases the interaction with other cells and molecules. It is highly recommended in biomedical and TE applications due to its biocompatibility, degradability and less immunological rejections. It is commonly used in drug delivery applications because alginate can be able to encapsulate molecules or different cell types in the process of gelation which resembles the extracellular matrix of tissues. Other usage areas of alginates are regeneration of bone (Venkatesan et al., 2014), delivery of adipose-derived stem cells (Moyer et al., 2010) and chondrocyte encapsulation to treat cartilage repears (Marsich et al., 2007).

1.1.2.2 Synthetic Biomaterials

Synthetic biomaterials have been applied in TE applications for many years due to their better uniform, controllable chemical and mechanical properties. They can be synthesized in different properties just by changing reaction conditions such as monomers, initiators or additives which determine the crystallinity, molecular weight, melting temperature and reactive groups.

1.1.2.2.1 Poly(Lactide-co-Glycolide)

Poly (Lactide-co-Glycolide) is obtained through the copolymerization of 90% glycolic acid (GA) and 10% l-lactic acid (LA). This ratio can be changed to obtain different range diameter for intented applications. Fibrous poly(lactic acid-co-glycolic acid) scaffolds with a diameter of 350-1100 nm were fabricated by electrospinning for skin regeneration (Kumbar et al., 2008). In another study, PLGA was used with HA for potential alendronate (AL) delivery and injectible cell carrier in the bone-repairing therapeutics. Cell culture studies were conducted with macrophages and osteoblasts. The improvement of osteoblastic proliferation and maturation through the released AL in the scaffolds of PLGA/HA-AL microspheres was verified by MTT assay. The results asserted that release of AL prohibited the growth of macrophages while enhanced osteoblast proliferation and upregulating the osteogenic enzyme ALP (Shi et al., 2009). The proliferation and

maturation of osteoblastic by AL release in PLGA/HA-AL microspheres were respectively analyzed by MTT assay and phenotype checking. The same groups of samples and controls in macrophage experiments were achieved for this purpose (Shi et al., 2009).

1.1.2.2.2 Polycaprolactone (PCL)

PCL is semicrystalline and biodegradable polyester that is obtained by ring opening polymerization. The melting temperature and glass transition temperature of PCL are 59-64°C and 60°C, respectively. This polymer is widely preferred for biomedical applications (TEs, drug delivery and regenerative medicine) because of its unique properties of slow degradation rate, biocompatibility and good permeability (Yoshimoto et al., 2003). PCL scaffolds can be produced in different forms. Porous PCL scaffolds can be produced by porogen leaching, saturation or CO_2 releasing, freeze drying and 3D printing. To produce fibrous PCL scaffolds, electrospinning or melt-electrospinning can be used (Dwivedi et al., 2020). Electrospinning is widely used to produce nano-fibers and scaffolds with 3D structures. In this method, PCL can be mixed with other polymers including fibroin, gelatin, PLA, PLGA, polyurethane and aluminum oxide. In another study, PCL was mixed with HA to fabricate 3D electrospun nanofibrous scaffolds through electrospinning. This scaffold mimicked extracellular matrix (ECM) of bone tissue. PCL/HA-3D scaffolds containing bone morphogenic protein-2 (BMP2) signaling activator phenamil significantly increased osteogenic differentiation of C2C12 cells compared to PCL-3D scaffolds (Miszuk et al., 2018). This study showed that PCL/HA scaffold with phenamil enabled appropriate extracellular matrix deposition by increasing osteogenic differention of C2C12 cells. Ectopic bone regeneration was also shown in mouse. In another study, porous PCL scaffolds were fabricated by combination of solvent casting and particulate leaching methods. They evaluated bone cell proliferation and differentiation by *in vitro* studies using mouse calvaria-derived preosteoblastic cells (MC3T3-E1). Porogens were used using water soluble polyethylene glycol (PEG) and sodium chloride (Thadavirul et al., 2014). It was demostrated that scaffold with highly interconnected pore structure increased migration of MC3T3-

E1 cells *in vitro* and vascularization of tissue and 3D mechanically stable structure were observed *in vivo* (Thadavirul et al., 2014). Another group reported that porous PCL/poly-L-lactide (PLLA) composite scaffolds improved proliferation of marrow stromal cells and trabecular osteoblast cells (Guarino et al., 2008). In another study, the nanofiber composite of PCL with nano-HA was fabricated and tested *in vitro* with bone marrow mesenchymal stem cells (MSCs). The results were higly promising for cell differentiation and bone mineralization (Chen & Chang, 2011). rhBMP2-coated PS/PCL fibrous scaffold which was produced by electrospinning method for regeneration of bone tested through *in vitro* and *in vivo* studies by using human osteoblasts and rabbit mesenchymal stem cells. The results showed that regeneration of bone was achieved and 75 vol % bone defect was recovered after 8 weeks (Nguyen & Lee, 2013).

1.1.3 Bioceramics

Bioceramics are widely used in orthopedic implants including hard tissue replacement and other TE applications. They can be found in crystalline, semicrystalline and amorphous structures. The invention of bioceramics was in the 1960s as an alternative to the metallic implants because metallic implants caused some corrosion, inflammation or toxicity at the implanted tissue area (Eliaz, & Metoki, 2017). Bioceramics have been used for many years because bone is composed of inner cancellous bone and outer periosteum layer. Additionally, bone tissue includes osteoblast for bone formation, osteoclasts for breakdown of bone and osteocytes for regulating function of osteoblast and osteoclast in the bone matrix. Morever, bone matrix constitutes 70% HA ($Ca_5(PO_4)_3OH$), 20% organic compounds and 10% water (Rödel et al., 2018). Thus, CaPs have similar chemical and physical properties with HA. In this respect, bioceramics have been used in hard tissue replacement and drug delivery applications for bone defect or coatings on metallic implants (Rödel et al., 2018). Bioceramics can be modified in size and structure to treat bone fractures, osteomyelitis, bone tumors and osteoporosis. Bioceramics are categorized into bioinert, resorbable and bioactive based on their responses in the body. In this respect, bioinert materials such as zirconia, stainless steel, titanium, alumina,

Si_3N_4 and carbons don't react with surrounding tissues. These materials can cause formation of some fibrous capsule around the implanted area which results in osteolysis and pain (Heness & Ben-Nissan, 2015). For example; stainless steel and cobalt-chrome alloys were used in the orthopedic applications including total hip prosthesis in the 20th century. Stainless steels consist of chromium which provides adherence, self-healing and resistance to corrosion but their mechanical properties didn't meet the requirements for load bearing applications. Then, Ti and Ti based alloys were started to be used in 1940s and they had become focus point because of their better mechanical properties and appropriate Young's modulus (eg. 110 GPa) (Navarro et al., 2008). Ti and Ti6Al4V were then used for orthopedic applications. Additionally, commercial Ti screws were used for treating rabbit bone in 1952. This experiment provided understanding of osseointegration phenomenon and bone formation in the dental applications. Alumina has been used in femoral heads or stems and dental implants because of its high hardness and inertness. However, alumina is brittle and its low tensile strength causes microcracking (Heness & Ben-Nissan, 2015) . Thus, it is highly recommended for use in dental applications. Zirconia which is also another inert material as an alternative to alumina used in orthopedics and dental applications due to its better fracture toughness, resistance to fatigue, bending strength and mechanical strength. However, sintering of zirconia leads to some problems related with volume shrinkage which resulted in residual stress and microcracking. This can be solved by addition of yttrium oxide as a stabilizing agent with a fine grain size and microstructure used for the application of femoral head of total hip joint replacement.

Carbonaceous materials are referred as first generation bioinert ceramic materials. They are highly resistant to wear and fatigue. They are not toxic to cells but they are not suitable for orthopedic applications because of their brittleness and low tensile strength. Thus, they were widely used in the heart valve and musculoskeletal reconstruction applications. The second generation bioceramics include silicate-based bioactive inorganic or organic composites because silicon is very important for bone and cytoskeleton regeneration in the human body, synthesis of collagen, essential component of connective tissues and good impact

for protein phosphorylation, nucleotides and saccharides (Zhou et al., 2016). In that sense, silicate-based bioceramics have a great potential for bone tissue regeneration because of their improved biological and mechanical properties and are found in the form of fibers, membranes, scaffolds, hydrogels and coating. Bioactive silicate-based bioceramics are categorized as silica based bioactive bioglasses in 1982 and its composition is 45 wt% of SiO_2, 24.5 wt% of CaO, 24.5 wt% of Na_2O and 6 wt% of P_2O_5. It is not applicable in the load bearing implants because of its low tensile strength (42 MPa) which is half of human cortical bone tensile strength. Thus, it is widely used for peridontal fillers. Silica based bioglasses induce bone regeneration, proliferation and osteogenic differentiation by releasing Si and Ca ions. In this respect, bioglasses were used for the first time in 1985 as vertebral prostheses. In this clinical study, apatite-wollastonite glass ceramics were produced with better Young's modulus, bending strength and fracture toughness. However, poor mechanical strength of silica based inorganic biomaterials led to brittleness when compared to CaP based bioceramics. This problem can be overcome by combining other ceramic, metal and polymers. This also helps to control the degradability of ions in the composite. CaP based bioactive composites were started to be used in 1890s for the medical applications without any promising results. Then, TCP was used for bone formation in 1920s by A Albee & Morrison, (1920) and results were potential use in the bone formation applications. In this respect, CaPs and bioglasses were osteoconductive and their usage in artificial bone grafts applications became popular in 1970-1980s. CaP based bioceramics like HA and β-TCP exhibit good biocompatibility in the living systems by forming chemical bonds without causing any encapsulation in fibrillary tissues which resulted in stimulation of tissue generation (Albulescu et al., 2019). However, pure HA has poor mechanical properties. This problem can be solved by addition of other cations including Na^+, Sr^{2+}, Mg^{2+} and Zn^{2+} and anions like $(CO_3)^{2-}$, $(SiO_4)^{4-}$, F^- and CI^-. This enables them to gain antimicrobial activity, delivery of drug and angiogenesis or osteogenesis induction which is also desired in orthopedic and dental applications (Albulescu et al., 2019). The solubility and pH stability at 25ºC of calcium orthophosphates are represented in Table 1.1. If the Ca/P ratio is less than 1,

implantation is not suitable for the body because of their higher acidic properties and solubility. Thus, they cannot be used as biomaterials but combination with other calcium orthophosphates or chemicals can solve this problem (Dorozhkin, 2010).

Table 1.1 Ca/P molar ratio, formula and solubility of various CaPs (Dorozhkin, 2010)

Ca/P Molar Ratio	Compound	Formula	Solubility (25 °C, g/L)
0.5	Monocalcium phosphate monohydrate (MCPM)	$Ca(H_2PO_4)_2.H_2O$	~18
0.5	Monocalcium phosphate anhydrous (MCPA)	$Ca(H_2PO_4)_2$	~17
1.0	Dicalcium phosphate dihydrate (DCPD)	$CaHPO_4 \cdot 2H_2O$	$\sim 8.8 \times 10^{-2}$
1.0	Dicalcium phosphate anhydrous (DCPA)	$CaHPO_4$	$\sim 4.8 \times 10^{-2}$
1.33	Octacalcium phosphate (OCP)	$Ca_8(HPO_4)(PO_4)_2.4 \cdot 5H_2O$	$\sim 8.1 \times 10^{-3}$
1.5	α-TCP	$\alpha\text{-}Ca_3(PO_4)_2$	$\sim 2.5 \times 10^{-3}$
1.5	β-TCP	$\beta\text{-}Ca_3(PO_4)_2$	$\sim 5 \times 10^{-4}$
1.2-2.2	Amorphous calcium phosphate (ACP)	$Ca_xH_y(PO_4)_z \cdot nH_2O$ n=3–4.5	[a]
1.5-1.67	Calcium-deficient hydroxyapatite (CDHA)[b]	$Ca_{10-x}(HPO_4)_x(PO_4)_{6-x}(OH)_{2-x}$ $(0<x<1)$ [c]	$\sim 9.4 \times 10^{-3}$
1.67	HA	$Ca_{10}(PO_4)_6(OH)_2$	$\sim 3 \times 10^{-4}$
1.67	Fluorapatite (FA)	$Ca_{10}(PO_4)_6F_2$	$\sim 2 \times 10^{-4}$
2.0	Tetracalcium phosphate (TTCP)	$Ca_4(PO_4)_2O$	$\sim 7 \times 10^{-4}$

a Cannot be measured precisely. However, the following values were found: 25.7±0.1 (pH=7.40), 29.9±0.1 (pH =6.00), 32.7±0.1 (pH=5.28). The comparative extent of dissolution in acidic buffer is: ACP>>α-TCP>>β-TCP>CDHA>>HA> FA.

b Occasionally, CDHA is named as precipitated HA.

c In the case x=1 (the boundary condition with Ca/P=1.5), the chemical formula of CDHA looks as follows: $Ca_9(HPO_4)(PO_4)_5(OH)$.

1.1.3.1 Zinc-doped Hydroxyapatite

Synthetic HA has been widely used due to its similar structure with inorganic part of the bone and easy synthesis methods. This makes synthetic HA a good candidate for bone tissue engineering (BTE). Additionally, it can be easily doped with other ions to improve its antibacterial, biological and mechanical properties. In this respect, HA can be mixed with other polymers or doped with ions to improve its properties because of presence of vacancies in the structure including cationic and anionic vacancies (Rey et al., 2009). One of doping elements is zinc which is a vital element in the biological system. Zinc is found in enamel or dentine and it stimulates new bone formation after implantation by reducing contamination and infection effects (Ofudje et al., 2019). Zn doped apatite has been shown to exhibit improved biocompatibility with osteoblasts, human-adipose-derived mesenchymal stem cells and antibacterial property. It also decreases the instability in the interfacial region of bone-implant. In a study, it was shown that Zn doping with an amount of 0.316 and 0.633 wt% in the TCP prevented the resoption of bone by mature osteoclasts at the bone-implant interface by downregulating 0.5 fold the mRNA expression of CAII and 0.6 fold cathepsin K/OC2 in the osteoclast compared to the TCP (Yamada et al., 2007). Additionally, ALP activity of bone marrow cells (BMCs) was enhaced by addition of 1.26 wt% zinc content in the TCP/HA composite. There is no cytotoxic effect up to concentration of 1.26 wt% zinc amount (Ikeuchi et al., 2003). Besides, substitution amount of Zn into hydroxyapatite is very important because addition of higher amount can lead to some cytotoxic effect and decrease the crystallinity of the structure by increasing TCP phases. Additionally, release of calcium and phosphate is reduced when the substitution amount of zinc is increased. Thus, the amount of Zn shouldn't exceed the 1.6 wt%. In a study, the optimum zinc content in the Zn HA structure was found to be 0.34% for increasing the cell proliferation (Sogo et al, 2004). Additionally, antibacterial and antifungal characteristics of Zn doped HA was reported with many studies (Stanić et al., 2010; Thian et al., 2013; Wang et al., 2010). In a study, Stanić et al. (2010) investigated the antimicrobial activity of zinc doped HA against *Escherichia coli*, *Staphylococcus aureus* and pathogen yeast *Candida albicans* with agar diffusion and liquid challenge in

buffer solution methods. The results showed that zinc doped HA enabled reduction of viable cells in the all three microorganisms. In another study, antimicrobial activity of Zn doped HA was analyzed against *Staphylococcus aureus* and *Escherichia sp.* by using different concentrations of Zn. Presence of Zn in HA increased its antimicrobial activity (Ofudje et al., 2019). Thian et al. (2013) evaluated the biological activity of 1.6 wt% Zn doped HA through in vitro studies using human adipose-derived MSCs and also antimicrobial activity towards *S. aureus* bacteria. *In vitro* cell studies of Zn-HA and HA showed that Zn-HA enabled increment in the human adipose-derived MSCs and improvement in the bone cell diffrentiation markers. There was a significant increment in the COL expression in the presence of Zn-HA at 14 and 21 days. Hence, the antimicrobial activity of Zn-HA towards *S. aureus* bacteria showed enhanced decrease in the number of bacteria after 6 days when compared to pure HA.

1.1.3.2 Boron Nitride Nanostructures

Carbon nanostructures are one of the most widely searched materials which are also used in different areas from electronic to biomedical field because of their exceptional physical and chemical properties. However, after discovery of boron nitride (BN) nanoparticles, BN nanostructures surpass attention of the carbon-based nanostructures because of their enhanced thermal and chemical stabilities in addition to structural similarity with the carbon nanomaterials. Among these nanostructures, one dimensional-BN nanostructures are on the verge of development as new materials to fulfill some necessities for different application areas due to their excellent and unique properties including their tunable surface and bandgap, electronic, optical, mechanical, thermal and chemical stability characteristics (Pakdel et al., 2014; Wang et al., 2017). They are composed of boron and nitrogen ions with different crystal lattice structures such as hexagonal boron nitride (h-BN), cubic boron nitride (c-BN) and wurtzhite BN (w-BN). BNs show superior mechanical strength and thermal resistance at high temperatures (Haubner et al., 2002). Thus, they can be used in corrosion resistant jigs, transistor heat sinks, nuclear reactor control rods, crucibles for metal evaporation and neutron absorber because of their unique thermal, electrical and chemical

properties (Haubner et al., 2002; Weng et al., 2016). Crystal structure of c-BN and h-BN is very important for industrial applications. Structure of c-BN is very similar to that of diamond, the second hardest material and it is used as coating on cutting and drilling tools. However, c-BN has higher thermal properties and chemical inertness than diamond (Monteiro et al., 2013). There are different synthesis methods for c-BN. One of them is a direct transformation of h-BN to c-BN at high pressure and temperature using different catalysts such as Mg or Ca (Bundy & Wentorf, 1963). For coating applications, chemical vapor deposition (CVD) and physical vapor deposition (PVD) methods are used to produce c-BN to improve the lifetime of devices (Bundy & Wentorf, 1963; Bundy et al., 1965; Guo et al., 2010). Besides, properties of c-BN are different than those of h-BN. Layered structure of h-BN becomes very similar to that of graphite when B and N atoms are replaced with C atom. C-C bonding in the graphite crystal structure is weaker than ionic bonding between B and N due to differences in electronegativity (Shore, 1968). Additionally, h-BN consists of a network of B_3N_3 hexagons. There is van der Waals interaction between the layers with a space of 0.333 nm. h-BN is used for production of nanostructures other 1D BN nanostructures including nanotubes, nanorods and nanofibers.

1.1.3.2.1 BN Nanotubes

Structure and mechanical properties of BN nanotubes (BNNTs) are very similar to those of the carbon nanotubes (CNTs) (Hernández et al., 1998; Kudin et al., 2001). However, BNNTs have some advantages over CNTs in terms of their unique electronic properties with a tunable band gap (Blasé et al., 1994; Rubio et al., 1993), resistance to high temperature without oxidation (Golberg et al., 2001) and capability of hydrogen storage (Jhi & Kwon, 2004). This makes BNNT a good candidate material for energy storage and other applications. Today, many synthesis methods have been reported and developed with high quality mass-production of BNNTs (Kim et al., 2018). There are various BNNT synthesis methods including arc discharge (Chopra et al., 1995; Loiseau et al., 1996; Terrones et al., 1996), laser ablation (Lee et al., 2001; Yu et al., 1998), ball milling (Chen et al., 1999), CVD (Lourie et al., 2000). There are studies on

BNNTs for TE applications. In one of these studies; it was reported that chitosan/BNNT-OH scaffolds significantly increased adhesion and proliferation of human dermal fibroblast (4 fold) after 7 days of incubation with respect to chitosan scaffolds without causing any cytotoxic effect. Cell viability (115 %) on chitosan/BNNT-OH scaffolds was significantly higher than observed in the control group (chitosan based) (Emanet et al., 2016).

In another study, BNNT–DSPE-PEG2000 was used in BNCT by using B16 melanoma cell line to investigate antitumor effect of BNNTs. These results showed that accumulation of BNNT–DSPE-PEG2000 in B16 melanoma cell line was three times higher than BSH (sodium mercaptoundecahydrododecaborate) which is used for a clinical treatment for glioblastoma patients in BNCT as a control. Thus, killing efficiency of BNNT–DSPE-PEG2000 was better than control groups and this composites were very good candidates as boron source in BNCT (Nakamura et al., 2015).

In nuclear medicine therapy, da Silva et al., (2018) investigated samarium 152 doped BNNTs as a nano-sized β- emission source in the nuclear medicine field. The results showed that samarium 152 doped BNNTs didn't cause any cytotoxic effect on MRC-5 fibroblasts and cell viability was higher than the 70%. As a result, the authors suggested that this material can be used as a nano-sized β-emission source in the nuclear medicine field. BNNT reinforced polylactide–polycaprolactone copolymer (PLC) composites were investigated for mechanical strength, viability and Runx2 gene expression of osteoblasts. PLC was reinforced with 2 and 5 wt% of BNNTs to be used in orthopedic applications. Young's modulus and tensile strength of PLC were enhanced 1370% and 109%, respectively by the addition of 5 wt% BNNT. The results showed that viability of human osteoblasts ATCC CRL-11372 (ATCC, Manassas, VA) was enhanced by 30%. Additionally, mechanical and tribological properties were significantly higher with addition of 5 wt% BNNT without causing any side effect when compared to copolymers. These results strengthened the idea of their potential usage in the orthopedic implants (Lahiri et al., 2010).

BNNTs were used as nanofillers in resin based dental applications (Bohns et al., 2019; Degrazia et al., 2017). In one of these studies, methacrylate-based adhesive resin was used for the dental applications. BNNTs were incorporated in the polymeric matrix including bisphenol A-glycol dimethacrylate (BisGMA) and hydroxyethyl methacrylate (HEMA) with concentrations of 0.05, 0.075, 0.1 and 0.15 wt%. Bioactivity of these scaffolds was verified by SBF experiments conducted for 7 days. Based on the SEM analysis, it was shown that both amorphous and crystalline HA precipitations were higher on the scaffolds when compared to methacrylate-based adhesive resin. Additionally, ultimate strength of the scaffolds was increased from 52.28 to 65.47 MPa by the addition of 0.15 wt% of BNNTs. This study revealed that addition of up to 0.15wt% of BNNTs enhanced the mechanical, chemical and cell adhesion and matrix deposition by the cells (Degrazia et al., 2017). However, BNNTs were used at low concentrations in these studies. To investigate the cytotoxic effect of BNNTs, Horváth et al., (2011) used BNNTs at higher concentration by analyzing the morphology of cells (epithelial cells (A549) and macrophages (RAW 264.7)) through SEM examination. There were some rearrangements of microvilli on the surface of the cells which led to spreading of the particles irregularly. Other cells experienced rounding, surface blebbing and detachment. The morphology of RAW 264.7 was spindle-shaped and spherical which depends on the adherence of the cell substrate. High-resolution SEM revealed the ultrastructural modification on the surface of the A549 epithelial cells after they were treated with BNNTs. This structural change can be related with cytotoxicity mechanism which is still unclear.

1.1.3.2.2 BN Nanofiber (BNNF)

Nanofiber structures are advantageous over nanoparticles and 2D structures because of their porous structure and high surface area which provides filter, protective and adsorption layer (Subbiah et al., 2005). This affects their usage in material science, electronics and polymer engineering (Subbiah et al., 2005). Among 1D structure, BNNTs have been widely studied by many researchers in many different areas including hydrogen storage (Ma et al., 2002; Oku & Kuno, 2003), nanofillers (Zeng et al., 2017; Zhi et al., 2006), water treatment (Cho et al.,

2020; Hilder et al., 2009) biosensor (Huang et al., 2009) and TE (Rocca et al., 2016; Salvetti et al., 2015) with desired morphology, large amount of production, low cost and high purity (Lin et al., 2016). Thus, these BNNTs studies which are the main member among 1D BN nanomaterials gave promising insight for potential usage of BNNFs in many different areas because of their unique properties and easy synthesis method. Especially, continuous and well aligned BNNFs which are produced electrospinning or rotary jet methods have better performance to improved thermal properties (Qiu et al., 2009a). According to TGA analysis, BNNFs can stand 890°C without any oxidation when compared to BNNTs and BN nanoparticles. Additionally, in another report, BNNF membranes which were produced from BN/PVA had a higher bandgap energy (4.52 eV) compared to that of BN nanoparticles (2.75 eV). This bandgap differences lead to different optical and electrical properties (Hwang et al., 2010). This enabled BNNFs to be used as a reinforcement agent in the polymeric precursor for the application which requires high insulating and thermal conductive properties (Guo et al., 2019). High oxidation and decomposition resistance of BN structures were explained by production methods, presence of defects, purity and partially ionic characters between the B-N bonds which creates strong electric field (Chen & Zou, 2004; Mahajan et al., 2013; Xu et al., 2009). Additionally, large-scale amount BNNFs can be produced with well aligned long structure through multijet/multicollector methods without causing any impurity and defects. This method enables commercialization because of its efficient, simplicity and easy to scale up while production methods for BNNTs are not easy to scale-up with desired morphology (Qiu et al., 2009a). Also, chemical structure of BN nanostructures is very similar to that of carbon nanostructures but BN nanostructures have B-N bonds which are ionic rather than covalent bond in carbon nanostructures. This alters its molecular orbital configuration and then molecular and solid-state electronics and also optical properties. BN nanostructures have some advantages over carbon nanostructures in terms of their unique electronic properties with a tunable band gap, resistance to high temperature without oxidation and capability of hydrogen storage (Dolati et al., 2012; Rubio et al., 1993). Besides, BN nanostructures are highly biocompatible

and widely studied in biomedical applications while carbon nanostructures including fullerenes, single- andmulti-walled carbon nanotubes have problems with cytotoxicity due to their shape and concentration (Lewinski et al., 2008). There are studies about usage of BNNFs in TE. As an example; Nagarajan et al. (2017) investigated gelatin/BN ESM to improve mechanical properties of gelatin and tested by using HOS osteosarcoma cells. In this respect, gelatin/BN ESM enhanced Young's modulus, cell attachment and proliferation without causing any cytotoxic effect according to cell viability assay, osteoblast gene expression, fluorescent imaging and ALP activity of HOS cells gelatin nanofibers. In another study, biocomposites of HA, chitosan (Cs), type 1 collagen (Ct1) and h-BN were used for recovery of bone fracture healing in the male Wistar rats. Biocomposite of HA/h-BN/Cs/Ct1 was used as a coating material on the stainless steel. The results revealed that this biocomposite didn't cause any cytotoxic effect in the fracture when compared to stainless steel as a control group based on the results of clinical, radiographic, haematological, biochemical, and histopathological findings (Deveci et al., 2020).

1.2 Composites

Composites are made of two or more different materials with distinct chemical or physical properties (Rahaman et al., 2018). In TE, to eliminate cytotoxicity problems of some materials, composites of synthetic polymers and bioceramics were produced. These composites enable enhanced mechanical, bioactivity, degredation rate and ion release (Song et al., 2007).

1.3 Studies on Biomaterials Subjecting Bone Tissue Engineering

Bone defect treatment has been studied by many research groups by using different composites of polymers and bioceramics. In a study, poly(ε-caprolactone) (PCL) was mixed with nano-HA through rotaryjet spinning (RJS) in order to improve lamellar bone formation and this was tested through *in vitro* and *in vivo* studies. For this purpose, 15 wt% of PCL solution in the chloroform was prepared and then nHA was added into this solution at an amount of 3, 5 and 20 wt%. The PCL/nHA fibers were obtained using aluminum collector of reservoir

with a constant rotation at 7500 rpm. Biocompatibility of PCL, PCL/3% nHA, PCL/5% nHA, and PCL/ 20% nHA was tested using rat mesenchymal stem cells (rMSCs). All scaffolds didn't show any cytotoxicity with respect to control group. Moreover, ALP levels of cells seeded on PCL/20% nHA were higher than those of PCL group. Additionally, formation of mineralized nodules visualized by alizarin red staining was high for PCL/ 20% nHA scaffolds which showed the existence of calcium and enhanced bone mineralization. *In vivo* studies were conducted by using 6 adult male rats (Rattus norvegicus, albinus, Wistar, 270–300 g, aged three months) for all groups. The histological staining results indicated that all scaffolds were cytocompatible with new bone neoformation in the defect area (Andrade et al., 2019). In another study, in vitro cell studies of polycaprolactone/ HA (PCL/HA) scaffolds fabricated by sol–gel method showed adhesion and proliferation of MC3T3-E1 cell lines. Results indicated that cell proliferation on the PCL/HA scaffolds were 30% higher than that of tissue culture polystyrene (TCPS) (Fabbri et al., 2010).

In another study, *in vitro* and *in vivo* studies were conducted on electrospun PCL/HA scaffold to repair calvarial defects. It was reported that PCL/HA scaffolds enabled better support for new bone formation during 6 weeks when compared to control and only PCL groups. *In vitro* cell culture studies were performed using human bone cells. Cells were seeded on PCL and PCL/HA scaffolds and cultivated for 24 h and 48 h. Cell viability was higher on the PCL/HA scaffolds (Chuenjitkuntaworn et al., 2010). Positive effect of PCL addition into the scaffold with and without HA was investigated in the bone formation of femural defect of rabbit through *in vivo* studies. In this respect, HA and PCL scaffold nanocomposites were used for femoral defect in rabbit. Histopathological results after implantation period of 45 days showed that the quantity of lamellar bone formation in the defect site for PCL/HA groups was higher than that of only HA and control groups (Eftekhari et al., 2017).

In another study, importance of presence of HA in the PCL composite was investigated for cell proliferation by (Groppo et al., 2017). Addition of HA into PCL nanofibers obtained by electrospinning enhanced the bone formation process

in vivo studies of rat calvarias with a faster response of body without causing any cytotoxic effect. There were more bone formation in pure PCL and PCL/HA groups with respect to groups of the blood clot with or without HA. In another study, Vasconcellos et al. (2020) produced PCL/nHA by rotary jet spinning to enhance biomechanical properties of new bone. In this respect, PCL/5% nHA and PCL/20% nHA were used for *in vivo* cell studies using twenty adult male wistar rats. Results showed that healing of rat tibia defects in the groups of PCL/5% nHA and PCL/20% nHA was faster than that of clot (control group). Also, new bone formation was better in PCL/20% nHA groups where initial development of Havers system indicates the maturation of bone tissue and improved biomechanical properties (Vasconcellos et al., 2020).

To investigate the effect of doping into HA with different ions for attachment and proliferation of cells in the BTE, HA co-doped with Zn^{2+} and F^{-} ions were analyzed by Uysal et al. (2014). The results asserted that co-doped HA improved microhardness, density, fracture toughness, adhesion and proliferation of Saos-2 cells compared to HA. Moreover, Ghorbani et al. (2015) demostrated that presence of 5wt% ZnHA in PCL/Ch/ZnHA nanocomposites significantly improved the attachment of human adipose derived stem cells (hAD-MSCs) when compared to PCL/Ch and PCL/Ch/nHA groups. Additionally, Young's modulus and tensile strength of the scaffolds increased 3-folds and 1.5 folds, respectively by the addition of 5 wt% of ZnHA. Additionally, higher adhesion and proliferation of MG-63 osteoblast cells on Zn-doped HA were verified than that of HA. This makes it suitable for orthopedic and dental applications (Begam et al., 2017).

Moreover, ZnO doped HA was used in the composite of poly(L-lactic acid)-co-poly(ε-caprolactone) (PLCL) and silk fibroin. The results showed that poly(L-lactic acid)-co-poly(ε-caprolactone) (PLCL), silk fibroin and ZnO doped HA were shown to improve proliferation of osteoblasts significantly *in vitro* than that of control group of PLCL (Gnaneshwar et al., 2019). Hence, doped HA was used as a coating material for BTE. For example, human osteoblast adhesion and proliferation were tested by using Zn-doped HA coated on titanium implant

through *in vitro* cell. The significant increment in adhesion and spreading of cells was observed with the use of 7 mol% Zn-doped HA as a coating material than that of HA. Additionally, morphology of HOB was elongated and polygonal shape based on the SEM analysis (Ortiz et al., 2016). In another cell study, 5 mol% and 10 mol% Zn-doped HAs were studied as a coating material on Ti6A14V by using human osteoblast Saos-2 cells. Additionally, antimicrobial effect was also analyzed by *E. coli* and *S. aureus* without causing any cytotoxic effect. These findings make Zn-doped HA a potential coating for Ti6A14V surfaces in order to use them in biomedical implants (Sergi et al., 2018). In another study, osteogenic activity of osteoblast cell was investigated by using the composite of titanium which was coated with Zn-doped HA/calcium silicate through *in vitro* studies. In this study, MC3T3-E1 cells were seeded on ZnHA/CS scaffolds and viability and osteogenic differentiation of the cells were analyzed by MTT and ALP activity assays. The findings showed that coating of ZnHA/CS on titanium resulted in higher proliferation and spreading of MC3T3-E1 cells without causing any cytotoxicity with respect to HA coating (Huang et al., 2015).

1.4 Scaffold Processing

In TE, scaffolds have to guide cells for growing and spreading. For this reason, they play a vital role for creating an environment which has to be conductive for attachment, spreading of cells and formation of new tissues. There are some requirements for ideal scaffolds to be used in bone-tissue engineering applications. Firstly, proper pore size, high surface area and surface permeability are required for attachment cells and accumulation of ECM. Secondly, appropriate degradation rate should match the rate of neotissue generation while byproducts have to be eliminated from body through physiological metabolic process. Thirdly, scaffolds must be biocompatible without causing any cytotoxic effect to cells. Fourthly, mechanical properties of scaffolds have to match with mechanical strength of tissue. Fiftly, proper surface properties including roughness are required for attachment, growth, migration and differentiation of cells (Ma, 2004). There are many techniques to produce scaffolds for biomedical applications

including rotary jet spinning, electrospinning, sol-gel method, solvent casting, compression molding, melt molding, 3D printing, etc.

1.4.1 Rotary Jet Spinning (RJS)

Rotary jet spinning is known as centrifugal or force spinning because it uses mechanical force instead of electrical force to expel solution in order to fabricate nanofibers. Additionally, large scale nanofiber with 3D aligned structures production can be achieved from different polymers in a short time. Badrossamay et al., (2010) used this system for the first time to produce aligned nanofiber. This system includes reservoir by 2 side wall orifices connecting to the shaft of motor with an adjustable rotational speed (Figure 1.2). Fiber can be collected on the flexible air foil which is located on the shaft. The reservoir has to be fed by polymer solution continuously with a stable rate in order to sustain a steady hydrostatic pressure and flow. The formed nanofibers are collected from both on cylindrical collector or on coverslip which is held towards collector wall. This process includes three main steps. Firstly, jet is initiated for stimulating flow of polymer solution into the orifice. Secondly, jet is extended in order to increase surface area of repelled polymer stream. Thirdly, solvent evaporation was achieved to solidify and minimize the size of polymer jet. There are some challenges which are related to preventing jet rupture, formation of droplets and ultrafine fibers in this process because of viscoelasticity, surface tension, solvent volatility, collector radius and capillary diameter. RJS is a technique used for production of nanofiber (Badrossamay et al., 2010). This system has some adventageous over other fabrication methods. One of them is that there is no usage of high voltage electric fields which increases the agglomeration of particles in the structure because of electrostatic interaction. Also, the used apparatus is simple to apply for polymer solution with desired aligned 3D structure or beaded, smooth and textured morphology, porosity and diameters of fibers can be adjusted just by

changing the variables of process. In this way, production of continuous, nonwoven and high production amount of fibers can be achieved with nanometer size by applying high speed mechanical rotation of polymeric solutions

(Badrossamay et al., 2010). The other works achieved through the rotary jet spinning were summarized in Table 1.2.

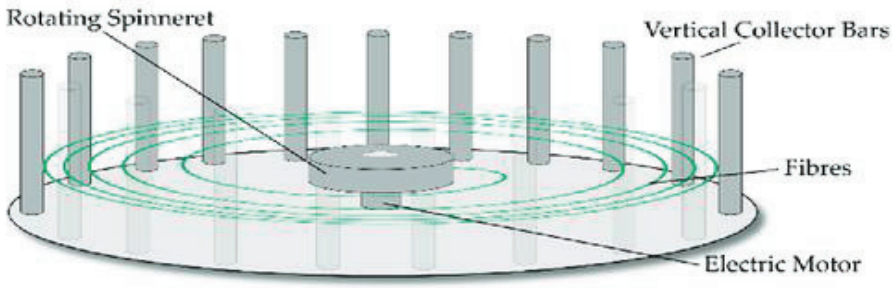

Figure 1.2 An illustration for rotary jet spinning system (Rogalski et al., 2018)

Table 1.2 The usage of rotary jet spinning in tissue engineering

	Rotary	**Rotary**	**Rotary Jet**	**Rotary Jet**	**Rotary Jet**
Reagents	Poly(vinylamine) (PVAm)	PLA	PLA	PCL-collagen, PCL-gelatin	Alginate:gelatin
Composition	8 wt%	4-9 wt%	4 wt%	(75:25), (75:25, 50:50, 25:75)	50 wt%
Rotation Speed (RPM)	6.000- 8.000	4.000-37.000	12.000	30.000	30.000
Product Properties	The obtained PVAm fibers used in the PVAm-based molecular imprinting nanofibers (MINFs) of bisphenol A (one endocrine disruptor) recognition with a higher recognition with a higher recognition and selectivity to smart materials.	The obtained aligned PLA fibers with a diameter of 150 nm has uniform morphology without bead formation at 35000 RPM.	Aligned and nonwoven PLA fibers were produced with a diameter of 424 nm. PLA fibers indicated improved attachment and proliferation of myocytes by orienting their contractile cytoskeleton and self-organizing into a beating.	PCL/Collagen aligned fibers showed enhanced cardiomyocytes, neurons and valve interstitial cells attachment and proliferation than that of only PCL fibers.	Aligned blended alginate–bioprotein nanofibers were produced with enhanced C2C12 myoblasts cell attachment, proliferation, and differentiation.
References	(Wu et al., 2019)	(Mellado et. al., 2011)	(Badrossamay et al., 2010)	(Badrossamay et al., 2014)	Gonzalez et al., 2017)

1.4.2 Electrospinning

Electrospinning uses electrical forces to fabricate nanofibers by using both natural and synthetic polymers. In this system, polymeric solution is put into syringe and system starts to pump at a constant rate. Then high electrical voltage (tens of kV) is applied at the tip of syringe to form a droplet of liquid and cone shape is formed which is known as Taylor cone in Figure 1.3. When the applied voltage overcomes the surface tension of polymer solution, polymer solution is ejected from the tip of syringe and move to the collector (Bhardwaj & Kundu, 2010). In this method, concentration of polymer solution, distance between collector and needle, applied voltage and flow rate of polymer solution are very important parameters for the production of 3D porous nanofibers (Bhardwaj & Kundu, 2010).

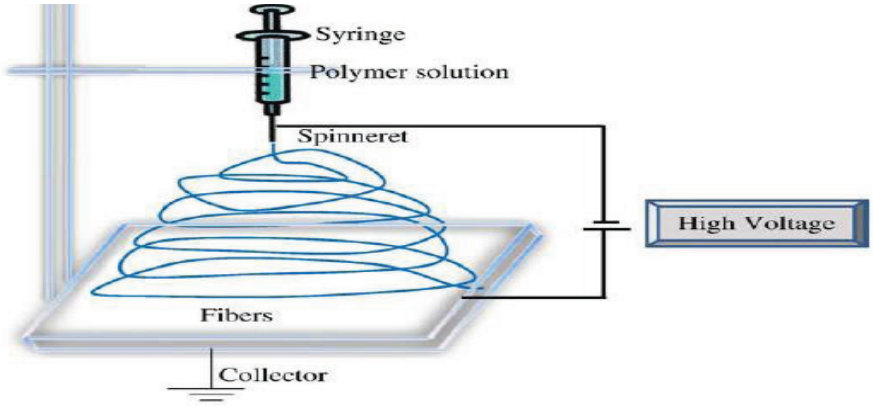

Figure 1.3 An illustration for electrospinning system (Bhardwaj & Kundu, 2010).

1.5 Aim of the Study

Since tissue injuries are beyond natural healing process and conventional treatments are not efficient, bone repair can be achieved by scaffolds. New composite scaffolds are still needed and under focus by many research groups from academia and industry for BTE applications. In this thesis, it was aimed to develop scaffolds of poly-ε-caprolactone (PCL) reinforced with Zn-doped hydroxyapatite (Zn-HA) and BNNF using rotary jet spinning to mimic bone tissue to enhance adhesion, proliferation and functionality of cells. BNNF and Zn HA were incorporated into the PCL scaffolds owing to mechanical stability, hardness, chemical inertnessa and enhanced wound healing of BNNF and antibacterial and osteoconductive properties of ZnHA. The hypothesis of the study was that PCL fiber scaffolds including (Zn-HA and BNNF) should give higher mechanical stability and cell viability based on the literature data. As the scaffold fabrication method rotary jet spinning method which has industrially applicability and reproducibility of large-scale production was chosen for obtaining scaffolds with aligned fibers. Firstly, synthesis of bioceramics including BNNFs and 1 wt% of Zn-HA were achieved by freeze drying and wet chemical method, respectively and then verified by characterization techniques including XRD, FTIR, SEM and ICP. Prepared scaffolds were characterized in terms of morphology, mechanical properties and degradation. At the final step, bioactivity and potency of the scaffolds as BTE constructs were investigated in terms of potency for bone regeneration by in vitro cell studies using Saos-2 cells.

CHAPTER 2

MATERIALS AND METHODS

2.1 Materials

Calcium nitrate tetrahydrate ($Ca(NO_3)_2.4H_2O$), diammonium hydrogen phosphate ($(NH_4)2HPO_4$), zinc nitrate hexahydrate ($Zn(NO_3)_2.6H_2O$), melamine ($C_3H_6N_6$), boric acid (H_3BO_3), poly(ε-caprolactone) (PCL) (Mn, 80 000), chloroform, cupric sulfate pentahydrate ($CuSO_4.5H_2O$), bicinchoninic acid, ascorbic acid, β-glycerophosphate, paraformaldehyde, sodium hydroxide (NaOH), hexamethyldisilizane nitric acid and dexamethasone were from Sigma Aldrich (USA). Ethanol, sodium chloride (NaCl), magnesium chloride hexahydrate ($MgCl_2.6H_2O$), potassium chloride (KCl), calcium chloride ($CaCl_2$), sodium bicarbonate ($NaHCO_3$), dipotassium hydrogen phosphate trihydrate ($K_2HPO_4.3H_2O$), hydrochloric acid (HCl), sodium sulfate (Na_2SO_4), hexamethyldisilizane (Merck, Germany), TRIS, disodium hydrogen phosphate dihydrate ($Na_2HPO_4.2H_2O$), dipotassium hydrogen phosphate (K_2HPO_4) and chloroform were purchased from Merck (USA). Saos-2 cell line was from ATCC (USA) whereas low glucose Dulbecco's modified Eagle medium (DMEM), fetal bovine serum (FBS), penicillin/streptomycin and trypsin/ethylenediaminetetraacetic acid (Trypsin/EDTA) were the products of Biological Industries (Israel). Alamar Blue and p- nitrophenyl phosphate (pNPP) were from Invitrogen, (USA), BSA (Bovine Serum Albumin) (PAA Laboratories GmbH), Triton-100X (Merck, Germany), Alexa Fluor™ 488 (Invitrogen) and Draq5 (Invitrogen) for Confocal analysis, paraformaldehyde powder (Sigma, USA) and hexamethyldisilazane (Sigma, USA) were used for cell fixation.

2.2 Methods

2.2.1 Synthesis of boron nitride nanofibers (BNNFs)

BNNFs were synthesized by freeze-drying with further annealing of the synthesized product (Lin et al., 2016). First, 4.64 g of H_3BO_3 and 3.15 g of $C_3N_6H_6$ were mixed in 250 ml of distilled water. The mixture was then annealed at 85°C for 4h. Following, the mixture was frozen by liquid nitrogen and lyophilized at -80°C. Dried white product was annealed at 1100°C for 4h under nitrogen atmosphere with a flow rate of 0.5 L/min to yield BNNF.

2.2.2 Synthesis of %1 Zn doped HA (Zn HA)

Zn doped nano-sized HA (Zn HA) was synthesized by mixing Ca and P sources followed by ultrasonication and aging (Barbosa et al., 2013). For this purpose, 200 ml of 0.167 M Ca source composed of 99 % ($^{mole}/_{mole}$) $Ca(NO_3)_2 \bullet 4H_2O$ and 1 % ($^{mole}/_{mole}$) $Zn(NO_3)_2.6H_2O$ was titrated with 200 ml of phosphate source containing 0.1 M $(NH_4)_2HPO_4$. During titration process, ammonia solution was added to the mixture to adjust pH to 10. After titration, mixture was subjected to ultrasound sonication with 250 Hz and 30% amplitude for 30 min. Then, the mixture was left for aging for 120h at room temperature. Following, aged mixture was filtered and rinsed with distilled water until pH 7.0 was reached. Finally, the precipitate was dried at 60°C for overnight.

2.2.3 Material Characterization

2.2.3.1 X-Ray Diffraction (XRD) Analysis

XRD spectra of synthesized BNNF and Zn HA were performed to determine the phases (Barbosa et al., 2013; Li et al., 2018; Lin et al., 2016). XRD spectra between 10-80° were recorded with 0.02°/second with CuKα radiation at 40 kV and 30 mA (PANalytical Empyrean, Netherlands).

2.2.3.2 Fourier-Transform Infrared (FTIR) Spectroscopy

FTIR spectroscopy (Bruker IFS66/S, USA) spectra were recorded between 4000-400 cm^{-1} in order to confirm h-BN structure in BNNF (Barbosa et al., 2013; Abidi & Murtaza, 2014) and functional groups present in Zn HA (Li et al., 2018; Lin et al., 2016).

2.2.3.3 X-Ray Photoelectron Spectroscopy Scanning Analysis (XPS)

The chemical state of BNNF and Zn HA was analyzed with XPS to confirm the B and N elements in BNNF and Zn, Ca and P ions in the structure of Zn HA with their binding energy (Qu et al., 2018;Liu et al., 2019 ;Ofudje et al., 2019).

2.2.3.4 Scanning Electron Microscopy (SEM)

Morphology of synthesized BNNF and Zn HA particles was investigated with SEM (Quanta 400F Field Emission SEM, USA). Prior to imaging, samples were coated with 10 nm ultra-fine gold particles by using precision etching coating system (Gatan 682 PECS, Gatan, Inc., USA) (Barbosa et al., 2013).

2.2.3.5 Particle Size Measurement

Particle size distribution and BNNF and Zn HA samples were analyzed (Malvern Mastersizer 2000, UK). Volume weighted particle size values were recorded from 3 different batches (Barbosa et al., 2013; Rupasinghe et al., 2012), (Li et al., 2018; Lin et al., 2016).

2.2.3.6 Inductively Coupled Plasma - Optical Emission Spectrometry (ICP-OES)

Elemental composition of Zn HA was investigated by ICP-OES (Perkin Elmer Optima 4300DV, UK) (Louyeh, 2016). For this purpose, samples were prepared by dissolving 100 mg of Zn HA in 5 ml of 20 % nitric acid solution. Then, samples were filtered and analyzed for presence of Ca, P and Zn.

2.2.4 Preparation of Scaffolds

Scaffolds were prepared by rotary jet spinning (RJS) (Guner et al., 2020). For this purpose, 15% PCL solution was prepared in chloroform. Following, PCL solutions with Zn HA only, BNNF only or with both Zn HA and BNNF were prepared (Table 2.1). Prepared solutions were propelled by an NE-1000 syringe pump (New Era, USA) into a custom made rotating reservoir (Mekoptronik, Turkey) and spun for 5 minutes with the settings as specified in Table 2.1.

Table 2.1 Composition and fabrication parameters of scaffold groups

Scaffold Group	PCL (%, $^{w}/_{v}$)	Zn HA (%, $^{w}/_{v}$)	BNNF (%, $^{w}/_{v}$)	Rotation (rpm)	Flow Rate (mL/min)
PCL	15	-	-	30000	2.5
PCL-Zn HA	15	0.150	-	30000	2
PCL-Zn HA-BNNF	15	0.075	0.075	30000	2
PCL-BNNF	15	-	0.150	30000	2

2.2.5 Characterization of Scaffolds

2.2.5.1 Fiber Morphology

Morphology of prepared scaffolds were visualized with SEM imaging. Samples were coated with gold as aforesaid. 200 fiber diameter was measured from obtained images by using the software ImageJ (USA). Mean fiber diameter was calculated from obtained measurements.

2.2.5.2 Tensile Test

Tensile test was performed on scaffolds (Akcay, 2012) by using Lloyd LS500 Univert mechanical tester (CellScale, Canada). Data was analyzed by using the computer program Univert (CellScale, Canada). 40 mm to 10 mm samples with 2 mm thickness and 10 mm radius were placed in grips so that gauge length would be 20 mm. Tensile test was performed with a crosshead velocity of 1 mm/min and under 1N load. Young's modulus, tensile strength and elongation at break were calculated by using stress-strain graph (Wittaya-Areekul & Prahsarn, 2006).

2.2.5.3 Compression Test

Compression test was performed on scaffolds by using Universal Instron Compression/Tension machine (METU, Turkey). Data was analyzed by using the computer program Univert (CellScale, Canada). The 3 cylindrical shaped samples with ~8 mm length and 4 mm diameter were placed in grips. The scaffolds were prepared by wrapping fibers around very tiny stick and then this stick was removed. The prepared scaffolds are cut into small cylindirical shape with 8 mm length and 4 mm diameter. The preparation steps are shown in Figure 2.1. Compression test was performed with a cross head velocity of 1 mm/min until 50 % strain was reached under 10 N load cells. Young's modulus and compressive strength was calculated by using stress-strain graph (Paşcu et al., 2013; Kim & Lee, 2011).

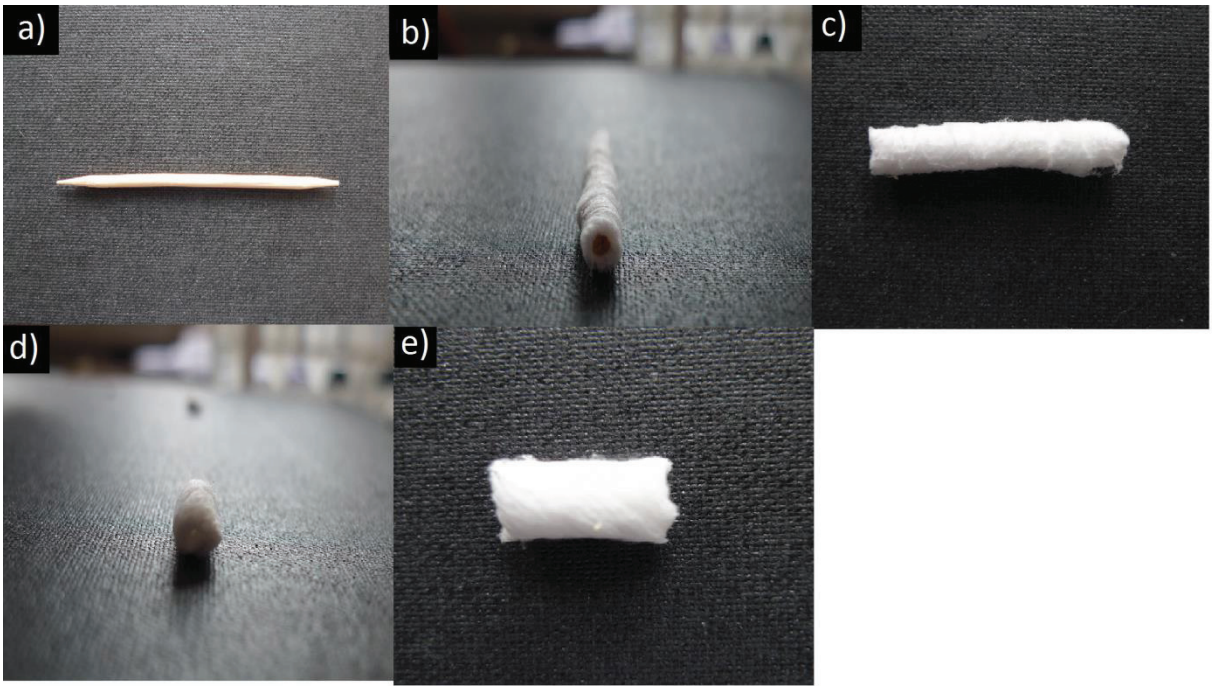

Figure 2.1 Preparation of the scaffolds for the compression test, a) stick with 0.5 mm diameter, b) front image after wrapping fibers around stick, c) top image after wrapping around stick, d) after removing stick from fibers, e) cutting of cylindrical shaped of fibers into small pieces with 4 mm diameters and 8 mm length

2.2.5.4 Biomineralization Test

In order to investigate biomineralization on scaffolds according to ISO/FDIS 23317 standard, 100 mg of composite fiber was weighed. Samples were incubated in 10 mL simulated body fluid (SBF) solution and incubated at 37°C for 14 days (Kokubo et al., 1990). Samples were taken out and dried at days 1^{st}, 4^{th}, 7^{th}, 11^{th} and 14^{th} dry samples were weighed to monitor weight change. Additionally, pH was monitored at each time point. Biomineralization on samples was also investigated with SEM at day 1^{st}, 7^{th} and 14^{th} days. Samples were coated with 10 nm ultra-fine gold particles by using precision etching coating system, prior to SEM imaging (Quanta 400F Field Emission SEM, USA)

2.2.6 *In Vitro* Cell Culture Studies

Cell culture studies were carried out by using Saos-2 cell line (ATCC, USA). Cells were cultivated with growth medium consists of low glucose DMEM supplemented with 10% FBS, and 1% penicillin/streptomycin. Cells were incubated in 37°C with 95% humidity and 5% CO_2 and media were changed every other day. Cell viability study was conducted with growth medium whereas osteogenic differentiation study was done with osteogenic media. Osteogeic medium was prepared by supplying DMEM/F12 with 10% FBS, 1% penicillin/streptomycin, 50 μg/ml ascorbic acid, 10mM β-glycerophosphate and 10^{-8} M dexamethasone (Pazarçeviren et al., 2020; Uysal et al., 2014).

2.2.6.1 Dose Dependent Cytotoxicity Test of BNNF and Zn HA

The BNNF and Zn HA powders in the crucible wrapped with aluminum foil were sterilized at 200°C for 2h MTT (3-(4,5-dimethylthiazol-2-yl)-2,5-diphenyltetrazolium bromide) assay was performed for 25 mg/ml of BNNF and 200 mg/mL of Zn HA to evaluate their cytotoxicity (Patel et al., 2013). For this purpose, extracts were prepared by incubating sterile 25 mg/ml of BNNF (500 mg in 20 ml sterile DMEM) and of 200 mg/ml of Zn HA (1500 mg in 7.5 ml sterile DMEM) for 24 hours. Saos-2 cells (ATCC, USA) were seeded in 96-well plate with a density of 1×10^5 cells/cm^2 and treated to varying concentrations of BNNF or Zn HA extracts for 24 hours at 37°C with 95% humidity and 5% CO_2 (MCO-

5M-PE, Panasonic, Japan). Untreated cells were used as control whereas not seeded wells served as blanks. MTT assay was conducted after 24 hours of treatment in order to determine cell viability. For this purpose, samples were interacted with 0.5 $^{mg}/_{ml}$ sterile MTT solution in phenol red free DMEM for 4 hours to allow formation of formazan crystals. After 4 hours, MTT solution in wells was discarded and formazan crystals formed inside cells were dissolved in DMSO for 30 minutes at dark. Dissolved formazan was transferred to a new well plate and absorbance at 570 nm was measured by using spectrophotometer (Paradigm Fluorescence Plate Reader, Molecular Devices, USA).

2.2.7 Cell Viability

Cell viabiltity was investigated by using Alamar Blue Assay (Pazarçeviren et al., 2020). Scaffolds were sterilized by incubation in 70% ($^{v}/_{v}$) ethanol for 1 hr followed by ultraviolet (UV) light for 1hr, each side. Cells seeded on tissue culture polystyrene (TCPS) were used as control group whereas scaffolds without cells were used as blanks. Sterile scaffolds that are 1 cm in diameter were seeded with cells at a density of 1×10^4 cells/cm^2 in 48 well plates. Alamar blue assay was performed at days 1, 4, 7, 11 and 14. Briefly, media in wells were replaced by 10% ($^{v}/_{v}$) alamarBlue^{TM} in DMEM without phenol red. Samples were then incubated at 37°C for 4 hours in dark. After 4 hrs, Alamar Blue solutions from the 48 well plates were transferred into a new 48-well plate to read absorbance at 570 and 600 nm by using a spectrophotometer (Paradigm Fluorescence Plate Reader, Molecular Devices, ABD) in the dark environment. The percent reduction was calculated in Equation 2.1 (Pazarçeviren et al., 2020). Then, wells were washed with PBS, before the addition of fresh media. Subsequently, cells on scaffolds were cultivated in the carbon dioxide incubator for the upcoming time point.

$$\text{Reduced } \% = \frac{((\varepsilon_{ox})_{\lambda 2} * A_{\lambda 1}) — ((\varepsilon_{ox})_{\lambda 1} * A_{\lambda 2})}{((\varepsilon_{red})_{\lambda 1} * A_{\lambda 2}) — ((\varepsilon_{red})_{\lambda 2} * A_{\lambda 1})} * 100 \qquad (2.1)$$

Where;

$(\varepsilon_{ox})_{\lambda 2}$= molar extinction coefficient (E) of oxidized alamarBlue at 600 nm

$(\varepsilon_{ox})_{\lambda 1}$= E of oxidized alamarBlue at 570 nm

$(\varepsilon_{red})_{\lambda 1}$= E of reduced alamarBlue at 570 nm

$(\varepsilon_{red})_{\lambda 2}$= E of reduced alamarBlue at 600 nm

$A_{\lambda 1}$= absorbance of test wells at 570 nm

$A_{\lambda 2}$= absorbance of test wells at 600 nm

Cell morphology on the scaffolds was investigated at days 1 and 14 by SEM examination. For this purpose, cells were fixed with 4% ($^{w}/_{v}$) paraformaldehyde in PBS for 15 minutes. Fixation was followed by washing with PBS and dehydration with ethanol series from 30 to 100% ($^{v}/_{v}$). Finally, samples were stored in a dessicator at 25°C. Imaging was performed after gold coating of samples as mentioned.

2.2.7.1 Confocal Imaging

In the confocal imaging, Alexa Fluor 488 and Draq5 fluorescent dyes were used for cellular imaging. Draq5 is far-red DNA stain for fixed cells. The Draq5 stain can be multiplexed with other fluorophores because of its far-red excitation and emission. It is lipophilic and can cross membranes of nuclear and cells in the fixed cells by staining DNA rapidly. This stain is water-soluble easily without requiring RNase, cell lysis or washing steps so Draq5 fluorescent probe is added in the last step. In short, it is used to visualize cells by counterstaining nuclei (Smith et al., 2000).

Alexa Fluor 488 dye is bright green-fluorescent dye. It is used for staining the cytoskeleton by binding the phalloidin to F-actin in the fixed and permeabilized cells because of toxicity of phalloidin (Lengsfeld et al., 1974). Before staining procedure, fixation of cells was performed to cease decomposition of cells and freze cellular proteins and subcellular structures in place. Firstly, 10.000 cells were seedeed for each 48 well plate and incubated for 1 day. Then, cells were washed with PBS. Then, cells were fixed by crosslinking method with 4% of paraformaldehyde which forms covalent bonds between proteins in cells and their surroundings to preserve soluble proteins in PBS for 15 minutes. In the final step,

cells were washed with PBS for 3 times. To stain cells, they were perforate with 1% triton x-100 in PBS for 15 minutes for permeabilization of cell membrane to allow antibodies access into the intracelllular components in the beginning. Then, cells were washed with PBS for 3 times. The incubation was done with 1 % of Bovine Serum Albumin Buffer (BSA) in PBS for 30 minutes because this medium is used to maximize fluorescence signal intensities before staining cells without presence of free biotin In the last step, cells were stained with Alexafluor 488 by diluting dye 300X with 0.1 % of BSA in PBS. Then incubation step was performed for 1 h. To stain cells with Draq5, Alexafluor 488 dye was removed and dilutes the Draq5 dye 400X with 0.1 %BSA in PBS. The cells with Draq5 dye was incubated for 20 minutes. In the final step, Draq5 was replaced with PBS. Keep cells in +4 until imaging. All incubation steps were performed under dark condition to inhibit the quenching of fluorescent dye/proteins.

2.2.7.2 Osteogenic Activity

Osteogenic activity of Saos-2 cells seeded on scaffolds was investigated with alkaline phosphatase (ALP) activity of seeded cells (Pazarçeviren et al., 2020). Cells seeded on TCPS and cultivated with growth media were used as negative control whereas cells seeded on TCPS and cultivated with osteogenic media were used as positive control. Wells and scaffolds without cells were used as blanks. Scaffolds were sterilized as aforesaid. Scaffolds of 1 cm in diameter were seeded with cells at a density of 4×10^4 cells/cm^2. Samples were cultivated in osteogenic media for 14 days. ALP activity, amount of DNA and total intracellular protein of cells were determined at days 7 and 14. For this purpose control wells and scaffolds were washed with PBS. Following, 300 µl of lysis buffer consisting of 0.1 % ($^{w}/_{v}$) Triton X-100 in carbonate buffer at pH 10.5 was added to each well and cells were lysed with a freezing at -80°C and thawing at 37ºC. Obtained lysates were centrifuged at 10000 rpm for 10 minutes and cell lysate was used for analyses. Amount of DNA was measured by using PicoGreen™ dye. For this purpose, 1% ($^{v}/_{v}$) picogreen solution was prepared in Trishydroxyamino methane (TRIS)/EDTA buffer with pH 7.5. 50 µl of the cell lysate was mixed with 50 µl of picogreen solution in black 96-well plate. Fluorescence was read at 485 nm

excitation and 538 nm emission wavelengths. Calf thymus DNA was used for constructing the calibration of DNA (100, 200, 300, 400, 500, and 600 ng/ml).

ALP activity was measured by using para-nitrophenylphosphate (pNPP) as substrate. First, 1 part of 100 mM $MgCl_2$ solution was mixed with 50 part of pNPP. Obtained mixture was diluted 3 times with distilled water to yield pNPP working solution. Following, 50 µL of cell lysate was mixed with 100 µL of pNPP working solution and incubated at 37°C for 1 hour. Finally, absorbance was recorded at 405 nm. Different concentration of p-nitrophenol (50,100, 150, 200, 250, 300 µM) was used for constructing the calibration curve. Specific ALP activity was expressed as (nmol/mg protein/min). Protein amount was determined by bicinchonic acid (BCA) assay. For this purpose, 4% (w/v) $CuSO_4$ solution was prepared in distilled water. Then, 1 part of cupric sulfate solution was mixed with 50 parts of bicinchonic acid. 350 µL of this mix was added to 50 µL of cell lysate and incubated at 37°C for 1 hour. After incubation, absorbance was measured at 562 nm. Bovine serum albumin was used as standard for constructing the calibration curve to quantify the specific enzyme activity of cell (nmol/mg protein/min).

2.2.8 Statistical Analysis

Significant differences between groups were assessed by using Tukey's Comparison Test (SPSS-22 Software, SPPS Inc., USA). The differences were acceptable statistically at $p<0.05$. The results are shown with mean and standard deviation.

CHAPTER 3

RESULTS AND DISCUSSION

3.1 Characterization Results of Synthesized Materials: Zn-dıoped Hydroxyapatite and Boron Nitride nanofiber

3.1.1 X-Ray Diffraction Analysis

X-ray diffraction data are used to get information about average size and interlayer spacing d_{002}.The interlayer spacing of d_{002} is calculated from Bragg's law by using (002) diffraction angle (Bernard et al., 2002). The average size in BNNF for (002) and (100) planes were found to be 13 Å and 45 Å, respectively. Additionally, values of d_{002} and d_{100} were found to be 3.663 Å and 2.135 Å. The values of d_{002} in BNNF were slightly higher than that of BNNTs and hexagonal BN (3.33 Å), deducing a turbostratic BN phase of porous nanofibers (Lin et al., 2016). Besides, BNNFs include both amorphous and crystalline phases. (002) peaks are located at $2\theta \approx 24.3°$ (24.2° and 25.4°). The alignment of (002) layers is not orderly parallel to the axis of fiber (Luo et al., 2014). The relatively weak peaks at $2\theta = 42.95°$ and 50.25° correspond to (100) and (101) and indicate 2 dimensional order and 3 dimensional disorder BNNFs with hexagonal structure as seen in Figure 3.1 (Liu et al., 2018; Luo et al., 2014). The obtained XRD datas were similar to that of preperation of BNNF from polymeric precurser (Lin et al., 2016; Luo et al., 2014).

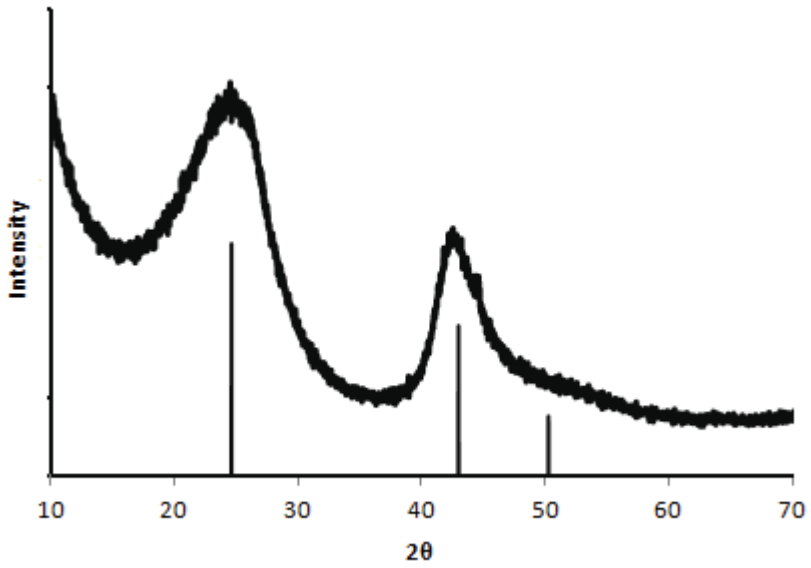

Figure 3.1 XRD analysis of BNNF with reference peaks of hexagonal BN

XRD spectrum of Zn HA and HA (Figure 3.2) revealed the characteristic diffraction peaks of pure HA in single hexagonal phase [JCPDS: 01- 089-6439]. Additionally, concentration of 1 wt% Zn (II) cation in the solid phase was too little to stimulate significant change in the cell parameters of HA. The crystallinity of HA and Zn HA was found as 75.5% and 76.9%, respectively. The XRD spectrum of HA was similar to the previous results reported (Mondal et al., 2017). Besides, Zn HA was found to belong to P63/m space group.

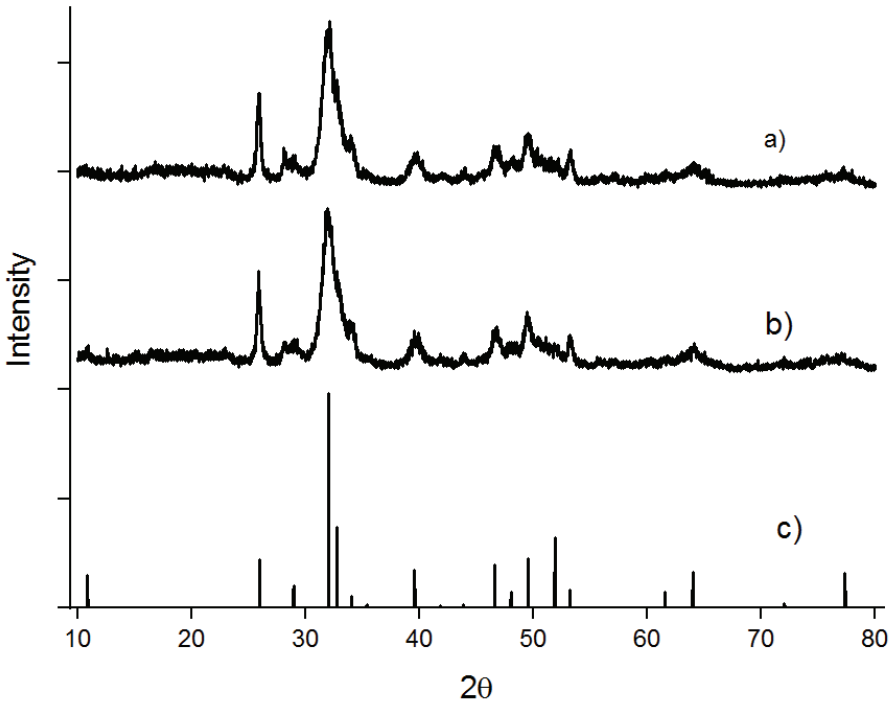

Figure 3.2 XRD analysis of a) Zn HA, b) HA, c) Card number with JCPDS: 01-089-6439 reference peaks of pure HA

3.1.2 Fourier-transform Infrared Spectroscopy Analysis

The bonds in synthesized BNNFs were confirmed by FTIR analysis (Figure 3.3). After the heat treatment at 1100°C, absorbtion peaks of BNNF were observed at ~794 and 1360 cm^{-1} which correspond to out-of-plane transverse optical (TO) modes of B-N-B bending and in-plane TO modes of B-N stretching, respectively. The presence of residual N-H bond was observed as absorption at 3500-3200 cm^{-1} (Geick et al., 1966; Qiu et al., 2009b; Yu & Matsumoto, 2003).

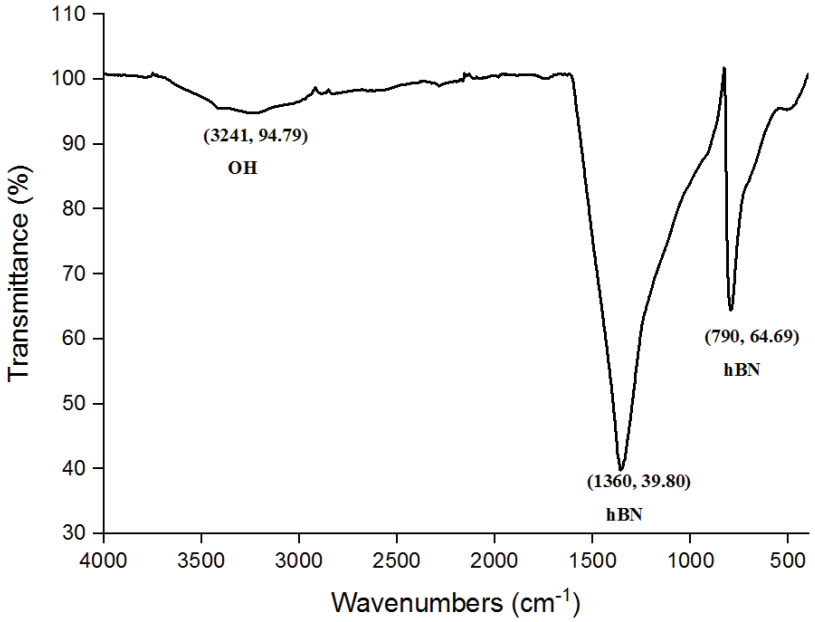

Figure 3.3 FTIR spectrum of BNNF

The absorption peaks of Zn HA and HA were observed at around 1090, 1025.07, 963.12, 600.30 and 561.12 cm^{-1} that are attributed to PO_4^{3-} groups as shown in Figure 3.4. The principal peaks at 1090 and 1025.07 cm^{-1} are associated with symmetric ν_3 bending-mode of PO_4^{3-} groups (Kashkarov et al., 2011; Mondal et al., 2017; Prabakaran et al., 2005). The broad band between 1000-1100 cm^{-1} is related to P-O bonding of phosphate group. The peaks around 963.12 cm^{-1} and in 561.12-600.30 cm^{-1} appeared was attributed to ν_1 streching mode of PO_4^{3-} and splitted ν_4 bending mode of PO_4^{3-} group, respectively (Kashkarov et al., 2011; Mondal et al., 2017; Prabakaran et al., 2005). Additionally, stretching mode of hydroxyl group (OH^-) is assigned at 3345.15 cm^{-1} while liberation bands of OH bands are generally found at 632 cm^{-1}. This is because of that liberation band intensity of OH in the Zn HA decreases as the amount of Zn doping increases. This also suggests the Zn is inserted in the channel of OH in this structure (Bhattacharjee et al., 2019; Tank et al., 2011). In a study, the band of Zn-O stretching was detected in the 433 cm^{-1} (Uysal et al., 2013) but this region corresponds to fingerprint so it is difficult to identify the specific peak of Zn. XPS can be used to detect the zinc ions. Additionally, the broad band at 1645.59 cm^{-1}

indicates the absorption of water. The weak band at 1423.22 cm^{-1} also shows the presence of trace CO_3^{2-} because of the reaction of carbon dioxide in air and Ca^{2+} and Zn^{2+} in the surface layer of the HA structure (Fowler, 1974; Stanić et al., 2010; Tank et al., 2014; Türk et al., 2019).

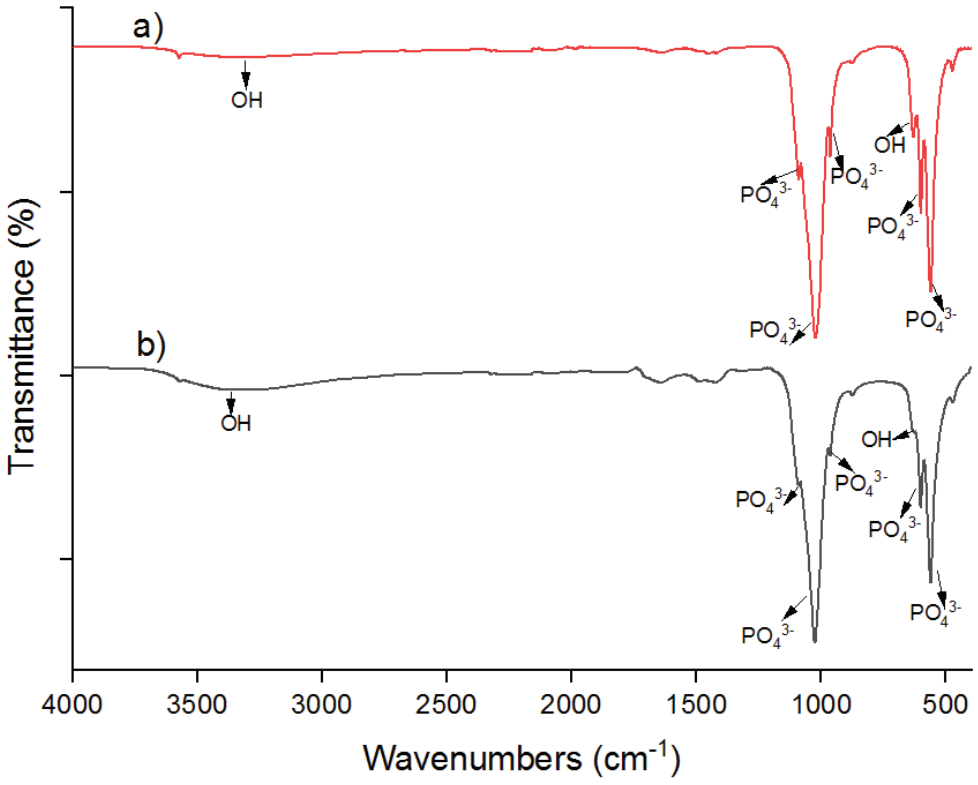

Figure 3.4 FTIR spectrum of a) HA and b) Zn HA

3.1.3 X-Ray Photoelectron Spectroscopy Scanning Analysis of Boron Nitride Nanofiber

The chemical state of BNNF was analyzed with XPS. The results showed that surface of the BNNFs included boron (B), carbon (C), nitrogen (N) and oxygen (O) with binding energies of B1s, N1s, O1s and C1s and total XPS spectrum in Figure 3.5, respectively. Also, the binding energy was calibrated to the C1s energy (284.8 eV) as a reference. In this thesis, the B1s spectrum is defined as B-N peak in between 190 eV-191 eV which corresponds to binding energy of B and

N. The full spectrum showed that BNNFs consist of mainly B and N elements with small amount of C and O elements (Table 3.1) could be due to the impurities or CO_2 adsorption in the sample. Additionally, the atomic ratio of B:N was slightly higher than 1, which showed that BN was found in higher amount in the sample. These results were correlated with previous results and it also showed that BNNFs were synthesized successfully (Liu et al., 2019; Qu et al., 2018).

Table 3.1 Atomic ratios of B, N, C and O in BNNF

Element	B	C	N	O
Atomic Ratio (%)	41.53 ± 0.41	3.82 ± 0.17	22.61 ± 0.71	32.04 ± 1.04

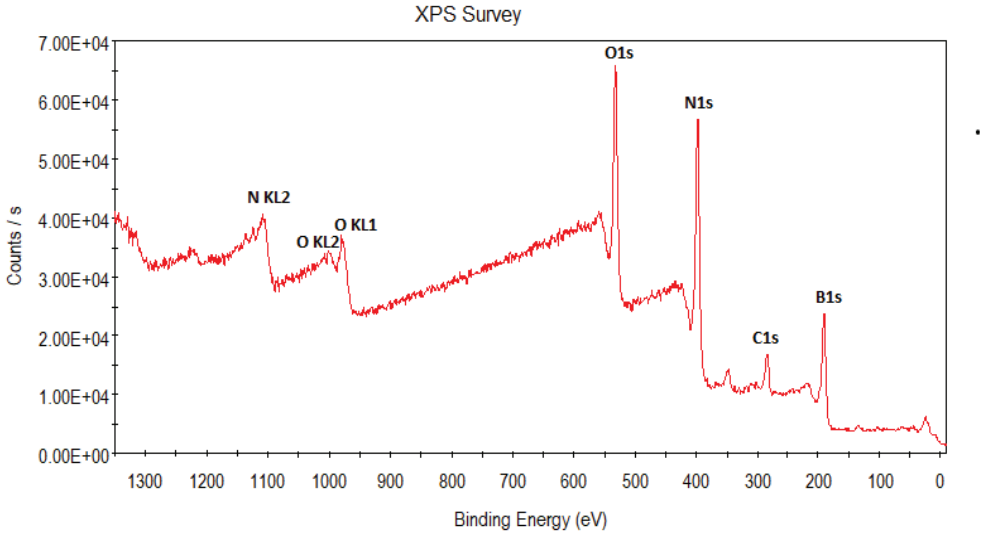

Figure 3.5 XPS full spectrum of BNNF sample

Additionally, the chemical state of Zn HA was analyzed with the XPS (Figure 3.6) and also atomic ratio of each element is shown in Table 3.3. Based on XPS the Ca/P ratio in the %1 Zn HA in Table 3.2, Ca/P ratio is slightly less then 1.67 in

the hydroxyapatite. This showed that the structure is calcium deficient structure. In the spectra, calcium (Ca2p), oxygen (O1s), phosphorus (P2p), and Zinc (Zn2P) peaks were observed. This result verified the presence of zinc ions in the apatite structure. The results were also consistent with literature reports (Ofudje et al., 2019; Thian et al., 2013; Wang et al., 2010; Popa et al., 2016).

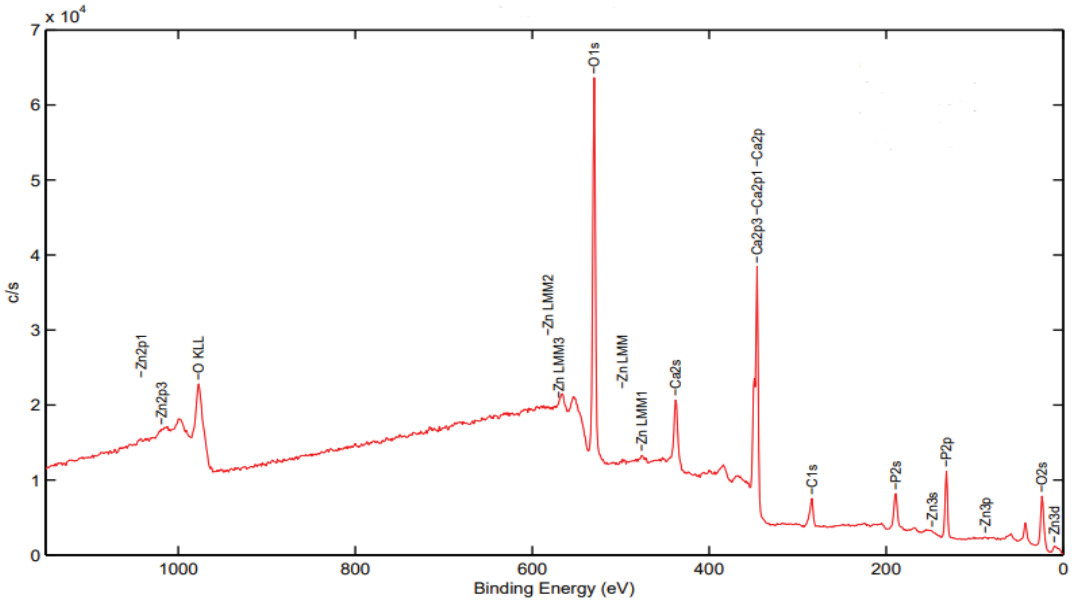

Figure 3.6 XPS full spectrum of Zn HA sample

Table 3.2 Ca/P ratio in the Zn HA

Element	Ca/P	Zn (%)
XPS	1.53	0.50

Table 3.3 Atomic ratios of Ca, P, Zn, C and O in Zn HA

Atom	**Atomic Ratio (%)**
Ca2p	17.4
P2p	11.7
O1s	57.6
C1s	12.9
Zn2p3	0.5

3.1.4 SEM Images of Boron Nitride Nanofiber and Zn-doped Hydroxyapatite

The morphology of BNNF was visualized by SEM as shown in Figure 3.7. The distribution of diameter was also measured from SEM images through using ImageJ software (USA) (Table 3.1). The obtained product after the heat treatment at 1100°C showed 1D BN fibers with high purity. The length and diameter of each fiber varied from several to tens of micrometers. SEM analysis of Zn HA showed the formation of nearly spherical Zn HA nanoparticles (Figure 3.8).

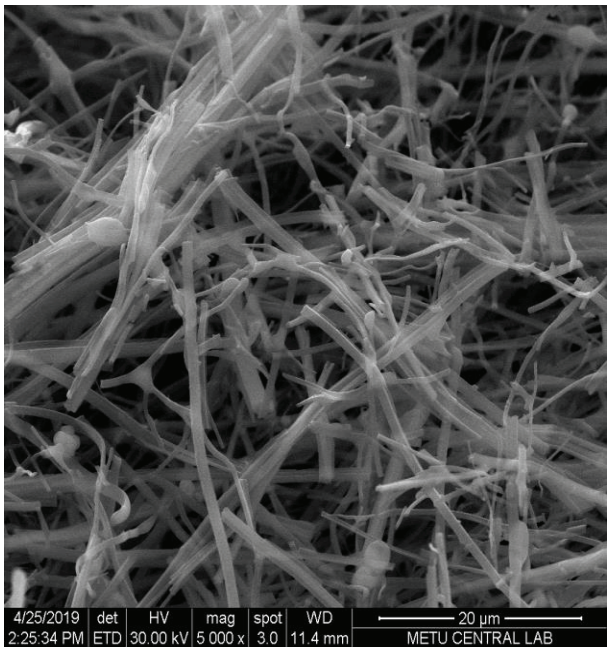

Figure 3.7 SEM image of BNNF with scale bar of 20 µm. Fiber morphology was observed after freeze drying.

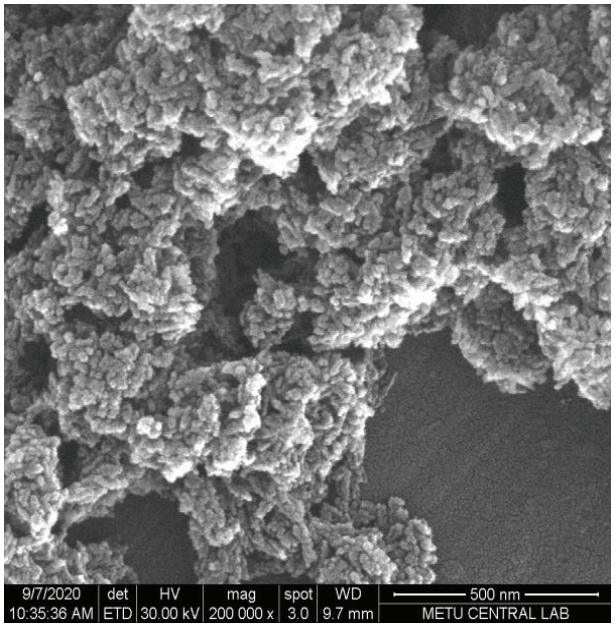

Figure 3.8 SEM image of nano Zn HA synthesized by the wet-precipitation method. Scale bar: 500 nm.

3.1.5 Boron Nitride Nanofiber & Zn-doped Hydroxyapatite Particle Size Analysis (MasterSizer)

Particle size of BNNF and Zn HA determined by using MasterSizer and ImageJ from SEM images are given in Table 3.4. However, there was a difference in the particle size determined by SEM (Scale bar: 500 nm) and mastersizer for BNNF due to the fact that mastersizer gives average hydrodynamic radius.

Table 3.4 Mean particle size (d[0.5]), surface weighted particle size (D[3,2]) and Span of Zn HA and BNNF from Mastersizer (n=3), mean particle size from SEM images (n=200).

Group	d [0.5] (µm)	D [3,2] (µm)	Specific Surface Area (m^2/g)	Span	SEM (µm)
Zn HA	9.31 ± 0.62	6.00 ± 0.12	0.99 ± 0.02*	4.17	-
BNNF	8.66 ± 0.51	5.76 ± 0.30	1.06 ± 0.02	3.29	0.59 ± 0.19

*stands for significantly the lowest group (n=3, $p<0.05$).

It was found that the specific surface area of Zn HA particles was significantly lower than that of BNNF whereas SPAN of Zn Ha group was significantly higher than that of BNNF group. There was no significant difference between the mean d [0.5] and D [3,2] of the groups. SPAN shows how far the 10 % and 90 % points are apart from each other normalized with the midpoint. A small value of SPAN indicates a narrow size distribution. In particle size determination, mean value is an important parameter to define the number, volume and surface distribution. In general, surface area moment mean results D [3,2] is named as surface area moment mean (Sauter mean diameter). It is generally used when the system has different sizes of particles without considering their physical meaning. The Sauter mean diameter of collected spherical particles with different sizes is equal to the diameter of equisized spherical objects composing a collection in the

polydispersed system. The Sauter mean diameter of objects gives an idea about the size of identical spherical objects by assuming same total area and volume (Kowalczuk & Drzymala, 2016). Thus, the value of D [3, 2] gave more reliable results because of different size shape of particles than that of D [4, 3] which is very sensitive to the presence of large particles rather than small particles. From data, D [3, 2] values of Zn HA and BNNFs were 6.00±0.12 µm and 5.76±0.30 µm, respectively. Average diameter of 200 BNNFs was obtained as 0.5998±0.188 µm by using software ImageJ (USA). However, there are differences between the size of BNNFs with the SEM and Mastersizer methods due to 1D structure of BNNFs. Mastersizer technique is generally used for spherical particles but to determine the 1D structure, ImageJ can be used to obtain reliable results for the BNNF structure.

3.1.6 Characterization of Zn-doped Hydroxyapatite with Inductively Coupled Plasma - Optical Emission Spectrometry (ICP-OES)

Inductively Coupled Plasma - Optical Emission Spectrometry (ICP-OES) and XPS was used to evaluate the amounts of elements in the structure of Zn substituted HA (Yedekci et al., 2020; Ofudje et al., 2019; Popa et al., 2016; Predoi et al., 2019) and it gives the results of elemental analysis of the Zn doped hydroxyapatite. ICP-OES showed the presence of Zn elements in the structure in Table 3.5. The obtained Zn is slighltly smaller than the previous results (Predoi et al., 2019).

Table 3.5 Zn atomic ratio in the Zn HA

Element	**Ca/P**	**Zn (%) (mol/mol)**
ICP-MS	-	0.33 ± 0.06

3.2 Characterization of Polycaprolactone Based Scaffolds

3.2.1 SEM Image of Fibers Through Rotary-Jet spinning

Morphology of fibers was analyzed by SEM (Quanta 400F Field Emission SEM, USA). Fibers PCL, PCL-Zn HA, PCL-Zn HA-BNNFs and PCL-BNNFs were produced with the rotary jet method. Besides, mean fiber diameter of 200 fibers was attained from the SEM images of fibers by using the software ImageJ (USA) (Table 3.3). Some agglomeration and bead formation on the PCL fibers were observed after the addition of the Zn HA and BNNF (Figure 3.9). This was because of the electrostatic interaction between particles which induce agglomeration, so good dispersion using sonication methods is needed for homogeneous size distribution. The morphology of fibers was uniform without any broken structure and aligned fibers were also observed. Additionally, SEM images of PCL-Zn HA-BNNF scaffolds that were prepared in cylindrical shape for compression tests are shown in Figure 3.10. The scaffolds had a cylindrical shape with a ∼4 mm diameter. In the SEM images, surface roughness and cylindirical shape of the scaffolds can be seen in Figure 3.10.

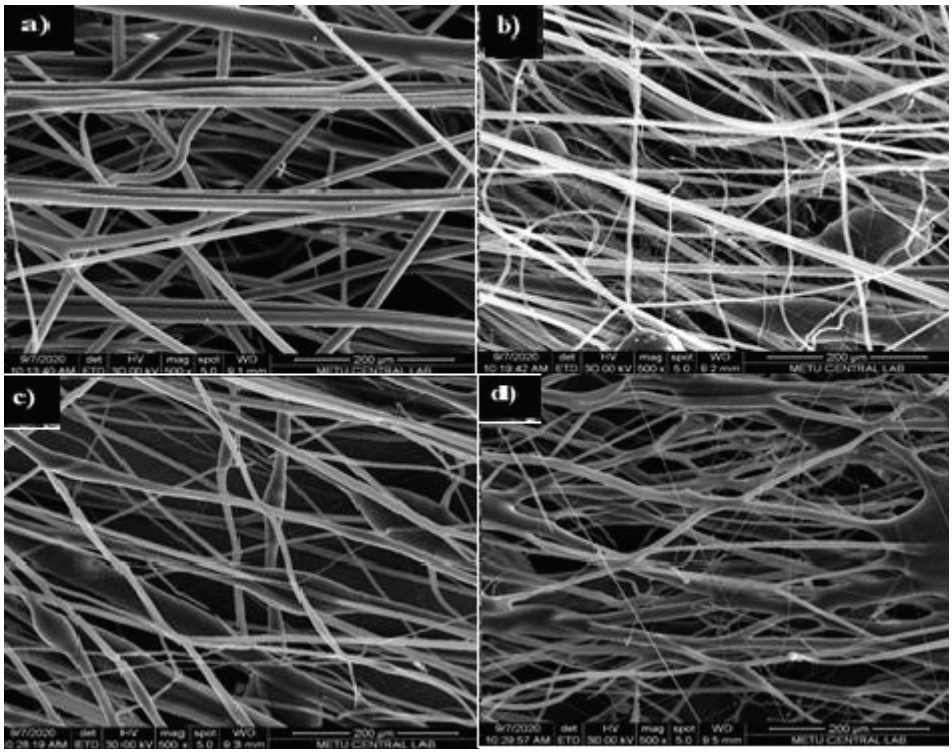

Figure 3.9 SEM images of a) PCL, b) PCL- Zn HA, c) PCL-Zn HA-BNNF, d) PCL-BNNF scaffolds (Scale bar: 200 μm).

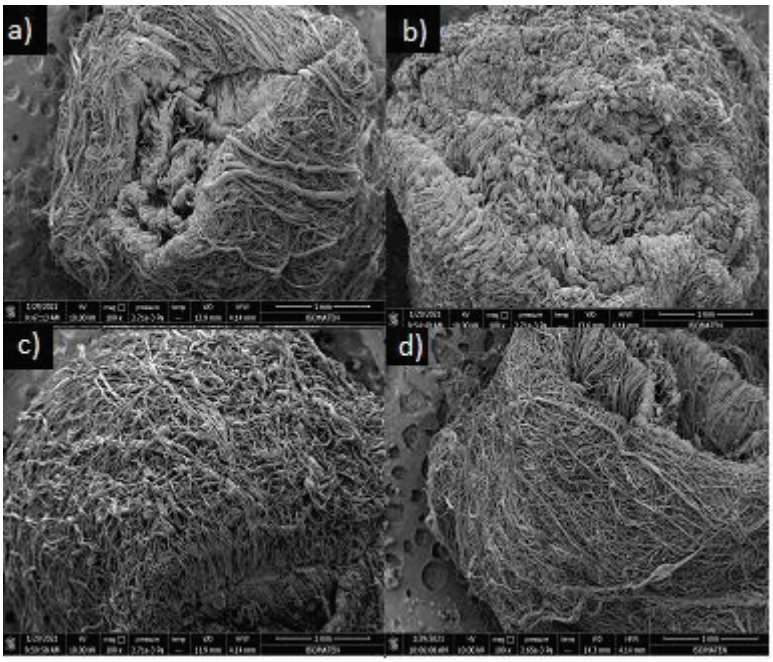

Figure 3.10 SEM images of the cylindirical shaped a) PCL, b) PCL- Zn HA, c) PCL-Zn HA-BNNF, d) PCL-BNNF scaffolds (Scale bar:1 mm).

3.2.2 Fiber Size Distribution of Polycaprolactone Based Scaffolds

The diameters of PCL fibers ranged from 6 µm to 13 µm (Table 3.6). They had smooth morphology and uniform diameter. Effect of Zn HA and BNNF addition to the fibers on the fiber diameter was investigated. The fiber diameter of 15% ($^{w}/_{w}$) PCL increased from 6.46 ± 1.66 µm to 11.16 ± 5.68 µm with the addition of 1% ($^{w}/_{w}$) Zn HA. Fibers produced using lower concentrations of PCL with Zn HA addition into had inhomogenous distribution of Zn HA in PCL fibers with less agglomeration (Hassan et al., 2014). Fiber diameter of PCL group was significantly lower than that of PCL-BNNF group. However, there was no significant difference between the mean fiber diameters of the other groups.

Table 3.6 Fiber diameter of PCL based scaffolds measured from SEM analysis by using ImageJ.

Group	Fiber Diameter (µm)
PCL	6.46 ± 1.66*
PCL-Zn HA	11.16 ± 5.68
PCL-Zn HA-BNNF	9.40 ± 3.72
PCL-BNNF	12.34 ± 4.05

* stands for significantly the lowest group (n=200, $p<0.05$).

After the addition of Zn HA, the morphology of fibers became irregular with protrusions because of particles agglomeration and electrostatic interaction. This interaction happened before and during the mixing of solution. However, the mixing solution was sonicated before spinning but it seems not to be enough for agglomeration. The nonhomegeneous dispersion of particles disturbs the alignment in the fibers and leads to an increase in the disorder while reducing the crystallinity (Bayrak et al., 2016). Zn HA particles were positioned on the surface of the fibers in the SEM images in Figure 3.9c. This led to an increment in the diameter of PCL fibers. Besides, the addition of BNNF resulted in the highest agglomeration in Figure 3.9d and this led to the highest fiber diameter increment (12.34 µm) compared to other composites in Table 3.6. PCL-BNNF-Zn HA

composite fibers had smaller diameter due to well dispersion of BNNF-Zn HA in the solution before spinning so less agglomeration was formed. Additionally, the obtained fibers were aligned and uniform without any broken fibers in Figure 3.9.

3.2.3 Mechanical Test of Polycaprolactone Based Scaffolds

Tensile test was performed on PCL, PCL-Zn HA, PCL-Zn HA-BNNF and PCL-BNNF fibers to test integration between PCL and Zn HA, BNNF layers as well as to assess adequacy of the scaffold for bone tissue engineering by testing in transverse direction. Young's Modulus and strain at break of each composite of PCL, PCL-Zn HA, PCL-Zn HA-BNNF and PCL-BNNF are given in Table 3.7. Image of a breaking of PCL, PCL-Zn HA, PCL-Zn HA-BNNF, PCL-BNNF scaffolds after the tensile test are given in Figure 3.11. The obtained Young's Modulus of PCL (34.66±9.61 MPa) produced with the rotary jet was very close to the previous reported data (Anindyajati et al., 2015; Guner et al., 2020; Lobo et al., 2018). On the other hand, Young's moduli of PCL-Zn HA (7.64 ± 1.13 MPa) and PCL-BNNF (5.14 ± 1.18 MPa) were lower than that of PCL-Zn HA-BNNF scaffolds (10.73 ± 0.91 MPa). In the previous studies, Wutticharoenmongkol et al. (2006) found a maximum tensile strength of 3.95 MPa PCL containing 1 wt% HA. Ozbek et al., 2017 obtained 5.60 MPa of Young's Modulus for poly(ε-caprolactone)/tri-calcium phosphate/hexagonal boron nitride electrospun composite which was lower than found in this thesis (10.73 MPa). This can be explained by the presence of agglomeration of Zn HA or BNNF particles in the scaffold of PCL-Zn HA and PCL-BNNF that leads to increasing disorder while decreasing the mechanical properties because of the constraint of interfacial area. In this respect, good dispersion of particles on fibers is very crucial to overcome the electrostatic and attractive forces between particles (Ashraf et al., 2018). Agglomeration of particles also creates defects and stress in the composites that ruin the mechanical properties of composites. Additionally, agglomeration reduces the effective volume fraction of particles in the polymer nanocomposite. Thus, bigger nanofillers including nanotubes, graphene and nanoclays can be used to reduce agglomeration of particles (Zare, 2016). Among composites, PCL-

BNNF had more beads and agglomeration so it had the lowest Young's modulus and tensile strength but PCL-Zn HA-BNNF had less agglomeration and beads with better dispersion on the fiber structure so it had better mechanical properties than that of PCL-BNNF and PCL-Zn HA. Additionally, the improvement of the mechanical properties of PCL-Zn HA-BNNF was dependent on the strength of bonding in the reinforcement-matrix interface. The bonding between Zn HA and BNNF is not ionic or covalent because they are chemically inert materials so there is a Van der Waal's bonding between Zn HA and BNNF at the interface. Besides, interfacial strength is also dependent on the lattice arrangement at the interface. If the mismatch at the lattice strain is minimum, work of adhesion becomes higher (Lahiri et al., 2011). These differences can be explained by the diameter of fibers, porosity and presence of impurities. Additionally, strain at break and tensile strength of the PCL-Zn HA-BNNF scaffolds were also higher compared to PCL-Zn HA and PCL-Zn HA-BNNF scaffolds.

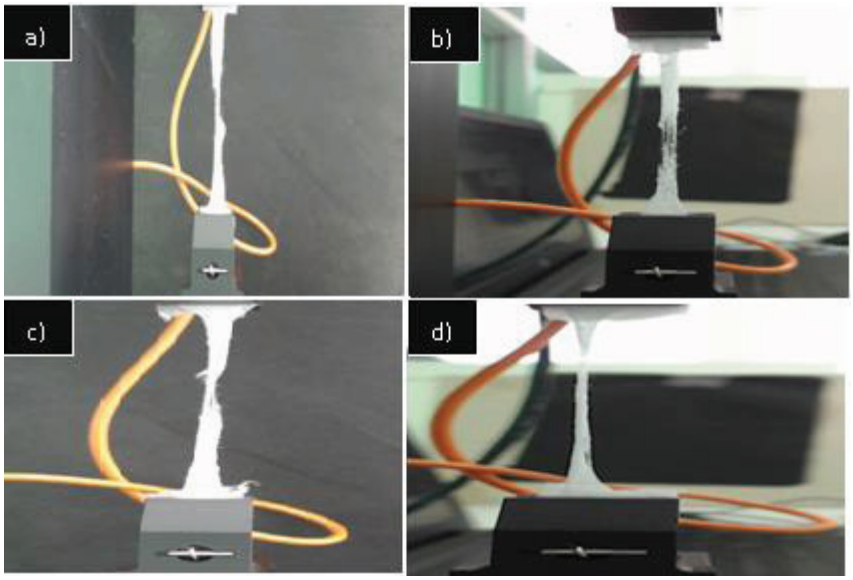

Figure 3.11 Tensile testing of the scaffolds: a) PCL, b) PCL-Zn HA, c) PCL-Zn HA-BNNF, d) PCL-BNNF.

Table 3.7 Young's modulus and strain of the scaffolds.

Group	Young's Modulus (MPa)	Strain at Break (%)
PCL	34.66 ± 9.61*	84.35 ± 2.85
PCL-Zn HA	7.65 ± 1.13	70.62 ± 2.65
PCL-Zn HA-BNNF	10.73 ± 0.91	85.07 ± 0.89
PCL-BNNF	5.14 ± 1.18	52.46 ± 1.85

"*"stands for significantly the highest group (n=3, $p<0.05$).

Young's modulus of PCL group was significantly the highest among the groups. There was no significant difference between Young's modulus of PCL-Zn HA, PCL-Zn HA-BNNF and PCL-BNNF groups. Additionally, there was no significant difference between the groups, in terms of strain at break. Additionally, Young's Modulus of PCL, PCL-Zn HA, PCL-Zn HA-BNNF and PCL-BNNF scaffolds was determined to evaluate the adequacy of their strength for bone tissue treatment. Human bone includes both cortical and cancellous bones. Most of the studies have focused on the cancellous bone. Thus, suitable architecture for artificial implants to mimic the shape of natural bone structure has been investivaged through sponge replica method with interconnected porous morphology. However, this structure led to weakened mechanical strength of scaffolds but cortical bone has higher mechanical strength and it was not studied too much because of its complex structure. In this mechanical work, we prepared cylindrical shape of PCL-Zn HA-BNNF with a diameter of ~ 4 mm to use them in non-load bearing applications including cartilage or skull. The Young's Modulus and compressive strength after compression test are given in Table 3.8. The structure of the all scaffold was designed with cylindrical shape by wrapping the bundle of PCL fibers around the very tiny stick with a ~4 mm diameter and then this stick was removed. The Young's Modulus and compressive strength (45% Strain) of PCL increased after the addition of BNNF and Zn HA. The compressive strength (2.53 MPa) of PCL-Zn HA-BNNF was very lower than to the previous reported data for composite of HAp-loaded PMMA-PCL (4.98 MPa) which had also cylindrical shape (Kim & Lee, 2011). In another study, Kurkijärvi et al.

(2004) found Young's and dynamic modulus of full-thickness, cartilage-bone cylinders of human (non-arthritic) knees. The obtained Young's modulus at equilibrium (E_{eq}) and the dynamic modulus (E_{dyn}) were 0.15 MPa-2.14 MPa and 0.8 MPa- 15.58 MPa. Thus, it was widely accepted but there can be small differences with the mechanical strength of natural bone. Besides, Paşcu et al. (2013) obtained Young's modulus (3.32 MPa) for PHBV electrospun matrix that was comparable with the low limit of load-bearing tissues including cartilage. The prepared scaffolds including PCL-Zn HA, PCL-Zn HA-BNNF and PCL-BNNF had comparable compressive mechanical strength with the previous results and BNNF addition improved the mechanical properties of PCL scaffolds. The highest compressive strength was obtained with PCL-Zn HA-BNNF due to less porosity because the addition of BNNF or Zn HA seperately into PCL resulted in more voluminous and porous structure. This makes their dispersion difficult and resulted in the inhomogeneous microstructure of material. As a result of this, compressive strength decreased. However, the addition of BNNF and Zn HA together in PCL enabled their good and homogeneous dispersion in the PCL rather than voluminous structure. Thus, PCL-Zn HA-BNNF structure with higher compressive strength was obtained (Grzeszczyk et al., 2020). Young's modulus of PCL group was significantly lower than that of PCL-Zn HA-BNNF groups. Additionally, there was no significant difference between the other groups. It can be concluded that PCL-Zn HA-BNNF scaffolds can be used for treatment of cartilage (12 MPa) or other nonloading application like skull due to their close mechanical strength (Lai et al., 2015).

Table 3.8 Young's moduli and compressive strength of PCL based scaffolds (n=3). *stands for significantly the lowest group.

Group	Young's Modulus (MPa)	Compressive Strength (MPa)
PCL	1.38 ± 0.59*	0.34 ± 0.26*
PCL-Zn HA	3.42 ± 0.10	0.87 ± 0.50
PCL-Zn HA-BNNF	5.54 ± 2.20	2.53 ± 3.61
PCL-BNNF	3.30 ± 0.54	1.05 ± 1.02

3.3 Bioactivity of Polycaprolactone Based Scaffolds

The bioactivity of PCL scaffolds was investigated after 1, 7 and 14 days incubation in SBF solution at 37°. The weight change was monitored (Figure 3.12). The highest weight change was observed in the of PCL-Zn HA-BNNF group, while PCL and PCL-BNNF groups had the two lowest weight change and less apatite formation because of their hydrophobic properties which prevented the wettability and water uptake (Hassan et al., 2014). Additionally, pH of SBF solution was observed for 1st, 7th and 14th day. There was no significant change in the pH of solution on day 1st day in all groups (Figure 3.13) and similar to the human body. As the immersion time increases, there was slight increment in pH. This can be because of the dissolution of the Ca^{2+} ions into the SBF solution in the early stage and then exchange of Ca^{2+} and H^{+} accumulates the OH^{-} ions on the surface of the composite which favors the accumulation of apatite layer. When OH^{-} and PO_4^{3-} ions attract the

H^+ and Ca^{2+} ions increase in the negative charge was observed on the surface of the scaffolds (Bovani et al., 2019). On day 7 pH increased from 7.40 to 7.63 and 7.58 in PCL-Zn HA-BNNF and PCL-Zn HA groups, respectively. This increment can be related with OH^- ions coming from Zn HA structure interacts with Ca^{2+} ions in the solutions. Addtionally, H^+ ions in the SBF solutions interact with the BNNF through the Lewis acid-base interaction which favors the apatite precipitation because accumulation of Ca^{2+} will be faster (Rahmati et. al, 2018) ions. This was verified by SEM images and weight change because the higher precipitation was observed in the PCL-Zn HA-BNNF and PCL-Zn HA groups (Figure 3.15c and 3.15b). Similarly, the highest pH was observed for PCL-Zn HA-BNNF and PCL-BNNF on the 14^{th} day. The presence of apatite layer was also examined by SEM (Figures 3.14, 3.15 and 3.16) for the 1^{st}, 7^{th} and 14^{th} day. At 1^{st} day, apatite layer was not noticable but at 7^{th} day, apatite layer formed and covered the surface of fibers like a sheet and filled the gaps between the fibers (Figure 3.15b and Figure 3.15c). On the 14^{th} day, CaP precipitation was higher and more visible in PCL-Zn HA, PCL-Zn HA-BNNF and PCL-BNNF groups (Figure 3.16b, Figure 3.16c and Figure 3.16d, respectively). The enhancement in the bioactivity of PCL scaffolds was due to both BNNF and Zn HA. In BNNF, there is a vacant p orbital of boron atom and this enables Lewis acid nature. Moreover, HA has Lewis base nature. The formation of HA crystals occured through the Lewis acid-base interaction. In the mechanism of apatite formation in SBF is initiated by firstly adsorption of Ca^{2+} by the negatively charged surface. Then, CaP precipitation was formed by recruitment of HPO_4^{2-} through the ionic interaction with Ca^{2+}. Hence, there is also OH^- ions in the structure of Zn HA. As OH^- ions are released into the solution environment, Ca^{2+} ions exchange increases in the SBF solution and induces formation of the apatite layer on the surface of fibers (Rahmati et al., 2018). This result highlighted the bioactivity of BNNFs for mineralization.

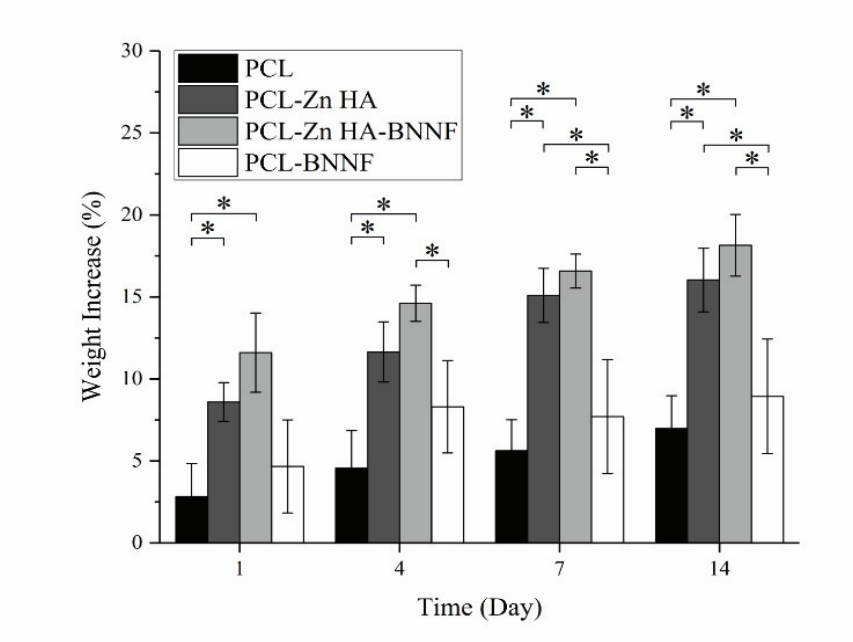

Figure 3.12 Weight change of PCL, PCL-Zn HA, PCL-Zn HA-BNNF and PCL-BNNF scaffolds in SBF at 37ºC. "*" indicates statistical significant difference between the groups (n=6, $p<0.05$).

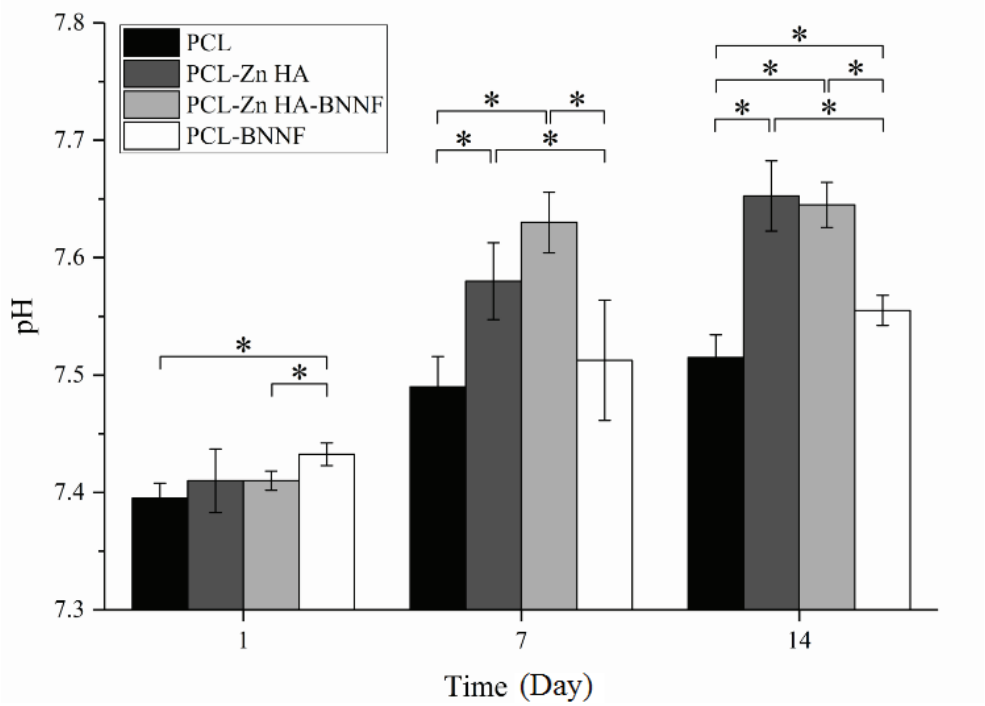

Figure 3.13 pH change of SBF in which PCL, PCL-Zn HA, PCL-Zn HA-BNNF and PCL-BNNF scaffolds were incubated at 37ºC. "*" indicates the statistical difference between the groups (n=4, $p<0.05$).

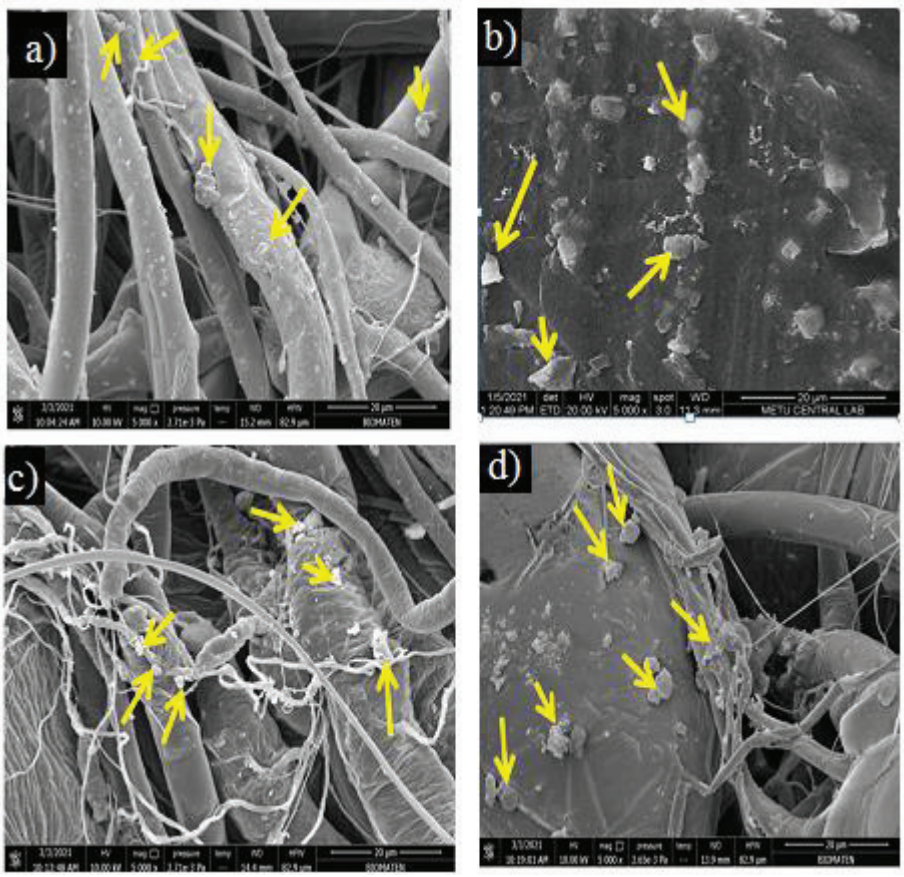

Figure 3.14 SEM images of scaffolds before and after 1st day of SBF immersion. a) PCL, b)PCL-Zn HA, c) PCL-Zn HA-BNNF, d) PCL-BNNF (Scale bar: 20 μm). (Yellow arrows: CaP deposition on the fibers)

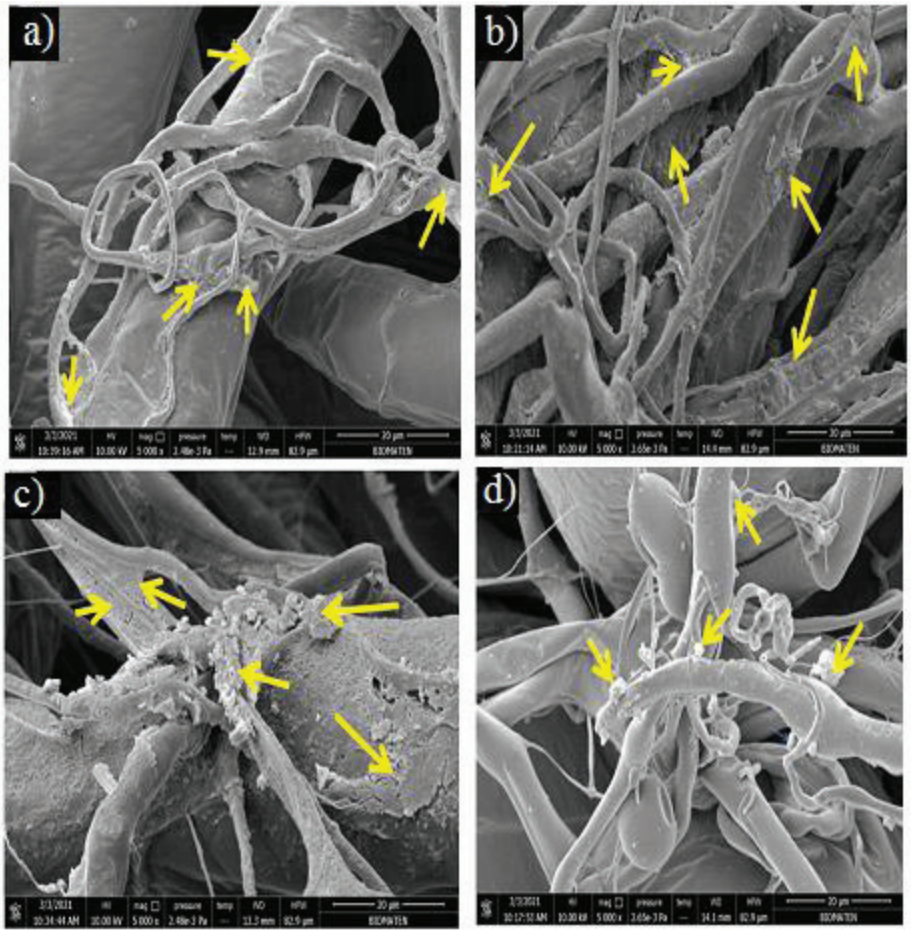

Figure 3.15 SEM images of scaffolds before and after 7th day of SBF immersion. a) PCL, b) PCL-Zn HA, c) PCL-Zn HA-BNNF, d) PCL-BNNF (Scale bar: 20 μm). (Yellow arrows: CaP deposition on the fibers)

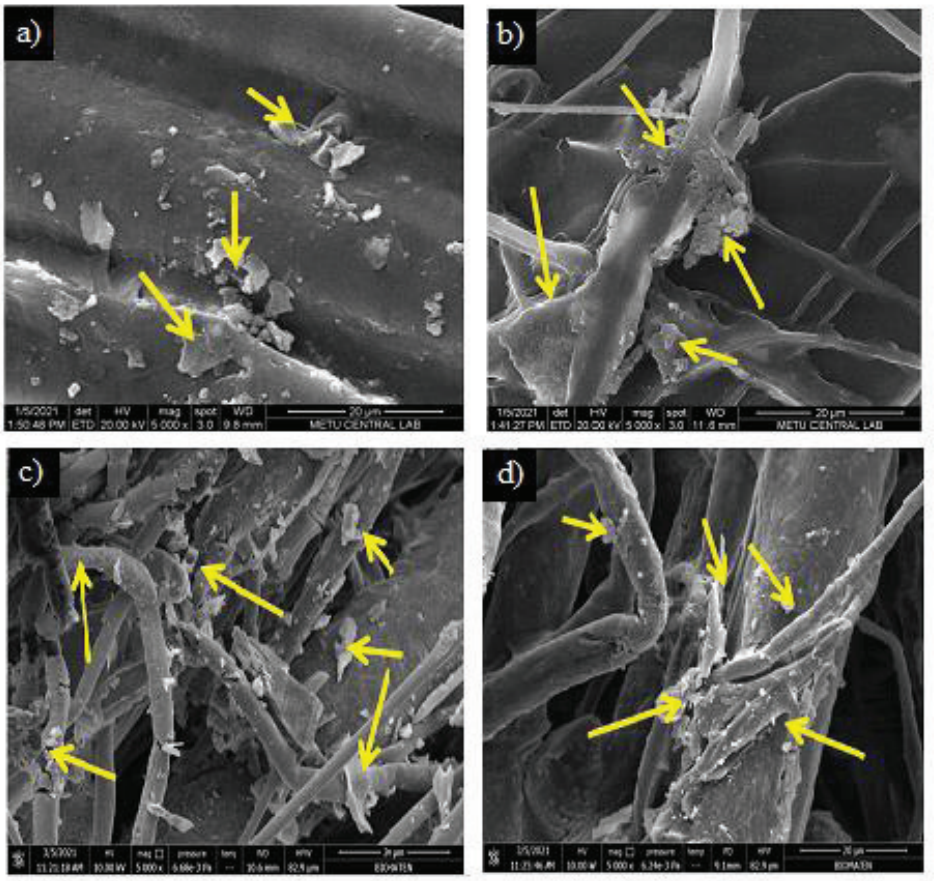

Figure 3.16 SEM analysis of PCL scaffolds after SBF immersion at 14th day a) PCL, b) PCL-Zn HA, c) PCL-Zn HA-BNNF, d) PCL-BNNF (Scale bar: 20 μm). (Yellow arrows: CaP deposition on the fibers).

CaP precipitation was also investigated with XRD analysis as seen in Figures 3.17-3.19. The characteristic peaks of HA are seen $30° < 2\theta < 33°$ (Sossa et al., 2018). In the 1st day, there was no peak between 30° and 33°. However, at the 7th and 14th days, the peaks in this range became more visible when compared to the 1st day. This showed the presence of CaP precipitation.

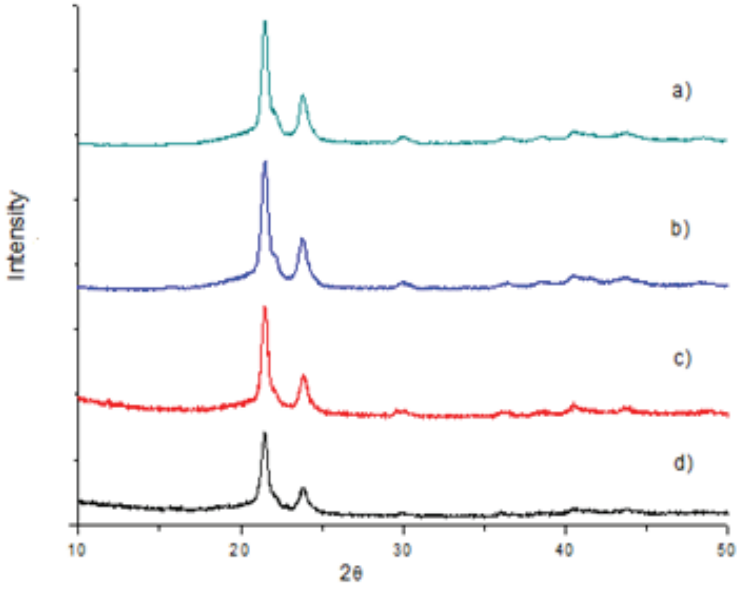

Figure 3.17 XRD analysis of PCL scaffolds after SBF immersion at 1st day: a) PCL-BNNF, b) PCL-Zn HA-BNNF, c) PCL-Zn HA, d) PCL

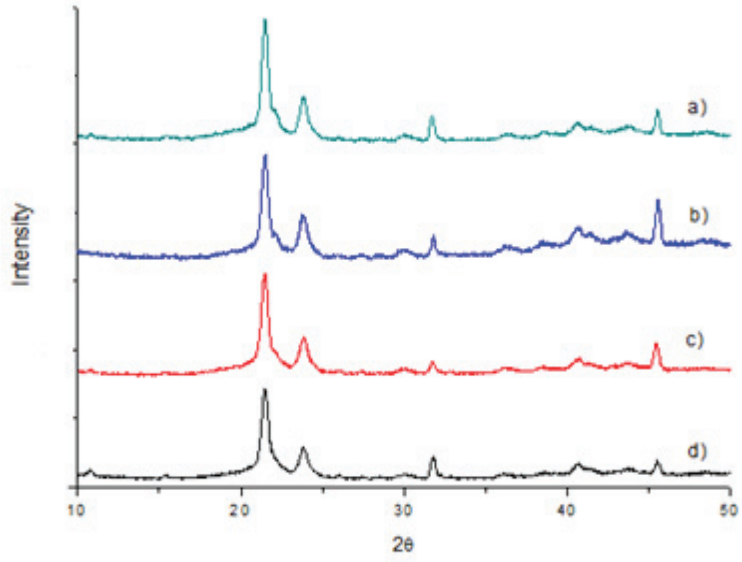

Figure 3.18 XRD analysis of PCL scaffolds after SBF immersion at 7th day: a) PCL-BNNF, b) PCL-Zn HA-BNNF, c) PCL-Zn HA, d) PCL

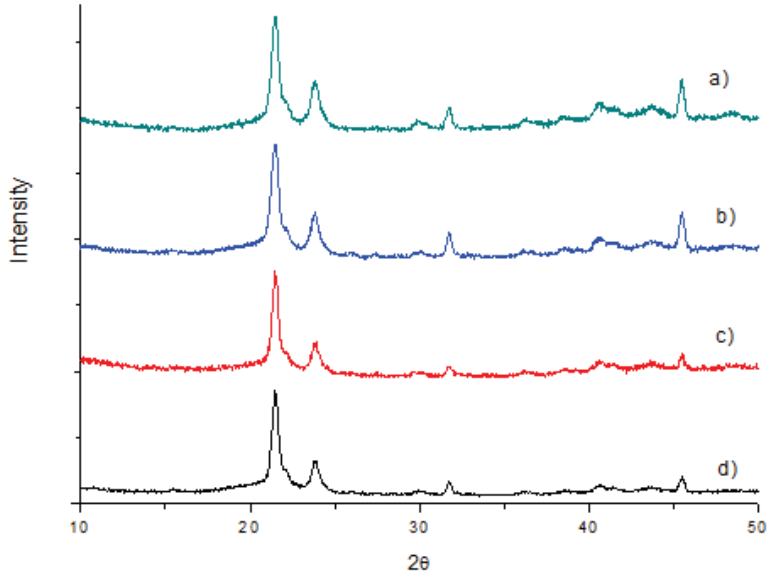

Figure 3.19 XRD analysis of PCL scaffolds after SBF immersion at 14th day: a) PCL-BNNF, b) PCL-Zn HA-BNNF, c) PCL-Zn HA, d) PCL

The formed CaP apatite layer was analyzed with the FTIR in the Figure 3.20-3.22. In all groups, carbonyl stretching peaks were dominated at 1722.38 cm^{-1} which corresponds to the vibrational mode of C-COO, C-C, CH_2 and C=O streching modes of PCL. The SBF-treated PCLcomposites had 1040.63 cm^{-1}, 1107.30 cm^{-1}, 960 cm^{-1}, 583 cm^{-1} and 452.80 cm^{-1} corresponding to the PO_4^{3-} main peaks showing the presence of calcium phosphate. The peaks around 1631.65 cm^{-1},1471.28 $cm^{-1}$and 1554.15 cm^{-1} corresponds to CO_3^{2-} peaks. The the peaks around 3188.04 cm^{-1} and 2944.39 cm^{-1} correspond to OH^-. These peaks verified the presence of CaP precipitation. The OH^- peaks are more apparent and distinct in the 7th and 14th days in the Figure 3.21 and Figure 3.22. Additionally, these results were compatible with the previous results (Berzina-Cimdina & Borodajenko, 2012; Deliormanlı et al., 2019).

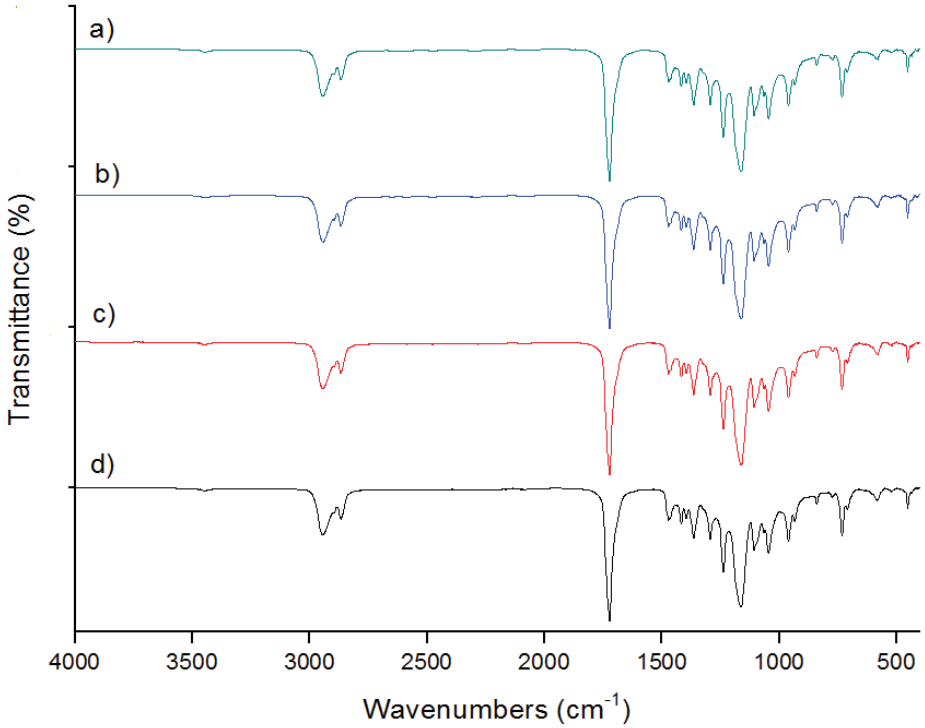

Figure 3.20 FTIR analysis of PCL scaffolds after SBF immersion at 1st day: a) PCL-BNNF, b) PCL-Zn HA-BNNF, c) PCL-Zn HA, d) PCL

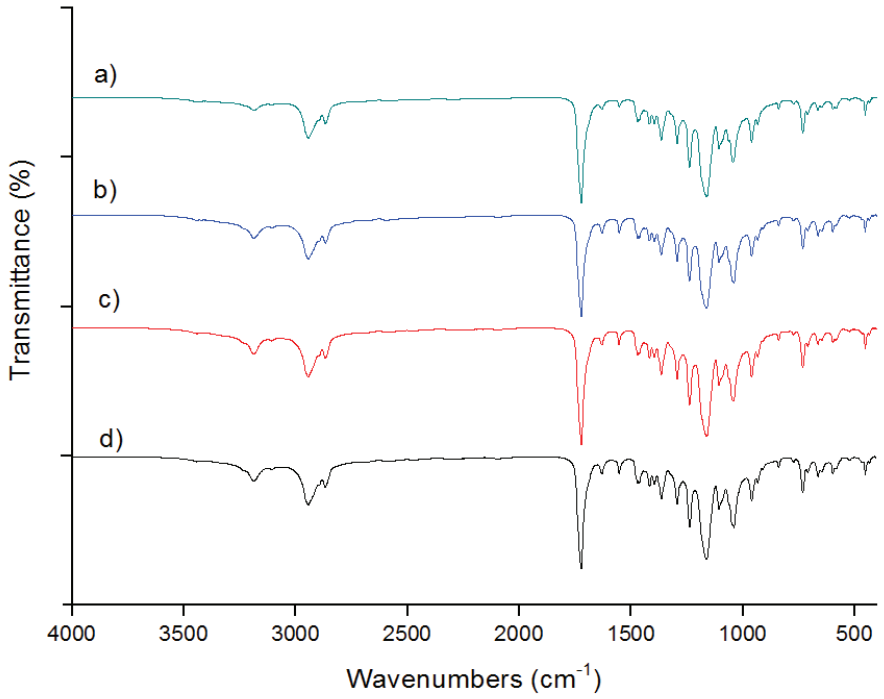

Figure 3.21 FTIR analysis of PCL scaffolds after SBF immersion at 7th day: a) PCL-BNNF, b) PCL-Zn HA-BNNF, c) PCL-Zn HA, d) PCL.

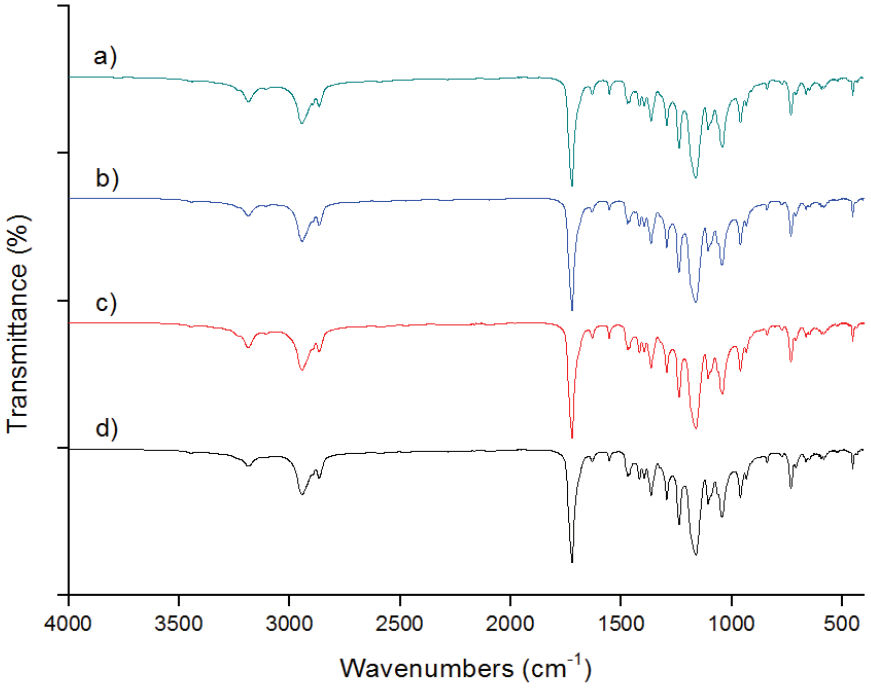

Figure 3.22 FTIR analysis of PCL scaffolds after SBF immersion at 14th day: a) PCL-BNNF, b) PCL-Zn HA-BNNF, c) PCL-Zn HA, d) PCL

3.4 Cell Culture Studies

3.4.1 Assessment of Cell Viability

The cell viability of Saos-2 cells in the presence of Zn HA of different concentrations was evaluated with indirect cytotoxicity test using MTT assay. The MTT (3-(4,5- dimethylthiazol-2-yl)-2,5-diphenyl-tetrazolium bromide) is used to analyze the metabolic activity of viable cells by measuring optical density of dark blue formazan crystal which is formed by reduction of the tetrazolium ring of MTT because reduction of MTT happen in the mitochondria by succinate dehydrogenase (Santos et al., 2007; Sonmez et al., 2016). No cytotoxic effect was observed for all concentrations upto 200 mg/ml Zn HA, however 500 mg/ml of Zn HA lowered cell viability compared to the control group (Figure 3.23) as also reported previously (Santos et al., 2007). Additionally, Ito et al., (2000) also reported that doping with Zn^{2+} with the amount in the range of 0.6-1.2 wt% significantly improved the proliferation of MC3T3-E1 cells compared to βTCP/HA composite (control group). Furthermore, Webster et al., (2001) found that doping HA with 2 mol% of Zn^{2+} significantly increased the adhesion of osteoblasts. In this thesis, the results of 1 wt% of Zn doped HA were in agreement with the previous results reported in the literature. We observed that that up to 500 mg/ml concentration of Zn HA could be used without showing any cytotoxic effect.

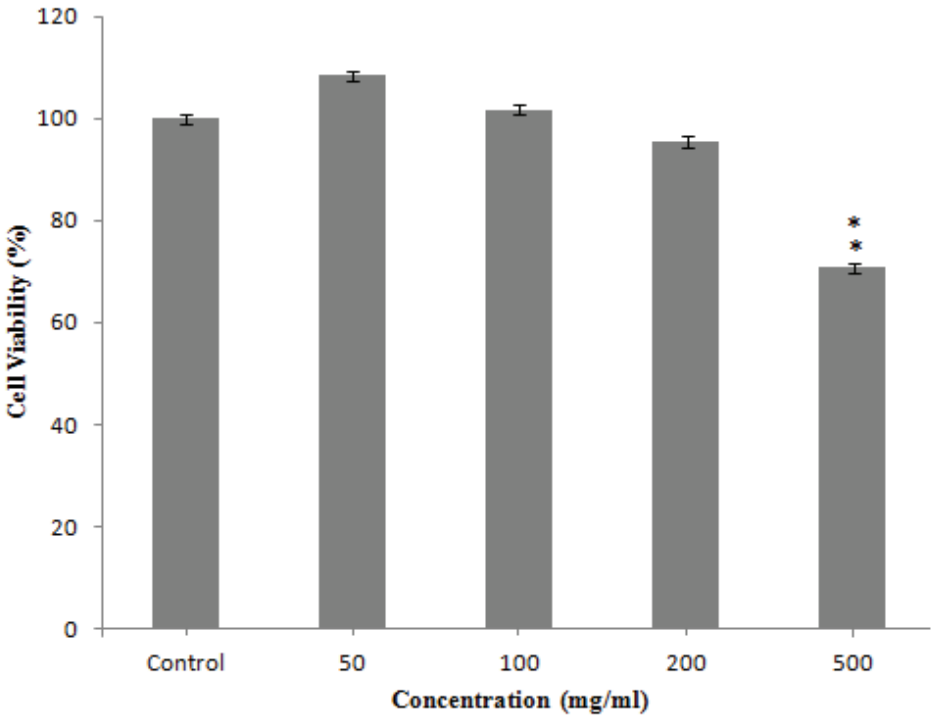

Figure 3.23 Dose dependent cytotoxicity test results of Zn HA using indirect elution method. Saos-2 cells were incubated with the extracts of Zn HA of different concentrations for 1 day. "**"shows the group which is significantly lower than the other groups (n=8, $p<0.05$).

Dose dependent cytotoxicity test of BNNF was also performed on Saos-2 cells using MTT assay. In our case, 1 and 2.5 mg/ml BNNF didn't show any significant cytotoxic effect to Saos-2 cells but 5 and 20 mg/ml of BNNF led to cytotoxicity to Saos-2 cells. Besides, the small amount of BN was used in the cell studies in general. This was explained by the morphology and size of the BN nanostructures because as the size and dimension of nanoparticles becomes smaller, they possess high surface energy which enables more unsaturated boron atoms on the surface. This leads to high reactivity in the cell and induce reactive oxygen species (ROS). Thus, toxicity was increased. Another reason could be due to transport of smaller nanoparticles into the cells through phagocytosis which could lead to generation of reactive oxygen species. The size and shape of BN nanostructures are very important for biocompatibility. In previous studies, biocompatibility of commercial BN nanosheet and BN nanoparticles was reported by using Saos-2

cell. In a study, it was observed that the viability of the Saos-2 cells was lower than 20% when they were incubated with spherical BN nanomaterials and BN nanosheets which were less than 100 nm in size. The reason of this cytotoxicity was explained by their higher surface area. BN nanomaterials are in nanometer size, the amount of boron and surface area increased by 30-fold and 6-fold, respectively. Thus, as boron amount was increased, the viability of Saos-2 cells significantly decreased. The boron content of cell culture was measured by elemental analysis to investigate the effect of concentration of BN nanostructure on the cytotoxicity. It was observed that the boron content varied significantly with concentration of material. Thus, BN was used at lower concentrations (0 to 100 μg mL^{-1}) for different cell lines (Merlo et al., 2018). In this thesis, it was observed that up to 2.5 mg/ml of BNNF can be used without showing any cytotoxic effect (Figure 3.24).

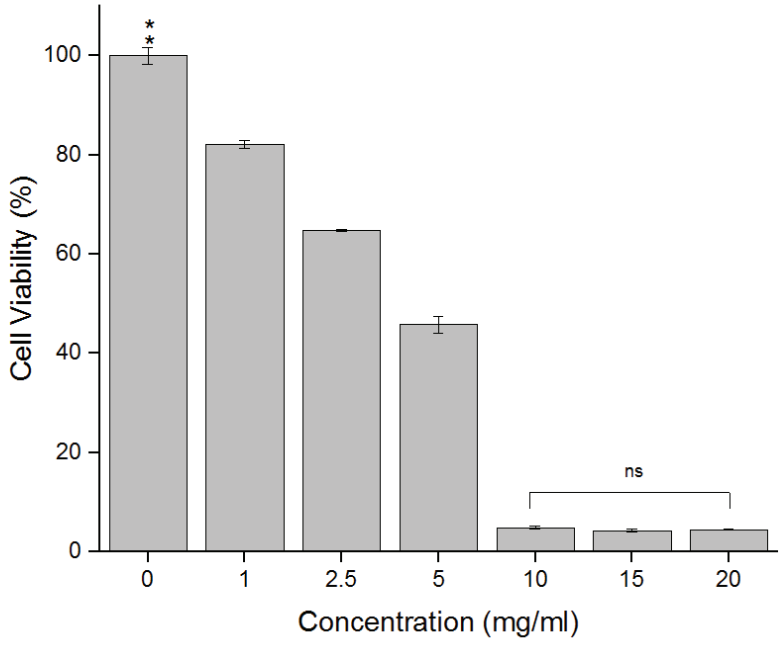

Figure 3.24 Dose dependent cytotoxicity test results of BNNF after 1 day of incubation at 37ºC. Saos-2 cells were incubated with the extracts of BNNF of different concentrations for 1 day. "**"shows the group which is significantly highest than the other groups (n=8, $p<0.05$).

3.4.2 Evaluation of Cytocompatibility and Cell Proliferation of Polycaprolactone Composite Scaffolds

Proliferation of Saos-2 on the scaffolds was studied using Alamar Blue assay. Alamar Blue assay is generally used to quantify viability and proliferation of cell lines by using oxidation and reduction of resazurin. This reduction is indicator of cell viability and metabolic activity in the cells (Bonnier et al., 2015). Higher cell viability was observed on PCL-Zn HA-BNNF scaffolds on day 7 with respect to the other groups (Figure 3.25). This result is similar to reported previous results. The presence of Zn HA in the PCL and apatite matrix enhanced the biocompatibility of BNNF (Horváth et al., 2011). This result is similar to the previous results reported. Lahiri et al. (2011) tested cytocompatibility of BNNT-HA composite scaffolds by *in vitro* culturing of osteoblasts for 1, 3 and 5 days. Higher number of viable cells was observed on BNNT -HA composite scaffolds by fluorescent microscopy.

Additionally, it was also repoted that the presence of Zn HA in the PCL and apatite matrix enhanced the biocompatibility of BNNF. They concluded that the presence of Zn and Ca ions induced cell proliferation (Horváth et al., 2011) There are studies in which HA was doped with zinc ions to obtain improved bioactivity (Sogo et al., 2004; Thian et al., 2013).

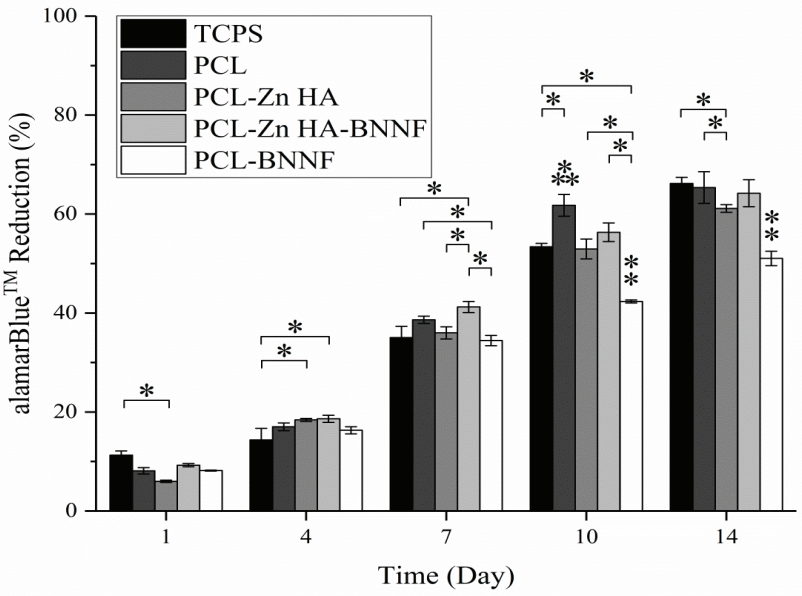

Figure 3.25 Percent reduction of Alamar Blue results of Saos-2 cells on PCL, PCL-Zn HA, PCL-Zn HA-BNNF and PCL-BNNF scaffolds and TCPS after 7 and 14 days of incubation. "**" refers that to the significantly lowest group, whereas "***" stands for significantly the highest group at a given time point. "*" indicates statistical significance between the groups (n=8, $p<0.05$).

3.4.3 Confocal Imaging

Confocal microscopy analysis was conducted to study the morphology and cell density on the scaffolds after different incubation periods (Figure 3.26, 3.27, 3.28). It used to resolve the detailed tissue structure in fixed cells by labeling with immunofluorescence to visualize in high resolution so sharp images were obtained with exact plane focus. Thus, it provides creation of sharp images. On the 1st day, the cell morphology was more spread, directed and started to extend along the fibers in the presence of PCL-ZnHA-BNNF (Figure 3.26c) while the morphology

of cells on the scaffold of PCL-Zn HA (Figure 3.26b) has less extension. The morphology of cells on PCL-BNNF (Figure 3.26d) scaffolds was round with less attachment. On the 7th day, the cells were extended more along the fibers and there was regional cell confluency in PCL-Zn HA-BNNF group compared to the other groups (Figure 3.27c). Saos-2 cells started to spread more in the PCL-BNNF group and cells became more directed along the fibers. BNNFs have a natural affinity towards proteins due to its surface which aid osteoblast proliferation and spreading (Merlo et al., 2018). The cell spreading has great importance for the interaction of cells with each other through the extracellular matrix (ECM) for cell migration and proliferation on the fibers resulted in development of multicellular organism and then tissue. On day 14, there was no significant difference in the cell viability between the groups except PCL-BNNF group (Figure 3.28). Regional confluency was observed in all groups. However, higher cell density was observed in PCL-Zn HA-BNNF and PCL groups compared to PCL-Zn HA and PCL-BNNF groups (Figure 3.28c and Figure 3.28a) , which was also in agreement with cell viability results (Figure 3.25). It can be concluded that presence of Zn HA and BNNF had synergistic effect to cell attachment, proliferation and spreading without causing cytotoxic effect on cells, as observed in the SEM and confocal images. Alamar results also support the confocal results because there was not significant difference between cell viability results of all groups at days 7 and 14, except for PCL-BNNF group. Ozbek et al. (2017) similary showed that poly(ε-caprolactone)/tri-calcium phosphate/h-BN scaffold provided higher attachment and proliferation of Saos-2 cells compared to pure hBN and TCP powders. The biocompatibility of pure h-BN and TCP powders was improved when incoporated in the PCL scaffolds. Cells made contacts with the adjacent fibers by their filopodia. Cell bridges between fibers were observed in all of the scaffolds at 14th day. Besides, PCL fibers with a diameter of 6 µm-13µm and its well aligned structure increase the the cell number by forming an environment for cell migration and proliferation.

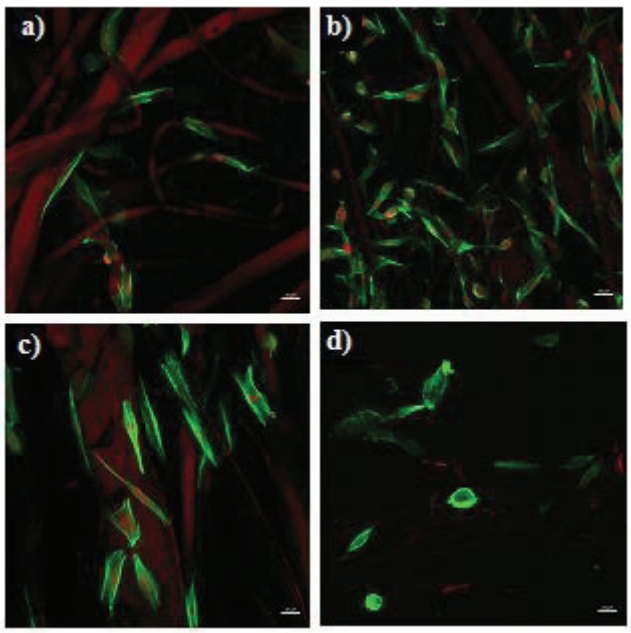

Figure 3.26 Confocal microscopy analysis of Saos-2 cells on PCL scaffolds at the end of 1st day: a) PCL, b) PCL-Zn HA, c) PCL-Zn HA-BNNF, d) PCL-BNNF (Scale bar: 20 μm) (red: nuclei, green: cytoskeleton).

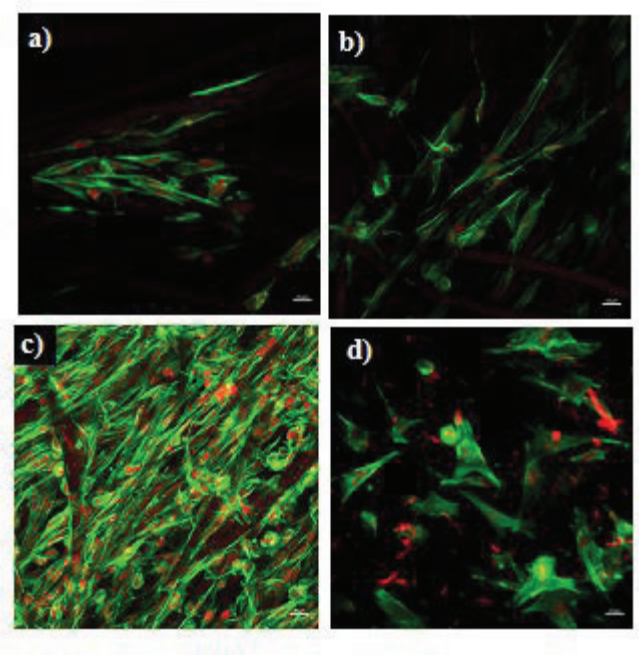

Figure 3.27 Confocal microscopy analysis of Saos-2 cells on PCL scaffolds at the end of 7th day: a) PCL, b) PCL-Zn HA, c)PCL-Zn HA-BNNF, d) PCL-BNNF (Scale bar: 20 μm) (red: nuclei, green: cytoskeleton).

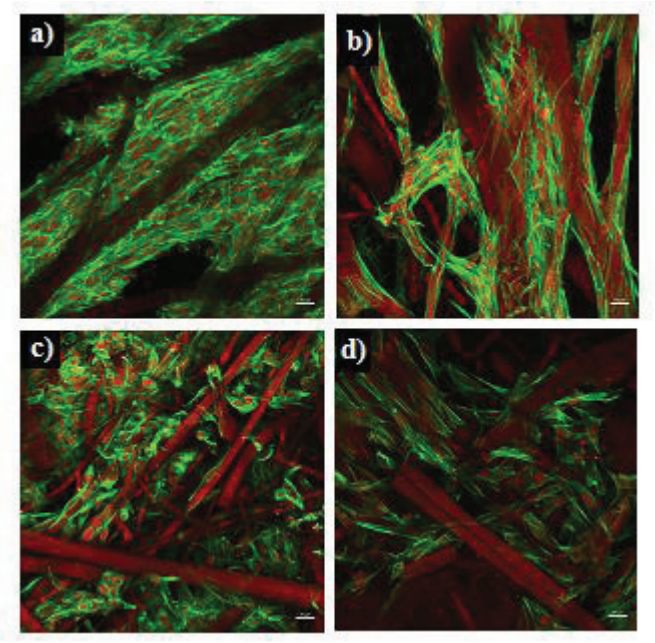

Figure 3.28 Confocal microscopy analysis of Saos-2 cells on PCL scaffolds at the end of 14th day: a) PCL, b) PCL-Zn HA, c) PCL-Zn HA-BNNF, d) PCL-BNNF (Scale bar: 20 μm) (red: nuclei, green: cytoskeleton).

Additionally, attached and spread of Saos-2 cells were observed on PCL scaffolds by SEM image (Figure 3.29-3.31) at the day of 1, 7 and 14. In the PCL-Zn HA-BNNF group, colonization of the cells were observed and their filopodia extension to move between fibers (Figure 3.31c).

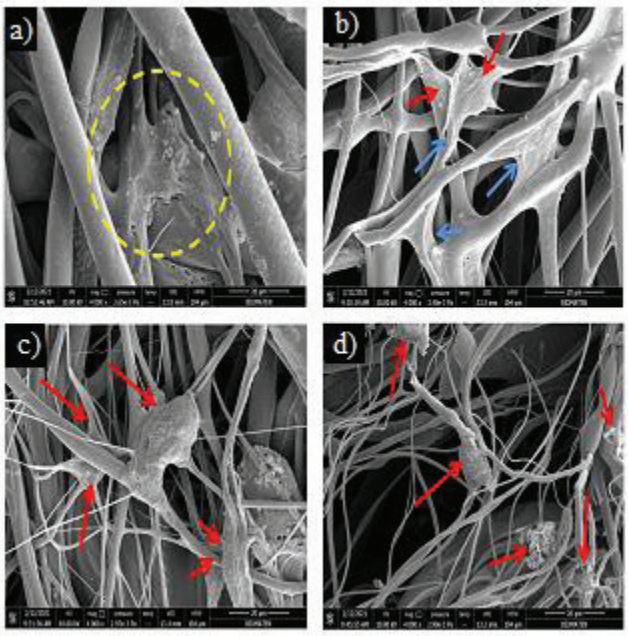

Figure 3.29 SEM images of Saos-2 cells on PCL scaffolds at the end of 1st day: a) PCL, b) PCL-Zn HA, c) PCL-Zn HA-BNNF, d) PCL-BNNF (Scale bar: 20 µm). (Red arrows: Adhered cells, Blue Arrows: Spread cells, Yellow circle: Cell sheet).

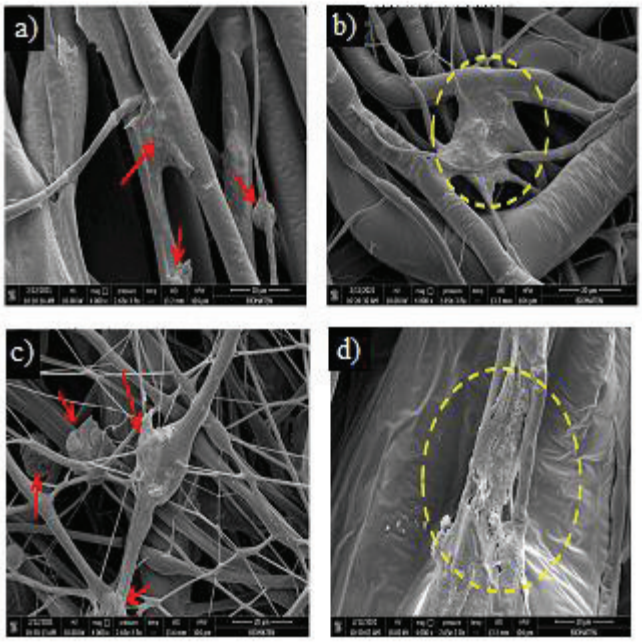

Figure 3.30 SEM images of Saos-2 cells on PCL scaffolds at the end of 7th day: a) PCL, b) PCL-Zn HA, c) PCL-Zn HA-BNNF, d) PCL-BNNF (Scale bar: 20 μm). (Red arrows: Adhered cells, Blue Arrows: Spread cells, Yellow circle: Cell sheet).

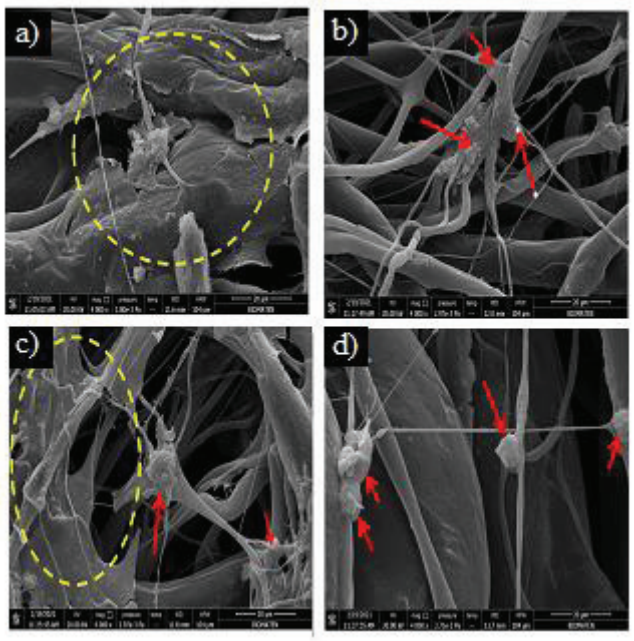

Figure 3.31 SEM images of Saos-2 cells on scaffolds at the end of 14th day: a) PCL, b) PCL-Zn HA, c) PCL-Zn HA-BNNF, d) PCL-BNNF (Scale bar: 20 μm). (Red arrows: Adhered cells, Yellow circle: Cell sheet).

3.4.4 Evaluation of Osteogenic Activity of Polycaprolactone Composite Scaffolds

The osteogenic activity of the scaffolds was also studies by determining of alkaline phosphatase (ALP) activity of Saos-2 cells on the PCL, PCL-Zn HA, PCL-Zn HA-BNNF and PCL-BNNF scaffolds (Figure 3.32). Thus, ALP is an enzyme of dephosphorylating hydrolase which hydrolyzes pyrophosphate to phosphate. These free phosphate ions improve calcium phosphate mineralization (Nagarajan et al., 2017). In short, ALP is used to show the generation of new bone in the presence of osteoblast cells. The highest cell viability was obtained in PCL-Zn HA-BNNF group at the end of second week. This can be because of release of zinc and boron ions from the scaffolds of Zn HA and BNNF in more controlled way in the PCL matrix (Ito et al., 2005; Li et al., 2016). In a study, Ito et al., (2005) investigated effect of Zn^{2+} in the composite of β-TCP/HA on ALP activity of bone marrow cells. The results showed that when the amount of Zn^{2+} was at the 1.26 wt%, the ALP activity of the cells was 3 or 4 fold higher than observed in the

undoped HA group. The zinc concentration in the cell culture medium was about 2.2-7.2 μg/ml which was higher than the plasma of rat and human. The release of boron from BNNFs was achieved by hydrolyzing BNNFs into ammonia and boric acid, which turn into ammonium borate hydrates. Although, the synthesized BNNFs are highly stable, the presence of structural defects and hydroxyl groups are found on their edges after sonication and oxidation. In the cell culture medium, the presence of defect site near the boron-nitrogen bonds in the BN nanostructures are more prone to the attack of oxygen in water molecules. Thus, as adjacent part is dissolved, defects parts propagate. As a result of this, boron is released very slowly in the structure of BN nanostructures. It was previously reported that low level of boron releasing (0.1-100 ng/ml) significantly improved the bone related protein levels and gene expression in osteoblasts (MC3T3-E1) thus would lead to mineralization and enhancing osteogenesis (Li et al., 2016). In this study, 1-10 μg/ml of BNNTs provided 0.1-1 ng/ml of boron released into Tris-HCI after 1 week of incubation. This enabled higher ALP activity of MSCs in the culture medium. Similar results were found with bone marrow stromal cells (BMSCs) (Ying et al., 2011). Similar results were obtained in the other studies. The low concentration of released boron (1, 10 and 100 ng/ml) enhanced the osteogenic differentiation by inducing osteogenic differentiation-related marker gene expression, improving calcium deposition and then ALP activity of human BMSCs but proliferation of BMSCs was inhibited at high concentration of boron (100 ng/ml) (Ying et al., 2011). In our study, ALP activity of Saos-2 cells on the PCL-BNNF was lower than the control groups and other PCL groups at the end of 14. days. The reason behind be the release of boron into medium from BNNF. This high concentration of boron into medium might have lowered the ALP activity and cell growth (Ying et al., 2011).

In the group of PCL-Zn HA, Saos-2 cells also showed higher ALP activity than groups of PCL and PCL-BNNF without causing any cytotoxic effect at the end of 14 days. This can be due to dissolution of Zn HA into zinc, phosphate and calcium ions which enable the osteogenic differentiation and increasing the bone cell mineralization (Chuenjitkuntaworn et al., 2009; Ito et al., 2005). Thus, ALP

activity at 14th day in the presence of PCL-Zn HA was higher compared to PCL control group was an expected outcome. The similar results were obtained with human osteoblast cells in the presence of PCL-HA scaffolds with improved cell viability, proliferation and osteoconduction properties than that of only PCL groups (Causa et al., 2006).

The highest ALP activity was obtained in the PCL-Zn HA- BNNF group at days 7 and 14 due to release of proper amount of zinc, calcium, phosphate, boron and ammonium. These results were consistent with the cell viability results. In the Alamar study, the cell viability decreased in the presence of PCL-Zn HA-BNNF after 7. days. This can be explained by that cells on the PCL-Zn HA-BNNF reached confluence earlier than other PCL groups and underwent osteogenic differentiation and then continued with bone formation process until day14.

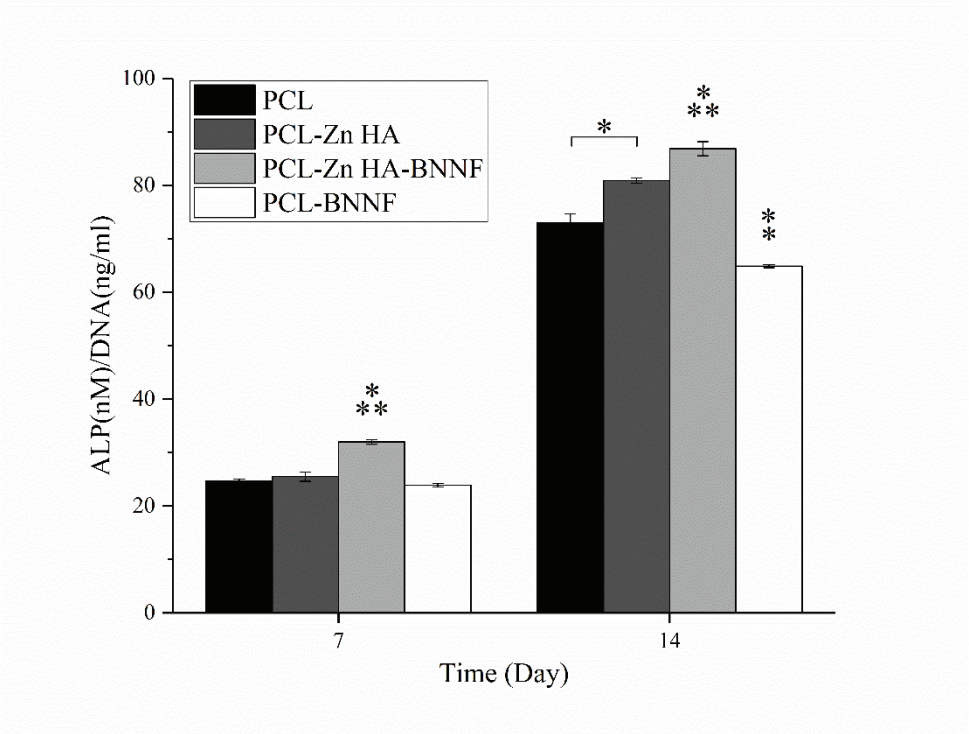

Figure 3.32 Specific ALP activity of Saos-2 cells seeded on the scaffolds after 7 and 14 days of incubation "**" refers that to the significantly lowest group, whereas "***" stands for significantly the highest group at a given time point. "*" indicates the statistical difference between the groups (n=8, $p<0.05$).

CHAPTER 4

CONCLUSION

This study investigated the synthesis and characterization of BNNF and Zn HA and their composition with PCL matrix through the rotary jet spinning (RJS) for the first time to fabricate the scaffolds for bone tissue engineering (BTE). Each material synthesized (BNNF and Zn HA) was verified by SEM, XRD, FTIR and XPS analysis. Additionally, the bioactivity studies showed that blending of Zn HA and BNNF with PCL resulted in higher CaP precipitation on the scaffolds. *In vitro* cell studies showed that presence of both Zn HA and BNNF also had synergistic effect for enhanced proliferation and osteogenic activity of Saos-2 cells. PCL-Zn HA-BNNF composite scaffolds hold promise as bone substitutes for bone repair. Mechanical tests showed that the scaffold of PCL-Zn HA-BNNF has a potential usage in the nonload bearing applications such as cartilage or skull. These results showed that PCL-Zn HA-BNNF scaffolds prepared by RJS method which is a fast, cost efficient, reproducible and industrial scale production method hold potential for BTE.

REFERENCES

Abidi, S. S. A., & Murtaza, Q. (2014). Synthesis and charactesization of nano-hydroxyapatite powder using wet chemical precipitation reaction. *Journal of Materials Science & Technology*, 30 (4), 307-310. https://doi.org/10.1016/j.jmst.2013.10.011.

Akcay, B. (2012). Experimental investigation on uniaxial tensile strength of hybrid fibre concrete. *Composites Part B: Engineering*, 43 (2), 766–778. https://doi.org/10.1016/j.compositesb.2011.08.017.

Albulescu, R., Popa, A.-C., Enciu, A.-M., Albulescu, L., Dudau, M., Popescu, I. D., Mihai, S., Codrici, E., Pop, S., Lupu, A.-R., Stan, G. E., Manda, G., & Tanase, C. (2019). Comprehensive in vitro testing of calcium phosphate-based bioceramics with orthopedic and dentistry applications. *Materials*, 12 (22), 1–41. https://doi.org/10.3390/ma12223704.

Albee, F., & Morrison, H. (1920). Studies in bone growth: triple calcium phosphate as a stimulus to osteogenesis. *Annals of Surgery*, 71 (1), 32-39. https://dx.doi.org/10.1097%2F00000658-192001000-00006.

Andrade, T. M., Mello, D. C. R., Elias, C. M. V., Abdala, J. M. A., Silva, E., Vasconcellos, L. M. R., Tim, C. R., Marciano, F. R., & Lobo, A. O. (2019). In vitro and in vivo evaluation of rotary-jet spun poly (ε- caprolactone) with high loading of nano-hydroxyapatite. *Journal of Materials Science. Materials in Medicine*, 30 (2), 19. https://doi.org/10.1007/s10856-019-6222-1.

Anindyajati, A., Boughton, P., & Ruys, A. (2015). The effect of rotating collector design on tensile properties and morphology of electrospun polycaprolactone fibres. *MATEC Web of Conferences,* 27, 02002. https://doi.org/10.1051/matecconf/20152702002.

Ashraf, M. A., Peng, W., Zare, Y., & Rhee, K. Y. (2018). Effects of size and aggregation/agglomeration of nanoparticles on the interfacial/interphase properties and tensile strength of polymer nanocomposites. *Nanoscale Research Letters,* 13 (1), 214. https://doi.org/10.1186/s11671-018-2624-0.

Badrossamay, M. R., McIlwee, H. A., Goss, J. A., & Parker, K. K. (2010). Nanofiber assembly by rotary jet-spinning. *Nano Letters*, 10 (6), 2257–2261. https://doi.org/10.1021/nl101355x.

Badrossamay, M. R., Balachandran, K., Capulli, A. K., Golecki, H. M., Agarwal, A., Goss, J. A., Kim, H., Shin, K., Parker, K. K. (2014). Engineering hybrid polymer-protein super-aligned nanofibers via rotary jet spinning. *Biomaterials*, 35 (10), 3188-3197. https://doi.org/10.1016/j.biomaterials.2013.12.072.

Barbosa, M. C., Messmer, N. R., Brazil, T. R., Marciano, F. R., & Lobo, A. O. (2013). The effect of ultrasonic irradiation on the crystallinity of nano-hydroxyapatite produced via the wet chemical method. *Materials Science and Engineering C*, 33 (5), 2620–2625. https://doi.org/10.1016/j.msec.2013.02.027

Bayrak, E., Ozcan, B., & Erisken, C. (2016). Processing of polycaprolactone and hydroxyapatite to fabricate graded electrospun composites for tendon-bone interface regeneration. *Journal of Polymer Engineering,* 37 (1), 99-106. https://doi.org/10.1515/polyeng-2016-0017.

Begam, H., Kundu, B., Chanda, A., & Nandi, S. K. (2017). MG63 osteoblast cell response on Zn doped hydroxyapatite (HAp) with various surface features. *Ceramics International*, 43 (4), 3752–3760. https://doi.org/10.1016/j.ceramint.2016.12.010.

Berzina-Cimdina, L., Borodajenko, N (2012). Research of calcium phophates using Fourier transform infrared spectroscopy, Infrared spectroscopy-materials science, engineering and technology, Prof. Theophanides Theophile

(Ed.). https://doi.org/10.5772/36942

Bernard, S., Chassagneux, F., Berthet, M. P., Vincent, H., & Bouix, J. (2002). Structural and mechanical properties of a high-performance BN fibre. *Journal of the European Ceramic Society*, 22 (12), 2047–2059. https://doi.org/10.1016/S0955-2219(01)00524-6.

Bhardwaj, N., & Kundu, S. C. (2010). Electrospinning: A fascinating fiber fabrication technique. *Biotechnology Advances*, 28 (3), 325–347. https://doi.org/10.1016/j.biotechadv.2010.01.004.

Bhattacharjee, A., Gupta, A., Verma, M., Murugan, P. A., Sengupta, P., Matheshwaran, S., Manna, I., & Balani, K. (2019). Site-specific antibacterial efficacy and cyto/hemo-compatibility of zinc substituted hydroxyapatite. *Ceramics International*, 45 (9), 12225–12233. https://doi.org/10.1016/j.ceramint.2019.03.132.

Blase, X., Rubio, A., Louie, S. G., & Cohen, M. L. (1994). Stability and band gap constancy of boron nitride nanotubes. *Europhysics Letters,* 28 (5), 335-340. https://doi.org/10.1209/0295-5075/28/5/007.

Bohns, F. R., Degrazia, F. W., Balbinot, G. de S. B., Leitune, V. C. B., Samuel, S. M. W., García-Esparza, M. A., Sauro, S., & Collares, F. M. (2019). Boron nitride nanotubes as filler for resin-based dental sealants, *Scientific Reports*, 9, 7710. https://doi.org/10.1038/s41598-019-44246-8.

Bonnier, F., Keating, M. E., Wróbel, T. P., Majzner, K., Baranska, M., Garcia-Munoz, A., Blanco, A., & Byrne, H. J. (2015). Cell viability assessment using the Alamar blue assay: A comparison of 2D and 3D cell culture models. *Toxicology in Vitro,* 29 (1), 124-131. https://doi.org/10.1016/j.tiv.2014.09.014.

Bovani, D., Allazadeh, M. R., Rasouli, S., Khodadad, E., & Borhani, E. (2019). Studying the effect of hydroxyapatite particles in osteoconductivity of Ti-HA bioceramics. *Journal of the Australian Ceramic Society*, 55, 395-403.

https://doi.org/10.1007/s41779-018-0247-7.

Bundy, F. P., & Wentorf, R. H. (1963). Direct transformation of hexagonal boron nitride to denser forms. *The Journal of Chemical Physics*, 38 (5), 1144–1149. https://doi.org/10.1063/1.1733815.

Bundy, F. P., (1965) US Patent Application No. 3,212,852.

Causa, F., Netti, P. A., Ambrosio, L., Ciapetti, G., Baldini, N., Pagani, S., Martini, D., & Giunti, A. (2006). Poly-ε-caprolactone/hydroxyapatite composites for bone regeneration: In vitro characterization and human osteoblast response. *Journal of Biomedical Materials Research - Part A*, 76 (1), 151-162. https://doi.org/10.1002/jbm.a.30528

Chen, J. P., & Chang, Y. S. (2011). Preparation and characterization of composite nanofibers of polycaprolactone and nanohydroxyapatite for osteogenic differentiation of mesenchymal stem cells. *Colloids and Surfaces B: Biointerfaces*, 86 (1), 169–175. https://doi.org/10.1016/j.colsurfb.2011.03.038

Chen, K.-Y., Liao, W.-J., Kuo, S.-M., Tsai, F.-J., & Chen, Y.-S., Huang, C.-Y., & Yao, C.-H. (2009). Asymmetric chitosan membrane containing collagen I nanospheres for skin tissue engineering. *Biomacromolecules*, 10 (6), 1642–1649. https://doi.org/10.1021/bm900238b

Chen, Y., Chadderton, L. T., Gerald, J. F., & Williams, J. S. (1999). A solid-state process for formation of boron nitride nanotubes. *Applied Physics Letters*, 74 (20), 2960-2962. https://doi.org/10.1063/1.123979

Chen, Y. I., & Zou, J. (2004). Boron nitride nanotubes: Pronounced resistance to oxidation. *Applied Physics Letter*, 84, 2430. https://doi.org/10.1063/1.1667278

Cho, H., Kim, J. H., Hwang, J. H., Kim, C. S., Jang, S. G., Park, C., Lee, H., & Kim, M. J. (2020). Single- and double-walled boron nitride nanotubes : Controlled synthesis and application for water purification. *Scientific Reports*

10, 7416. https://doi.org/10.1038/s41598-020-64096-z

Chong, E. J., Phan, T. T., Lim, I. J., Zhang, Y. Z., Bay, B. H., Ramakrishna, S., & Lim, C. T. (2007). Evaluation of electrospun PCL/gelatin nanofibrous scaffold for wound healing and layered dermal reconstitution. *Acta Biomaterialia*, 3 (3), 321–330. https://doi.org/10.1016/j.actbio.2007.01.002.

Chopra, N. G., Luyken, R. J., Cherrey, K., Crespi, V. H., Cohen, M. L., Louie, S. G., & Zettl, A. (1995). Boron nitride nanotubes. *Science*, 269 (5226), 966–967. https://doi.org/10.1126/science.269.5226.966.

Chuenjitkuntaworn, B., Supaphol, P., Pavasant, P., & Damrongsri, D. (2009). Electrospun poly(L-lactic acid)/hydroxyapatite composite fibrous scaffolds for bone tissue engineering. *Polymer International*, 59 (2), 227-235. https://doi.org/10.1002/pi.2712.

Chuenjitkuntaworn, B., Inrung, W., Damrongsri, D., Mekaapiruk, K., Supaphol, P., & Pavasant, P. (2010). Polycaprolactone/hydroxyapatite composite scaffolds: Preparation, characterization, and in vitro and in vivo biological responses of human primary bone cells. *Journal of Biomedical Materials Research-Part A*, 94A (1), 241–251. https://doi.org/10.1002/jbm.a.32657.

da Silva, W. M., Ferreira, H., Morais, C. A., Leal, A. S., Sousa, E. M. B., & Sousa, B. (2018). Smarium doped boron nitride nanotubes. *Applied Radiation and Isotopes*, 131, 30-35. https://doi.org/10.1016/j.apradiso.2017.10.045

Deliormanlı, A. M., Konyalı, R. (2019). Bioactive glass/hydroxyapatite-containing electrospun poly(Ɛ-caprolactone) composite nanofibers for bone tissue engineering. Journal of the Australian Ceramic Society 55, 247-256. https://doi.org/10.1007/s41779-018-0229-9.

Deveci, M. Z. Y., Gönenci, R., Canpolat, İ., & Kanat, Ö. (2020). In vivo biocompatibility and fracture healing of hydroxyapatite-hexagonal boron nitride-chitosan-collagen biocomposite coating in rats. *Turkish Journal of*

Veterinary and Animal Sciences, 44, 76–88. https://doi.org/10.3906/vet-1906-21.

Degrazia, F. W., Leitune, V. C. B., Samuel, S. M. W., & Collares, F. M. (2017). Boron nitride nanotubes as novel fillers for improving the properties of dental adhesives. *Journal of Dentistry*, 62, 85-90. https://doi.org/10.1016/j.jdent.2017.05.013

Dolati, S., Fereidoon, A., & Kashyzadeh, K. R. (2012). A comparison study between boron nitride nanotubes and carbon nanotubes. *International Journal of Emerging Technology and Advanced Engineering*, 2 (10), 470-474.

Dorozhkin, S. V. (2010). Bioceramics of calcium orthophosphates. *Biomaterials*, 31 (7), 1465–1485. https://doi.org/10.1016/j.biomaterials.2009.11.050

Drury, J. L., & Mooney, D. J. (2003). Hydrogels for tissue engineering: scaffold design variables and applications. *Biomaterials*, 24 (24), 4337–4351. https://doi.org/10.1016/S0142-9612(03)00340-5.

Dubok, V. A. (2000). Bioceramics - Yesterday, today, tomorrow. *Powder Metallurgy and Metal Ceramics,* 39*,* 381-394. https://doi.org/10.1023/a:1026617607548.

Dwivedi, R., Kumar, S., Pandey, R., Mahajan, A., Nandana, D., Katti, D. S., & Mehrotra, D. (2020). Polycaprolactone as biomaterial for bone scaffolds: Review of literature. *Journal of Oral Biology and Craniofacial Research*, 10 (1), 381–388. https://doi.org/10.1016/j.jobcr.2019.10.003.

Eftekhari, H., Jahandideh, A., Asghari, A., Akbarzadeh, A., & Hesaraki, S. (2017). Assessment of polycaprolacton (PCL) nanocomposite scaffold compared with hydroxyapatite (HA) on healing of segmental femur bone defect in rabbits. *Artificial Cells, Nanomedicine and Biotechnology*, 45 (5), 961–968. https://doi.org/10.1080/21691401.2016.1198360.

Eliaz, N., & Metoki, N. (2017). Calcium phosphate bioceramics : A review of

their history, structure, properties, coating technologies and biomedical applications. *Materials*, 10 (4), 334. https://doi.org/10.3390/ma10040334

Emanet, M., Kazanç, E., Çobandede, Z., & Çulha, M. (2016). Boron nitride nanotubes enhance properties of chitosan- based scaffolds. *Carbohydrate Polymers*, 151, 313-320. https://doi.org/10.1016/j.carbpol.2016.05.074

Fabbri, P., Bondioli, F., Messori, M., Bartoli, C., Dinucci, D., & Chiellini, F. (2010). Porous scaffolds of polycaprolactone reinforced with in situ generated hydroxyapatite for bone tissue engineering. *Journal of Materials Science: Materials in Medicine*, 21 (1), 343–351. https://doi.org/10.1007/s10856-009-3839-5.

Fowler, B. O. (1974). Infrared studies of apatites. I. Vibrational assignments for calcium, strontium, and barium hydroxyapatites utilizing isotopic substitution. *Inorganic Chemistry,* 13 (1)*,* 194-207. https://doi.org/10.1021/ic50131a039

Geick, R., Perry, C. H., & Rupprecht, G. (1966). Normal modes in hexagonal boron nitride. *Physical Review*, 146 (2), 543-547. https://doi.org/10.1103/PhysRev.146.543.

Ghorbani, F. M., Kaffashi, B., Shokrollahi, P., Seyedjafari, E., Ardeshirylajimi, A. (2015). PCL/chitosan/Zn-doped nHA electrospun nanocomposite scaffold promotes adipose derived stem cells adhesion and proliferation, *Carbonhydrate Polymers*, 118, 133-142. https://doi.org/10.1016/j.carbpol.2014.10.071.

Gnaneshwar, P. V., Sudakaran, S. V., Abisegapriyan, S., Sherine, J., Ramakrishna, S., Rahim, M. H. A., Yusoff, M. M., Jose, R., Venugopal, J. R. (2019). Ramification of zinc oxide doped hydroxyapatite biocomposites for the mineralization of osteoblasts. *Materials Science and Engineering C*, 96, 337–346. https://doi.org/10.1016/j.msec.2018.11.033.

Golberg, D., Bando, Y., Kurashima, K., & Sato, T. (2001). Synthesis and

characterization of ropes made of BN multiwalled nanotubes. *Scripta Materialia*, 44 (8–9), 1561–1565. https://doi.org/10.1016/S1359-6462(01)00724-2.

Gonzalez, G. M., MacQueen, L. A., Lind, J. U., Fitzgibbons, S. A., Chantre, C. O., Huggler, I., Golecki, H. M., Goss, J. A., & Parker, K. K. (2017). Production of synthetic, para-aramid and biopolymer nanofibers by immersion rotary jet-spinning. *Macromolecular Materials and Engineering*, 302 (1), 1600365. https://doi.org/10.1002/mame.201600365.

Groppo, M. F., Caria, P. H., Freire, A. R., Figueroba, S. R., Ribeiro-Neto, W. A., Bretas, R. E. S., Prado, F. B., Haiter-Neto, F., Aguiar, F. H., Rossi, A. C. (2017). The effect of a hydroxyapatite impregnated PCL membrane in rat subcritical calvarial bone defects. *Archives of Oral Biology*, 82, 209-215. https://doi.org/10.1016/j.archoralbio.2017.06.018.

Grzeszczyk, S., Matuszek-Chmurowska, A., Vejmelková, E., & Cerný, R. (2020). Reactive powder concrete containing basalt fibers: strength, abrasion and porosity. *Materials*, 13, 2948. https://doi.org/10.3390/ma13132948.

Guarino, V., Causa, F., Taddei, P., di Foggia, M., Ciapetti, G., Martini, D., Fagnano, C., Baldini, N., & Ambrosio, L. (2008). Polylactic acid fibre-reinforced polycaprolactone scaffolds for bone tissue engineering. *Biomaterials*, 29 (27), 3662–3670. https://doi.org/10.1016/j.biomaterials.2008.05.024

Guner, M. B., Dalgic, A. D., Tezcaner, A., Yilanci, S., & Keskin, D. (2020). A dual-phase scaffold produced by rotary jet spinning and electrospinning for tendon tissue engineering. *Biomedical Materials*, 15 (6), 065014. https://doi.org/10.1088/1748-605x/ab9550

Guo, W., Jia, X., Guo, W. L., Xu, H. W., Shang, J., & Ma, H. A. (2010). Effects of additive LiF on the synthesis of cBN in the system of Li 3N-hBN at HPHT. *Diamond and Related Materials*, 19 (10), 1296–1299. https://doi.org/10.1016/j.diamond.2010.06.001

Guo, Y., Lyu, Z., Yang, X., Lu, Y., Ruan, K., Wu, Y., Kong, J., & Gu, J. (2019). Enhanced thermal conductivities and decreased thermal resistances of functionalized boron nitride/polyimide composites. *Composites Part B: Engineering,* 164, 732-739. https://doi.org/10.1016/j.compositesb.2019.01.099

Hassan, M. I., Sultana, N., & Hamdan, S. (2014). Bioactivity assessment of poly(ε -caprolactone)/hydroxyapatite electrospun fibers for bone tissue engineering application. *Journal of Nanomaterials*, 2014, 1-7. https://doi.org/10.1155/2014/573238

Haubner, R., Wilhelm, M., Weissenbacher, R., & Lux, B. (2002). Boron nitrides-properties, synthesis and applications. In *High Performance Non-Oxide Ceramics II*, (Vol. 102, pp. 1–45). https://doi.org/10.1007/3-540-45623-6_1

Heness, G. & Ben-Nissan, B. (2015). Innovative Bioceramics. *Materials Forum*, 27, 104-114.

Henkel, J., Woodruff, M. A., Epari, D. R., Steck, R., Glatt, V., Dickinson, I. C., Choong, P. F. M., Schuetz, M. A., Hutmacher, D. W. (2013). Bone regeneration based on tissue engineering conceptions-A 21st century perspective, *Bone Research*, 1 (3), 216-248. https://doi.org/10.4248/br201303002.

Hernández, E., Goze, C., Bernier, P., Rubio, A. (1998). Elastic properties of C and BxCyNz composite nanotubes, *Physical Review Letters*, 80 (20), 4502-4505. https://doi.org/10.1103/PhysRevLett.80.4502.

Hilder, T. A., Gordon, D., & Chung, S. (2009). Salt rejection and water transport through boron nitride nanotubes, *Small*, 5 (19), 2183–2190. https://doi.org/10.1002/smll.200900349.

Horváth, L., Magrez, A., Golberg, D., Zhi, C., Bando, Y., Smajda, R., Horváth, E., Forró, L., & Schwaller, B. (2011). In vitro investigation of the cellular toxicity of boron nitride nanotubes. *ACS Nano,* 5 (5), 3800-3810.

https://doi.org/10.1021/nn200139h

Huang, C., Chen, R., Ke, Q., Morsi, Y., Zhang, K., & Mo, X. (2011). Electrospun collagen-chitosan-TPU nanofibrous scaffolds for tissue engineered tubular grafts. *Colloids and Surfaces B: Biointerfaces*, 82 (2), 307–315. https://doi.org/10.1016/j.colsurfb.2010.09.002

Huang, Q., Bando, Y., Zhao, L., Zhi, C. Y., & Golberg, D. (2009). pH sensor based on boron nitride nanotubes. *Nanotechnology*, 20 (41), 415501. https://doi.org/10.1088/0957-4484/20/41/415501

Huang, Y., Zhang, H., Qiao, H., Nian, X., Zhang, X., Wang, W., Zhang, X., Chang, X., Han, S., & Pang, X. (2015). Anticorrosive effects and in vitro cytocompatibility of calcium silicate/zinc-doped hydroxyapatite composite coatings on titanium. *Applied Surface Science*, 357, 1776–1784. https://doi.org/10.1016/j.apsusc.2015.10.034

Hwang, H. J., Barakat, N. A. M., Kanjwal, M. A., Sheikh, F. A., Kim, H. Y., & Abadir, M. F. (2010). Boron nitride nanofibers by the electrospinning technique. *Macromolecular Research*, 18 (6), 551–557. https://doi.org/10.1007/s13233-010-0601-2.

Ikeuchi, M., Ito, A., Dohi, Y., Ohgushi, H., Shimaoka, H., Yonemasu, K., & Tateishi, T. (2003). Osteogenic differentiation of cultured rat and human bone marrow cells on the surface of zinc-releasing calcium phosphate ceramics. *Journal of Biomedical Materials Research Part A*, 67A (4), 1115-1122. https://doi.org/10.1002/jbm.a.10041

Ito, A., Ojima, K., Naito, H., Ichinose, N., & Tateishi, T. (2000). Preparation, solubility, and cytocompatibility of zinc-releasing calcium phosphate ceramics. *Journal of Biomedical Materials Research*, 50 (2), 178–183. https://doi.org/10.1002/(sici)1097-4636(200005)50:2<178::aid-jbm12>3.0.co;2-5.

Ito, A., Otsuka, M., Kawamura, H., Ikeuchi, M., Ohgushi, H., Sogo, Y., &

Ichinose, N. (2005). Zinc-containing tricalcium phosphate and related materials for promoting bone formation. *Current Applied Physics*, 5 (5), 402-406. https://doi.org/10.1016/j.cap.2004.10.006.

Jayakumar, R., Prabaharan, M., Nair, S. V, & Tamura, H. (2010). Novel chitin and chitosan nanofibers in biomedical applications. *Biotechnology Advances*, 28 (1), 142–150. https://doi.org/10.1016/j.biotechadv.2009.11.001

Jhi, S.-H., & Kwon, Y.-K. (2004). Hydrogen adsorption on boron nitride nanotubes: A path to room-temperature hydrogen storage. *Physical Review B*, 69 (24), 245407. https://doi.org/10.1103/PhysRevB.69.245407.

Kang, H., Tabata, Y., & Ikada, Y. (1999). Fabrication of porous gelatin scaffolds for tissue engineering. *Biomaterials*, 20 (14), 1339-1344. https://doi.org/10.1016/s0142-9612(99)00036-8.

Kashkarov, V. M., Goloshchapov, D. L., Rumyantseva, A. N., Seredin, P. V., Domashevskaya, E. P., Spivakova, I. A., & Shumilovich, B. R. (2011). X-ray diffraction and IR spectroscopy investigation of synthesized and biogenic nanocrystalline hydroxyapatite. *Journal of Surface Investigation*, 5, 1162-1167. https://doi.org/10.1134/S1027451011120068.

Kew, S. J., Gwynne, J. H., Enea, D., Abu-rub, M., Pandit, A., Zeugolis, D., Brooks, R. A., Rushton, N., Best, S. M. & Cameron, R. E. (2011). Regeneration and repair of tendon and ligament tissue using collagen fibre biomaterials. *Acta Biomaterialia*, 7 (9), 3237–3247. https://doi.org/10.1016/j.actbio.2011.06.002.

Kim, J. H., Pham, T. V., Hwang, J. H., Kim, C. S., & Kim, M. J. (2018). Boron nitride nanotubes: synthesis and applications. *Nano Convergence*, 5 (1), 17. https://doi.org/10.1186/s40580-018-0149-y.

Kim, Y.-H., & Lee, B.-T (2011). Novel approach to the fabrication of an artificial small bone using a combination of sponge replica and electrospinning methods. *Science and Technology of Advaanced Materials*, 12 (3), 035002.

https://doi.org/10.1088/1468-6996/12/3/035002

Kokubo, T., Kushitani, H., Sakka, S., Kitsugi, T., & Yamamuro, T. (1990). Solutions able to reproduce in vivo surface-structure changes in bioactive glass-ceramic A-W. *Journal of Biomedical Materials Research*, 24 (6), 721–734. https://doi.org/10.1002/jbm.820240607.

Koons, G. L., Diba, M., & Mikos, A. G. (2020). Materials design for bone-tissue engineering, *Nature Reviews Materials*, 5, 584-603. https://doi.org/10.1038/s41578-020-0204-2

Kowalczuk, P. B., & Drzymala, J. (2016). Physical meaning of the Sauter mean diameter of spherical particulate matter. *Particulate Science and Technology*, 34 (6), 645-647. https://doi.org/10.1080/02726351.2015.1099582.

Kudin, K. N., Scuseria, G. E., & Yakobson, B. I. (2001). C_2F, BN, and C nanoshell elasticity from ab initio computations, *Physical Review B*, 64, 235406. https://doi.org/10.1103/PhysRevB.64.235406.

Kumbar, S G, Kulkarni, A. R., & Aminabhavi, T. M. (2002). Crosslinked chitosan microspheres for encapsulation of diclofenac sodium: effect of crosslinking agent. *Journal of Microencapsulation*, 19 (2), 173–180. https://doi.org/10.1080/02652040110065422.

Kumbar, S. G., Nukavarapu, S. P., James, R., Nair, L. S., & Laurencin, C. T. (2008). Electrospun poly (lactic acid- co -glycolic acid) scaffolds for skin tissue engineering. *Biomaterials*, 29 (30), 4100–4107. https://doi.org/10.1016/j.biomaterials.2008.06.028.

Kurkijärvi, J. E., Nissi, M. J., Kiviranta, I., Jurvelin, J. S., & Nieminen, M. T. (2004). Delayed gadolinium-enhanced MRI of cartilage (dGEMRIC) and T_2 characteristics of human knee articular cartilage: topographical variation and relationships to mechanical properties. *Magnetic Resonance in Medicine*, 52 (1), 41-46. https://doi.org/10.1002/mrm.20104

Lahiri, D., Rouzaud, F., Richard, T., Keshri, A. K., Bakshi, S. R., Kos, L., &

Agarwal, A. (2010). Boron nitride nanotube reinforced polylactide–polycaprolactone copolymer composite : Mechanical properties and cytocompatibility with osteoblasts and macrophages in vitro. *Acta Biomaterialia*, 6 (9), 3524–3533. https://doi.org/10.1016/j.actbio.2010.02.044

Lahiri, D., Singh, V., Benaduce, A. P., Seal, S., Kos, L., & Agarwal, A. (2011). Boron nitride nanotube reinforced hydroxyapatite composite: Mechanical and tribological performance and in-vitro biocompatibility to osteoblasts. *Journal of the Mechanical Behavior of Biomedical Materials*, 4 (1), 44-56. https://doi.org/10.1016/j.jmbbm.2010.09.005

Lai, Y. S., Chen, W. C., Huang, C. H., Cheng, C. K., Chan, K. K., & Chang, T. K. (2015). The effect of graft strength on knee laxity and graft in-situ forces after posterior cruciate ligament reconstruction. *PLoS One,* 10 (5), 1-11. https://doi.org/10.1371/journal.pone.0127293.

Laurencin, C. T. & Freeman, J. W. (2005). Ligament tissue engineering : An evolutionary materials science approach. *Biomaterials* 26 (36), 7530–7536. https://doi.org/10.1016/j.biomaterials.2005.05.073

Lee, R. S., Gavillet, J., De La Chapelle, M. L., Loiseau, A., Cochon, J.-L., Pigache, D., Thibault, J., & Willaime, F. (2001). Catalyst-free synthesis of boron nitride single-wall nanotubes with a preferred zig-zag configuration. *Physical Review B*, 64 (12), 121405. https://doi.org/10.1103/PhysRevB.64.121405.

Lengsfeld, A. M., Löw, I., Wieland, T., Dancker, P., & Hasselbach, W. (1974). Interaction of phalloidin with actin. *Proceedings of the National Academy of Sciences of the United States of America*, 71 (7), 2803-2807. https://doi.org/10.1073/pnas.71.7.2803.

Lewinski, N., Colvin, V., & Drezek, R. (2008). Cytotoxicity of nanoparticles. *Small*, 4 (1), 26–49. https://doi.org/10.1002/smll.200700595

Li, R., Lin, J., Fang, Y., Yu, C., Zhang, J., Xue, Y., Liu, Z., Zhang, J., Tang, C., & Huang, Y. (2018). Porous boron nitride nanofibers/PVA hydrogels with improved mechanical property and thermal stability. *Ceramics International*, 44 (18), 22439-22444. https://doi.org/10.1016/j.ceramint.2018.09.011.

Li, X., Wang, X., Jiang, X., Yamaguchi, M., Ito, A., Bando, Y., & Golberg, D. (2016). Boron nitride nanotube-enhanced osteogenic differentiation of mesenchymal stem cells. *Journal of Biomedical Materials Research - Part B Applied Biomaterials*, 104 (2), 323-329 https://doi.org/10.1002/jbm.b.33391.

Lin, J., Xu, L., Huang, Y., Li, J., Wang, W., Feng, C., Liu, Z., Xu, X., Zou, J., & Tang, C. (2016). Ultrafine porous boron nitride nanofibers synthesized via a freeze-drying and pyrolysis process and their adsorption properties*, RSC Advances,* 6, 1253-1259. https://doi.org/10.1039/c5ra23426c

Liu, K., Zhang, C., Sun, Y., Zhang, G., Shen, X., Zou, F., Zhang, H., Wu, Z., Wegener, E. C., Taubert, C. J., Miller, J. T., Peng, Z., & Zhu, Y. (2018). High-performance transition metal phosphide alloy catalyst for oxygen evolution reaction. *ACS Nano*, 12 (1), 158–167. https://pubs.acs.org/doi/10.1021/acsnano.7b04646

Liu, Y., Ma, L., & Gao, C. (2012). Facile fabrication of the glutaraldehyde cross-linked collagen/chitosan porous scaffold for skin tissue engineering. *Materials Science & Engineering C*, 32 (8), 2361–2366. https://doi.org/10.1016/j.msec.2012.07.008.

Liu, Z., Zhao, K., Luo, J., & Tang, Y. (2019). Electrospinning of boron nitride nanofibers with high temperature stability. *Scripta Materialia* 170, 116-119. https://doi.org/10.1016/j.scriptamat.2019.06.002.

Lobo, A. O., Afewerki, S., de Paula, M. M. M., Ghannadian, P., Marciano, F. R., Zhang, Y. S., Webster, T. J., & Khademhosseini, A. (2018). Electrospun nanofiber blend with improved mechanical and biological performance. *International Journal of Nanomedicine*, 13, 7891-7903. https://doi.org/10.2147/IJN.S175619.

Loiseau, A., Willaime, F., Demoncy, N., Hug, G., & Pascard, H. (1996). Boron nitride nanotubes with reduced numbers of layers synthesized by arc discharge. *Physical Review Letters*, 76 (25), 4737-4740. https://doi.org/10.1103/physrevlett.76.4737.

Lourie, O. R., Jones, C. R., Bartlett, B. M., Gibbons, P. C., Ruoff, R. S., & Buhro, W. E. (2000). CVD growth of boron nitride nanotubes. *Chemistry of Materials*, 12 (7), 1808–1810. https://doi.org/10.1021/cm000157q.

Louyeh, M. A., (2016). Silver, magnesium and zinc substituted hydroxyapatite for orthopaedic applications (Doctoral dissertation, University of Birmingham). *Birmingham University Research Repository*. http://etheses.bham.ac.uk/id/eprint/7570.

Luo, X., Zhang, Y., Zandén, C., Murugesan, M., Cao, Y., Ye, L., & Liu, J. (2014). Novel thermal interface materials: Boron nitride nanofiber and indium composites for electronics heat dissipation applications. *Journal of Materials Science: Materials in Electronics*, 25, 2333-2338. https://doi.org/10.1007/s10854-014-1880-8

Ma, P. X. (2004). Scaffolds for tissue fabrication. *Materials Today*, 7 (5), 30–40. https://doi.org/10.1016/S1369-7021(04)00233-0.

Ma, R., Bando, Y., Zhu, H., Sato, T., Xu, C., & Wu, D. (2002). Hydrogen uptake in boron nitride nanotubes at room temperature. *Journal of American Chemical Society*, 124, 7672–7673.

Madihally, S. V, & Matthew, H. W. T. (1999). Porous chitosan scaffolds for tissue engineering. *Biomaterials*, 20 (12), 1133–1142.

Mahajan, A., Kingon, A., Kukovecz, Á., Konya, Z., & Vilarinho, P. M. (2013). Studies on the thermal decomposition of multiwall carbon nanotubes under different atmospheres. *Materials Letters*, 90, 165-168. https://doi.org/10.1016/j.matlet.2012.08.120

Marsich, E., Borgogna, M., Donati, I., Mozetic, P., Strand, B. L., Salvador, S. G.,

Vittur, F., & Paoletti, S. (2007). Alginate/lactose-modified chitosan hydrogels: A bioactive biomaterial for chondrocyte encapsulation. *Journal of Biomedical Materials Research Part A*, 84A (2), 364-376. https://doi.org/10.1002/jbm.a.31307.

Mellado, P., McIlwee, H. A., Badrossamay, M. R., Goss, J. A., Mahadevan, L., & Kit Parker, K. (2011). A simple model for nanofiber formation by rotary jet-spinning. *Applied Physics Letters*, 99 (20), 203107. https://doi.org/10.1063/1.3662015.

Merlo, A., Mokkapati, V. R. S. S., Pandit, S., & Mijakovic, I. (2018). Boron nitride nanomaterials: Biocompatibility and bio-applications. *Biomaterials Science*, 6, 2298-2311. https://doi.org/10.1039/c8bm00516h.

Miszuk, J. M., Xu, T., Yao, Q., Fang, F., Childs, J. D., Hong, Z., Tao, J., Fong, H., & Sun, H. (2018). Functionalization of PCL-3D electrospun nanofibrous scaffolds for improved BMP2-induced bone formation. *Applied Materials Today*, 10, 194–202. https://doi.org/10.1016/j.apmt.2017.12.004

Mondal, S., De Anda Reyes, M. E., & Pal, U. (2017). Plasmon induced enhanced photocatalytic activity of gold loaded hydroxyapatite nanoparticles for methylene blue degradation under visible light. *RSC Advances*, 7, 8633-8645. https://doi.org/10.1039/C6RA28640B.

Monteiro, S. N., Skury, A. L. D., de Azavedo, M. G., & Bobrovnitchii, G. S. (2013). Cubic boron nitride competing with diamond as a superhard engineering material – an overview. *Journal of Materials Research and Technology*, 2 (1), 68-74. https://doi.org/10.1016/j.jmrt.2013.03.004.

More, R. B., Haubold, A. D., & Bokros, J. C. (2013). Pyrolytic carbon for long-term medical implants. In Ratner, B. D., Hoffman, A. S., & Schoen, F. J. (Eds.), *Biomaterials Science*. Elsevier, Amsterdam, pp. 209-222.

Moyer, H. R., Kinney, R. C., Singh, K. A., & Williams, J. K. (2010). Alginate microencapsulation technology for the percutaneous delivery of adipose-

derived stem cells. *Transplantation Surgery and Research*, 65 (5), 497–503. https://doi.org/10.1097/SAP.0b013e3181d37713.

Nagarajan, S., Belaid, H., Pochat-Bohatier, C., Teyssier, C., Iatsunskyi, I., Coy, E., Balme, S., Cornu, D., Miele, P., Kalkura, N. S., Cavaillès, V., & Bechelany, M. (2017). Design of boron nitride/gelatin electrospun nanofibers for bone tissue engineering, *ACS Applied Material Interfaces*, 9, 33695-33706. https://doi.org/10.1021/acsami.7b13199.

Nakamura, H., Koganei, H., Miyoshi, T., Sakurai, Y., & Ono, K. (2015). Antitumor effect of boron nitride nanotubes in combination with thermal neutron irradiation on BNCT. *Bioorganic & Medicinal Chemistry Letters*, 25 (2), 172–174. https://doi.org/10.1016/j.bmcl.2014.12.005.

Navarro, M., Michiardi, A., Castaño, O., & Planell, J. A. (2008). Biomaterials in orthopaedics. *Journal of the Royal Society Interface*, 5 (27), 1137–1158. https://doi.org/10.1098/rsif.2008.0151.

Ngiam, M., Liao, S., Patil, A. J., Cheng, Z., Chan, C. K., & Ramakrishna, S. (2009). The fabrication of nano-hydroxyapatite on PLGA and PLGA/collogen nanofibrous composite scaffolds and their effects in osteoblastic behavior for bone tissue engineering. *Bone*, 45 (1), 4-16. https://doi.org/10.1016/j.bone.2009.03.674.

Nguyen, T. H., & Lee, B. T. (2013). *In vitro* and *in vivo* studies of rhBMP2-coated PS/PCL fibrous scaffolds for bone regeneration. *Journal of Biomedical Materials Research-Part A*, 101A (3), 797–808. https://doi.org/10.1002/jbm.a.34382.

Ofudje, E. A., Adeogun, A. I., Idowu, M. A., & Kareem, S. O. (2019). Synthesis and characterization of Zn-Doped hydroxyapatite: scaffold application, antibacterial and bioactivity studies. *Heliyon*, 5 (5), e01716. https://doi.org/10.1016/j.heliyon.2019.e01716.

Oku, T., & Kuno, M. (2003). Synthesis , argon/hydrogen storage and magnetic

properties of boron nitride nanotubes and nanocapsules. *Diamond and Related Materials*, 12 (3), 840–845.

Olivier, V., Faucheux, N., & Hardouin, P. (2004). Biomaterial challenges and approaches to stem cell use in bone reconstructive surgery. *Drug Discovery Today*, 9 (18), 803-811. https://doi.org/10.1016/S1359-6446(04)03222-2.

Oliveira, S. M., Amaral, I. F., Barbosa, M. A., & Teixeira, C. C. (2009). Engineering endochondral bone: in vitro studies. *Tissue Engineering Part A*, 15 (3), 625-634. https://doi.org/10.1089/ten.tea.2008.0051.

Ong, S.-Y., Wu, J., Moochhala, S. M., Tan, M.-H., & Lu, J. (2008). Biomaterials Development of a chitosan-based wound dressing with improved hemostatic and antimicrobial properties. *Biomaterials*, 29 (32), 4323–4332. https://doi.org/10.1016/j.biomaterials.2008.07.034.

Ortiz, I. Y., Raybolt dos Santos, A., Costa, A. M., Mavropoulos, E., Tanaka, M. N., Prado da Silva, M. H., & de Souza Camargo, S. (2016). In vitro assessment of zinc apatite coatings on titanium surfaces. *Ceramics International*, 42 (14), 15502–15510. https://doi.org/10.1016/j.ceramint.2016.06.203.

Ozbek, B., Erdogan, B., Ekren, N., Faik, N. O., Akyol, S., Ben- Nissan, B., Sasmazel, H. T., Kalkandelen, C., Mergen, A. Kuruca, S. E., Gunduz, O. & Gunduz, O. (2017). Production of the novel fibrous structure of poly(ε-caprolactone) /tri-calcium phosphate/hexagonal boron nitride composites for bone tissue engineering. *Journal of the Australian Ceramic Society*, 54, 251-260. https://doi.org/10.1007/s41779-017-0149-0.

Pakdel, A., Bando, Y., & Golberg, D. (2014). Nano boron nitride flatland. *Chemical Society Review*, 43, 934-959. https://doi.org/10.1039/c3cs60260e.

Paşcu, E. I., Stokes, J., McGuinness, G. B. (2013). Electrospun composite of PHBV, silk fibroin and nano-hydroxyapatite for bone tissue engineering, *Materials Science and Engineering: C*, 33 (8), 4905-4916.

https://doi.org/10.1016/j.msec.2013.08.012

Patel, N., Oudemans, P.V., Hillman, B.I. & Kobayashi, D. Y. (2013). Use of the tetrazolium salt MTT to measure cell viability effects of the bacterial antagonist *Lysobacter enzymogenes* on the filamentous fungus *Cryphonectria parasitica* . *Antonie van Leeuwenhoek* 103, 1271–1280. https://doi.org/10.1007/s10482-013-9907-3

Pazarçeviren, A. E., Tezcaner, A., Keskin, D., Kolukısa, S. T., Sürdem, S., & Evis, Z. (2020). Boron-doped Biphasic Hydroxyapatite/β-Tricalcium Phosphate for Bone Tissue Engineering. *Biological Trace Element Research*, 1-13. https://doi.org/10.1007/s12011-020-02230-8.

Pfister, L. A., Papaloïzos, M., Merkle, H. P., & Gander, B. (2006). Hydrogel nerve conduits produced from alginate / chitosan complexes. *Journal of Biomedical Materials Research Part A*, 80 (4), 932-937. https://doi.org/10.1002/jbm.a

Popa, C. L., Deniaud, A., Michaud-Soret, I., Guégan, R., Motelica-Heino, M., & Predoi, D. (2016). Structural and biological assessment of zinc doped hydroxyapatite nanoparticles. *Journal of Nanomaterials*, 2016, 1062878. https://doi.org/10.1155/2016/1062878.

Prabakaran, K., Balamurugan, A., & Rajeswari, S. (2005). Development of calcium phosphate based apatite from hen's eggshell. *Bulletin of Materials Science*, 28, 115-119. https://doi.org/10.1007/BF02704229.

Predoi, D., Iconaru, S. L., Predoi, M. V., Buton, N., & Motelica-Heino, M. (2019). Zinc doped hydroxyapatite thin films prepared by sol–gel spin coating procedure. *Coatings*, 9 (3), 156. https://doi.org/10.3390/coatings9030156.

Qiu, Y., Yu, J., Rafique, J., Yin, J., Bai, X., & Wang, E. (2009a). Large-scale production of aligned long boron nitride nanofibers by multijet/multicollector electrospinning. *Journal of Physical Chemistry C*, 113 (26), 11228–11234.

https://doi.org/10.1021/jp901267k.

Qiu, Y., Yu, J., Yin, J., Tan, C., Zhou, X., Bai, X., & Wang, E. (2009b). Synthesis of continuous boron nitride nanofibers by solution coating electrospun template fibers. *Nanotechnology*, 20 (34), 345603. https://doi.org/10.1088/0957-4484/20/34/345603.

Qu, J., Li, Q., Luo, C., Cheng, J., & Hou, X. (2018). Characterization of flake boron nitride prepared from low temperature combustion synthesized precursor and its application for dye adsorption. *Coatings* 8 (6), 214. https://doi.org/10.3390/coatings8060214.

Rahaman, M. N., Xiao, W., & Huang, W. (2018). Bioactive glass composites for bone and musculoskeletal tissue engineering. *Bioactive Glasses*, 285-336. https://doi.org/10.1016/b978-0-08-100936-9.00013-7.

Rahmati, M., Fathi, M., & Ahmadian, M. (2018). Preparation and structural characterization of bioactive bredigite ($Ca_7MgSi_4O_{16}$) nanopowder. *Journal of Alloys and Compounds*, 732, 915. https://doi.org/10.1016/j.jallcom.2017.10.132.

Rey, C., Combes, C., Drouet, C., & Glimcher, M. J. (2009). Bone mineral: update on chemical composition and structure. *Osteoporosis International*, 20 (6), 1013–1021. https://doi.org/10.1007/s00198-009-0860-y.

Rho, K. S., Jeong, L., Lee, G., Seo, B.-M., Park, Y. J., Hong, S.-D., Roh, S., Cho, J. J., Park, W. H., & Min, B. (2006). Electrospinning of collagen nanofibers : Effects on the behavior of normal human keratinocytes and early-stage wound healing. *Biomaterials,* 27 (8), 1452–1461. https://doi.org/10.1016/j.biomaterials.2005.08.004

Rocca, A., Marino, A., Del Turco, S., Cappello, V., Parlanti, P., Pellegrino, M., Golberg, D., Mattoli, V., & Ciofani, G. (2016). Pectin-coated boron nitride nanotubes: In vitro cyto-/immune-compatibility on RAW 264.7 macrophages. *Biochimica et Biophysica Acta* (*BBA) - General Subjects*, 1860

(4), 775-784. https://doi.org/10.1016/j.bbagen.2016.01.020.

Rogalski, J. J., Bastiaansen, C. W. M., & Peijs, T. (2018). PA6 nanofibre production: A comparison between rotary jet spinning and electrospinning. *Fibers*, 6 (2), 37. https://doi.org/10.3390/fib6020037.

Rödel, M., Meininger, S., Groll, J., & Gbureck, U. (2018). Bioceramics as drug delivery systems. *Fundamental Biomaterials: Ceramics*, 153-194. https://doi.org/10.1016/B978-0-08-102203-0.00007-X.

Rubio, A., Corkill, J. L., & Cohen, M. L. (1993). Theory of graphitic boron nitride nanotubes. *Physical Review B*, 49 (7), 5081.

Rupasinghe, D. B., Knapp, O., Blomster, L. V, Schmid, A. B., Adams, D. J., King, G. F., & Ruitenberg, M. J. (2012). Localization of Nav 1.7 in the normal and injured rodent olfactory system indicates a critical role in olfaction, pheromone sensing and immune function. *Channels (Austin, Tex.)*, 6 (2), 103–110. https://doi.org/10.4161/chan.19484.

Salvetti, A., Li, X., Pellegrino, T., & Ciofani, G. (2015). In vivo biocompatibility of boron nitride nanotubes : effects on stem cell biology and tissue regeneration in planarians. *Nanomedicine*, 10 (12), 1911-1922. https://doi.org/10.2217/nnm.15.46

Santos, M. H., Shaimberg, A. P. M., Valerio, P., Goes, A. M., Leite, M. de F., & Mansur, H. S. (2007). Cytocompatibility evaluation of hydroxyapatite/collagen composites doped with Zn^{2+}, *Revista Matéria*, 12 (2), 307-312. http://www.materia.coppe.ufrj.br/sarra/artigos/artigo10852

Sell, S. A., Mcclure, M. J., Garg, K., Wolfe, P. S., & Bowlin, G. L. (2009). Electrospinning of collagen / biopolymers for regenerative medicine and cardiovascular tissue engineering. *Advanced Drug Delivery Reviews*, 61 (12), 1007–1019. https://doi.org/10.1016/j.addr.2009.07.012

Sergi, R., Bellucci, D., Candidato, R. T., Lusvarghi, L., Bolelli, G., Pawlowski, L., Candiani, G., Altomare, L., De Nardo, L., & Cannillo, V. (2018). Bioactive

Zn-doped hydroxyapatite coatings and their antibacterial efficacy against *Escherichia coli* and *Staphylococcus aureus*. *Surface and Coatings Technology*, 352, 84–91. https://doi.org/10.1016/j.surfcoat.2018.08.017

Shen, W., Chen, X., Chen, J., Yin, Z., Chin, B., Chen, W., & Ouyang, H. (2010). The effect of incorporation of exogenous stromal cell-derived factor-1 alpha within a knitted silk-collagen sponge scaffold on tendon regeneration. *Biomaterials*, 31 (28), 7239–7249. https://doi.org/10.1016/j.biomaterials.2010.05.040

Shi, X., Wang, Y., Ren, L., Gong, Y., & Wang, D. (2009). Enhancing alendronate release from a novel PLGA/hydroxyapatite microspheric system for bone repairing applications. *Pharmaceutical Research*, 26 (2), 422–430. https://doi.org/10.1007/s11095-008-9759-0.

Shore, S. G. (1968). The chemistry of boron and its compounds. *Journal of Molecular Structure*, 45 (3), 211. https://doi.org/10.1016/0022-2860(68)80030-4.

Singh H., Singh S., & Prakash C. (2019). Current Trends in Biomaterials and Bio-manufacturing. In: Prakash C. et al. (eds) Biomanufacturing. Springer, Cham. https://doi.org/10.1007/978-3-030-13951-3_1

Smith, P. J., Blunt, N., Wiltshire, M., Hoy, T., Teesdale-Spittle, P., Craven, M. R., Watson, J. V., Amos, W. B., Errington, R. J., & Patterson, L. H. (2000). Characteristic of a novel deep red/infrared fluorescent cell-permeant DNA probe, DRAQ5, in intact human cells analyzed by flow cytometry, confocal and multiphoton microscopy. *Cytometry*, 40 (4), 280–291. https://doi.org/10.1002/1097-0320(20000801)40:4<280::aid-cyto4>3.0.co;2-7.

Sogo, Y., Ito, A., Fukasawa, K., Sakurai, T., & Ichinose, N. (2004). Zinc containing hydroxyapatite ceramics to promote osteoblastic cell activity. *Materials Science and Technology*, 20 (9), 1079-1083. https://doi.org/10.1179/026708304225019704

Song, H. H., Yoo, M. K., Moon, H. S., Choi, Y. J., Lee, H. C., & Cho, C. S. (2007). A novel polycaprolactone/hydroxyapatite scaffold for bone tissue engineering. *Key Engineering Materials*, 342–343, 265–268. https://doi.org/10.4028/0-87849-436-7.265

Sonmez, E., Cacciatore, I., Bakan, F., Turkez, H., Mohtar, Y. I., Togar, B., & Stefano, A. D. (2016). Toxicity assessment of hydroxyapatite nanoparticles in rat liver cell model in vitro. *Human and Experimental Toxicology*, 35 (10), 1073-1083. https://doi.org/10.1177/0960327115619770.

Sossa, P. A. F., Giraldo, B. S., Garcia, B. C. G., Parra, E. R., & Arango, P. J. A. (2018). Comparative study between natural and synthetic hydroxyapatite: structural, morphological and bioactivity properties. *Matéria (Rio J.),*23 (4),1-17. https://doi.org/10.1590/s1517-707620180004.0551.

Stanić, V., Dimitrijević, S., Antić-Stanković, J., Mitrić, M., Jokić, B., Plećaš, I. B., & Raičević, S. (2010). Synthesis, characterization and antimicrobial activity of copper and zinc-doped hydroxyapatite nanopowders. *Applied Surface Science*, 256 (20), 6083–6089. https://doi.org/10.1016/j.apsusc.2010.03.124

Subbiah, T., Bhat, G. S., Tock, R. W., Parameswaran, S., & Ramkumar, S. S. (2005). Electrospinning of nanofibers. *Journal of Applied Polymer Science*, 96 (2), 557–569. https://doi.org/10.1002/app.21481.

Suh, J.-K F., & Matthew, H. W. T. (2000). Application of chitosan-based polysaccharide biomaterials in cartilage tissue engineering: a review. *Biomaterials*, 21 (24), 2589-2598. https://doi.org/10.1016/S0142-9612(00)00126-5

Swarnalatha, B., Nair, S. L., Shalumon, K. T., Milbauer, L. C., Jayakumar, R., Paul-Prasanth, B., Menon, K. K., Hebbel, R. P., Somani, A., & Nair, S. V. (2013). Poly(lactic acid)–chitosan–collagen composite nanofibers as substrates for blood outgrowth endothelial cells. *International Journal of Biological Macromolecules*, 58, 220–224. https://doi.org/10.1016/j.ijbiomac.2013.03.060.

Tang, X., Thankappan, S. K., Lee, P., Fard, S. E., Harmon, M. D., Tran, K., & Yu, X. (2014). Polymeric biomaterials in tissue engineering and regenerative medicine. In S. K. G. Bar, L. C. Md, & M. Deng (Ed.), *Natural and Synthetic Biomedical Polymers* (1st ed., pp. 351-371). Elsevier Science. https://doi.org/10.1016/B978-0-12-396983-5.00022-3

Tank, K P, Sharma, P., Kanchan, D. K., & Joshi, M. J. (2011). FTIR, powder XRD, TEM and dielectric studies of pure and zinc doped nano-hydroxyapatite. *Crystal Research and Technology*, 46 (12), 1309–1316. https://doi.org/10.1002/crat.201100080

Tank, K. P., Chudasama, K. S., Thaker, V. S., & Joshi, M. J. (2014). Pure and zinc doped nano-hydroxyapatite: Synthesis, characterization, antimicrobial and hemolytic studies. *Journal of Crystal Growth*, 401, 474–479. https://doi.org/10.1016/j.jcrysgro.2014.01.062.

Terrones, M., Hsu, W. K., Terrenes, H., Zhang, J. P., Ramos, S., Hare, J. P., Castillo, K., Prassides, K., Cheetham, A. K., Kroto, H. W., & Walton, D. R. M. (1996). Metal particle catalysed production of nanoscale BN structures. *Chemical Physics Letters*, 259 (5–6), 568–573. https://doi.org/10.1016/0009-2614(96)00773-7

Thadavirul, N., Pavasant, P., & Supaphol, P. (2014). Development of polycaprolactone porous scaffolds by combining solvent casting, particulate leaching, and polymer leaching techniques for bone tissue engineering. *Journal of Biomedical Materials Research-Part A*, 102 (10), 3379–3392. https://doi.org/10.1002/jbm.a.35010.

Thian, E. S., Konishi, T., Kawanobe, Y., Lim, P. N., Choong, C., Ho, B., & Aizawa, M. (2013). Zinc-substituted hydroxyapatite: A biomaterial with enhanced bioactivity and antibacterial properties. *Journal of Materials Science: Materials in Medicine*, 24 (2), 437–445. https://doi.org/10.1007/s10856-012-4817-x.

Tomoaia, G., Soritau, O., Tomoaia-Cotisel, M., Pop, L.-B., Pop, A., Mocanu, A.,

Horovitz, O., & Bobos, L.-D. (2013). Scaffolds made of nanostructured phosphates, collagen and chitosan for cell culture. *Powder Technology*, 238, 99–107. https://doi.org/10.1016/j.powtec.2012.05.023

Türk, S., Altınsoy, I., Efe, G. Ç., Ipek, M., Özacar, M., & Bindal, C. (2019). Biomimetic synthesis of Ag, Zn or Co doped HA and coating of Ag, Zn or Co doped HA/fMWCNT composite on functionalized Ti. *Materials Science and Engineering C*, 99, 986–998. https://doi.org/10.1016/j.msec.2019.02.025.

Uysal, I., Severcan, F., & Evis, Z. (2013). Characterization by Fourier transform infrared spectroscopy of hydoxyapatite co-doped with zinc and fluoride. *Ceramics International*, 39 (7), 7727-7733. https://doi.org/10.1016/j.ceramint.2013.03.029.

Uysal, I., Severcan, F., Tezcaner, A., & Evis, Z. (2014). Co-doping of hydroxyapatite with zinc and fluoride improves mechanical and biological properties of hydroxyapatite. *Progress in Natural Science: Materials International*, 24 (4), 340–349. https://doi.org/10.1016/j.pnsc.2014.06.004.

Vasconcellos, L. M. R., Elias, C. de M. V., Minhoto, G. B., Abdala, J. M. A., Andrade, T. M., de Araujo, J. C. R., Gusmão, S. B. S., Viana, B. C., Marciano, F. R., & Lobo, A. O., (2020). Rotary-jet spun polycaprolactone/nano-hydroxyapatite scaffolds modified by simulated body fluid influenced the flexural mode of the neoformed bone. *Journal of Materials Science: Materials in Medicine*, 31, 72. https://doi.org/10.1007/s10856-020-06403-8.

Venkatesan, J., Nithya, R., Sudha, P. N., Kim, S.-K. (2014). Role of alginate in bone tissue engineering. *Advances in Food and Nutrition Research*, 73, 45-57. https://doi.org/10.1016/B978-0-12-800268-1.00004-4.

Wang, J., Ma, F., & Sun, M. (2017). Graphene, hexagonal boron nitride, and their heterostructures: properties and applications. *RSC Advances*, 7, 16801-16822 https://doi.org/10.1039/c7ra00260b.

Wang, X., Ito, A., Sogo, Y., Li, X., & Oyane, A. (2010). Zinc-containing apatite layers on external fixation rods promoting cell activity. *Acta Biomaterialia*, 6 (3), 962–968. https://doi.org/10.1016/j.actbio.2009.08.038.

Webster, T. J., Ergun, C., Doremus, R. H., & Bizios, R. (2001). Hydroxylapatite with substituted magnesium, zinc, cadmium, and yttrium. II. Mechanisms of osteoblast adhesion. *Journal of Biomedical Materials Research*, 59 (2), 312-317. https://doi.org/10.1002/jbm.1247

Weng, Q., Wang, X., Wang, X., Bando, Y., & Golberg, D. (2016). Functionalized hexagonal boron nitride nanomaterials: emerging properties and applications. *Chemical Society Review*, 45, 3989. https://doi.org/10.1039/c5cs00869g.

Wittaya-areekul, S., & Prahsarn, C. (2006). Development and in vitro evaluation of chitosan-polysaccharides composite wound dressing, *International Journal of Pharmaceutics*, 313 (1-2), 123-128. https://doi.org/10.1016/j.ijpharm.2006.01.027.

Wu, Y., Li, C., Fan, F., Liang, J., Yang, Z., Wei, X., & Chen, S. (2019). PVAm nanofibers fabricated by rotary jet wet spinning and applied to bisphenol a recognition. *ACS Omega*, 4, 21361-21369. https://doi.org/10.1021/acsomega.9b02964.

Wutticharoenmongkol, P., Sanchavanakit, N., Pavasant, P., & Supaphol, P. (2006). Preperation and characterization of novel bone scaffolds based on electrospun polycaprolacone fibers filled with nanoparticles. *Macromolecular Bioscience*, 6, 70-77. https://doi.org/10.1002/mabi.200500150.

Xu, Z., Golberg, D., & Bando, Y. (2009). In Situ TEM-STM recorded kinetics of boron nitride nanotube failure under current flow*, Nano Letter,* 9 (6), 2251-2254. https://doi.org/10.1021/nl900379c.

Yamada, Y., Ito, A., Kojima, H., Sakane, M., Miyakawa, S., Uemura, T., & LeGeros, R. Z. (2007). Inhibitory effect of Zn^{2+} in zinc-containing β-

tricalcium phosphate on resorbing activity of mature osteoclasts. *Journal of Biomedical Materials Research*, 84A (2), 344-352. https://doi.org/10.1002/jbm.a.31265.

Yamauchi, K., Goda, T., Takeuchi, N., Einaga, H., & Tanabe, T. (2004). Preparation of collagen/calcium phosphate multilayer sheet using enzymatic mineralization. *Biomaterials*, 25 (24), 5481–5489. https://doi.org/10.1016/j.biomaterials.2003.12.057.

Yedekci, Y., Gedik, E., Evis, Z., Dogan, L., Özyiğit, G., & Gürkaynak, M. (2021). Radiosensitization induced by zinc-dooped hydroxyapatite nanoparticles in breast cancer cells. *Applied Ceramics Technology*, 1-10. https://doi.org/10.1111/ijac.13707.

Ying, X., Cheng, S., Wang, W., Lin, Z., Chen, Q., Zhang, W., Kou, D., Shen, Y., Cheng, X., Rompis, F. A., Peng, L., & Lu, C. Z. (2011). Effect of boron on osteogenic differentiation of human bone marrow stromal cells. *Biological Trace Element Research*, 144, 306-315. https://doi.org/10.1007/s12011-011-9094-x.

Yoshimoto, H., Shin, Y. M., Terai, H., & Vacanti, J. P. (2003). A biodegradable nanofiber scaffold by electrospinning and its potential for bone tissue engineering. *Biomaterials*, 24 (12), 2077–2082. https://doi.org/10.1016/S0142-9612(02)00635-X.

Yu, D. P., Sun, X. S., Lee, C. S., Bello, I., Lee, S. T., Gu, H. D., Leung, K. M., Zhou, G. W., Dong, Z. F., & Zhang, Z. (1998). Synthesis of boron nitride nanotubes by means of excimer laser ablation at high temperature. *Applied Physics Letters*, 72 (16), 1966–1968. https://doi.org/10.1063/1.121236

Yu, J., & Matsumoto, S. (2003). Controlled growth of large cubic boron nitride crystals by chemical vapor deposition. *Diamond and Related Materials*, 12 (9), 1539-1543. https://doi.org/10.1016/S0925-9635(03)00222-X

Zare, Y. (2016). Study of nanoparticles aggregation/agglomeration in polymer

particulate nanocomposites by mechanical properties. *Composites Part A: Applied Science and Manufacturing*, 84, 158-164. https://doi.org/10.1016/j.compositesa.2016.01.020

Zeng, X., Sun, J., Yao, Y., Sun, R., Xu, J., & Wong, C. (2017). A Combination of boron nitride nanotubes and cellulose nanofibers for the preparation of a nanocomposite with high thermal conductivity. *ACS Nano*, 11 (5), 5167-5178. https://doi.org/10.1021/acsnano.7b02359.

Zhao, F., Yin, Y., Lu, W. W., Leong, J. C., Zhang, W., Zhang, J., Zhang, M., & Yao, K. (2002). Preparation and histological evaluation of biomimetic three-dimensional hydroxyapatite / chitosan-gelatin network composite scaffolds. *Biomaterials*, 23 (15), 3227–3234. https://doi.org/10.1016/S0142-9612(02)00077-7.

Zhi, C., Bando, Y., & Tang, C. (2006). Boron nitride nanotubes/polystyrene composites. *Journal of Materials Research*, 21 (11), 2794-2800. https://doi.org/10.1557/JMR.2006.0340.

Zhou Y. L., Huan Z. G., Chang J. (2016). Silicate-Based Bioactive Composites for Tissue Regeneration. In: Antoniac I. (eds) Handbook of Bioceramics and Biocomposites. Springer, Cham. https://doi.org/10.1007/978-3-319-12460-5_15.